SPINTRONIC DEVICES AS P-BITS FOR PROBABILISTIC COMPUTING

A Dissertation

Submitted to the Faculty

of

Purdue University

by

Punyashloka Debashis

In Partial Fulfillment of the

Requirements for the Degree

of

Doctor of Philosophy

May 2020

Purdue University

West Lafayette, Indiana

THE PURDUE UNIVERSITY GRADUATE SCHOOL
STATEMENT OF DISSERTATION APPROVAL

Dr. Zhihong Chen, Chair

School of Electrical and Computer Engineering

Dr. Joerg Appenzeller

School of Electrical and Computer Engineering

Dr. Supriyo Datta

School of Electrical and Computer Engineering

Dr. Yong Chen

Department of Physics and Astronomy

Approved by:

Dr. Dimitri Peroulis

Head of the School of Electrical and Computer Engineering

To Bounana, Chuabapa, Papu and Anupama.

ACKNOWLEDGMENTS

Firstly, I would like to extend my sincere gratitude towards my advisor, Prof. Zhihong Chen. In addition to advising me technically throughout my PhD, she has played a very crucial role in developing an independent research outlook in me by allowing me the freedom to work on topics that interested me, while caring deeply for the overall direction of my PhD and future career path.

I this regard, I should also thank Prof. Joerg Appenzeller who has been like a co-advisor for me. I thank him for the numerous discussions and rigorous analysis during the group meetings and for teaching me the value of setting the highest ethical standards in research. It was a privilege to have worked with Prof. Supriyo Datta during my time at Purdue. I thank him for the several insightful discussions and his advice during my PhD. My thesis work has greatly benefited from the ideas generated in his group. He will always remain a source of inspiration for me. I would like to thank Prof. Pramey Upadhyaya for sharing his valuable ideas with me and for the opportunity to work in collaboration with his group in the last couple of years. I also thank Prof. Yong Chen in this regard and for serving in my thesis committee. Dr. Neil Dilley has been a constant source of knowledge and I thank him for bearing with me through out all the times I have bugged him regarding magnetic and electronic measurements and magnetism in general.

I am very grateful to Dr. Ashish Verma Penumatcha, Dr. Chia-Ching Lin and Prof. Suprem Das for their guidance and support during the initial years of my PhD, which has continued even after they completed their journey at Purdue. I also thank Dr. Sunny Chugh and Dr. Ruchit Mehta for being very supportive even before I joined Purdue for my PhD. I was lucky to have colleagues in the spin group like Dr. Terry Hung, Tingting Shen and Vaibhav Ostwal, who have always helped me by sharing their knowledge and experience and the experimental tricks that they developed.

Towards the end of my PhD, Xiangkai and John have helped me in performing several experiments. I wish the best for their PhD journey at Purdue and future endeavors. I owe special thanks to Dr. Kerem Camsari and Dr. Rafatul Faria for sharing their insights and ideas with me and for always providing a theoretical benchmark for my experimental results. I have always enjoyed discussions with them and other members of the Datta group- Orchi Hassan, Jan Kaiser, Laxmi Anirrudh Ghantasala, Dr. Brian Sutton and Dr. Vinh Diep. I have enjoyed my interactions with other members of our research groups- Dr. Abhijith Prakash, Dr. Feng Zhang, Chin-Sheng Pang, Ruiping Zhou, Suki Zhang, Peng Wu, Chun-Li Lo, Shengjiao Zhang.

This PhD would have been incomplete without the tireless support of the amazing technical staff at Birck Nanotechnology center. Special thanks go to Bill Rowe, Dave Lubelski and Sean Rinehart for helping me during the times I have struggled in the cleanroom. I would also like to thank Mary Jo, Nancy Black, Viki Rogers for their prompt help regarding many official matters.

My PhD life at Purdue has been very enjoyable due to the presence of my many good friends - Harsha, Vasu, Prabhu, Shovan, Nitish, Piyush, Gautham, Vikrant, Surya, Krishna, Rishabh, Sansit and others. I will cherish the special moments we have spent together in the last several years.

This PhD was the dream of my parents Suravi and Narayana. I cannot thank them enough for the life they have provided me through the sacrifices they have made in their own lives. My brother Dharmashloka has always been there for me and I wish to do the same. Finally, I would like to thank Anupama, for her endless perseverance and belief in me. Marrying you is the best experiment I did during my PhD.

TABLE OF CONTENTS

Page

Page

LIST OF FIGURES

Figure Page

Figure Page

Figure Page

Figure Page

Figure Page

Figure Page

Figure Page

Figure Page

ABSTRACT

Debashis, Punyashloka PhD, Purdue University, May 2020. Spintronic Devices as P-bits for Probabilistic Computing. Major Professor: Zhihong Chen.

Several beyond-CMOS computing technologies have emerged in the recent years to tackle the modern computing tasks that become intractable for Boolean logic based computation, performed on a von Neumann computer. The underlying philosophy in developing such technologies is to harness the natural physics of the computing elements to perform certain specialized computing tasks. One such beyond-CMOS computing paradigm- probabilistic computing is based on a "p-bit" that randomly fluctuates between 0 and 1, a behavior that is naturally mimicked by thermally unstable nanomagnets. A coupled network of such nanomagnets traverses through its collective states and is naturally guided towards the pre-designed low energy states. This property has been shown to be useful in providing hardware acceleration to a wide variety of problems in optimization, invertible logic, inference and machine learning. In order to develop practical circuits with p-bits, an efficient way to implement them in hardware by leveraging spintronics technology is required and forms the subject of this thesis. First, the experiments demonstrating the convergence of a weakly coupled nanomagnet network's configuration towards the ground state of the associated Hamiltonian is shown. Next, it is demonstrated that by varying the interconnection strength and bias parameters in a two p-bit electrical circuit, Bayesian network building blocks can be implemented in hardware. Following this, a unique p-bit design based on the interaction of spin orbit torque on weak perpendicular anisotropy nanomagnets is presented and its interesting properties such as stochastic resonance, electrically tunable fluctuation rate and correlated fluctuations of two such devices are discussed. As related work, a prototype spin logic device is demon-

strated using a composite stack of stable nanomagnets having perpendicular and in plane anisotropies. Finally, the development of a hybrid material stack with greatly improved giant spin Hall efficiency by incorporating WSe_2 for energy efficient spin orbit torque switching of nanomagnets is presented.

1. INTRODUCTION

The predominant way to perform computation and information processing in the last few decades has been through digital CMOS hardware, designed according to the von Neumann architecture [1]. This way of computation through a "general purpose processor" has been propelled by the exponential growth of the number of CMOS transistors per unit cost, as predicted by Gordon Moore in 1965 [2]. This computing scheme has proven to be very powerful for a wide range of tasks that are based on deterministic rules such as Boolean logic.

In recent years, driven by the availability of vast amounts of data, tasks such as learning [3, 4], inference [5, 6], optimization [7], etc. have become important for real world applications. For these kinds of tasks, the general purpose processor becomes inefficient due to the von-Neumann bottleneck [8] and the fundamental uncertainty and noise in unstructured real world data. This has led to an increasing demand for alternative computing schemes. In this regard, bio-inspired computing architectures have been studied and implemented using vastly modified CMOS circuits. For example, IBM's TrueNorth chip [9] implements a spiking neural network using a CMOS hardware platform with a non-Von Neumann architectural design. Other prominent examples are Google's tensor processing unit (TPU) [10] that accelerates matrix multiplication for machine learning tasks, Intel's Loihi chip [11] representing a self learning neuromorphic system, Hitachi's spin Ising chip [12] that solves optimization problems by mimicking a network of spins. These implementations have shown large improvements in power consumption and execution time compared to general purpose processors in solving their specialized tasks.

This has further motivated research to look for new hardware technologies that are naturally suited towards these specific applications by virtue of their novel phys-

ical properties. The vision is to develop novel computing hardware components to complement the functionality of CMOS devices in these specialized applications.

1.1 Using physics to do computation

In contrast to the idea of a general purpose processor that solves problems by executing a set of commands listed in an algorithm, a specialized computing core that uses the physical properties of its elements in order to naturally perform computation has gained significant attention in the recent years. Fig. 1.1 illustrates this idea in the context of optimization problems. The idea that in order to simulate physical world systems, the building blocks of computers should naturally embibe the laws governing the physical world was discussed by Feynman in 1982 in his seminal paper titled "Simulating physics with computers" [13]. This paper is often credited as one of the initial ideas that helped launch the field of quantum computing [14]- a field of vast current interest but is not the subject of this thesis work. However, in the same discussion, Feynman envisions "imitating" probabilities in the real world with a computer, "which itself is probabilistic". In such a computer, the probabilities of interest could be obtained by observing the corresponding node, without having to compute them from deterministic rules of statistics which could be intractable to implement on a general purpose computer.

Many computing paradigms related to the above philosophy have emerged over the last decade. For example, superconducting [15] and optical systems [16,17] have been used to implement Ising computing, where many computationally difficult problems are mapped to find the ground state of a network of interacting spins. The complex phase dynamics of oscillators have been utilized to implement associative memory properties [18–20].

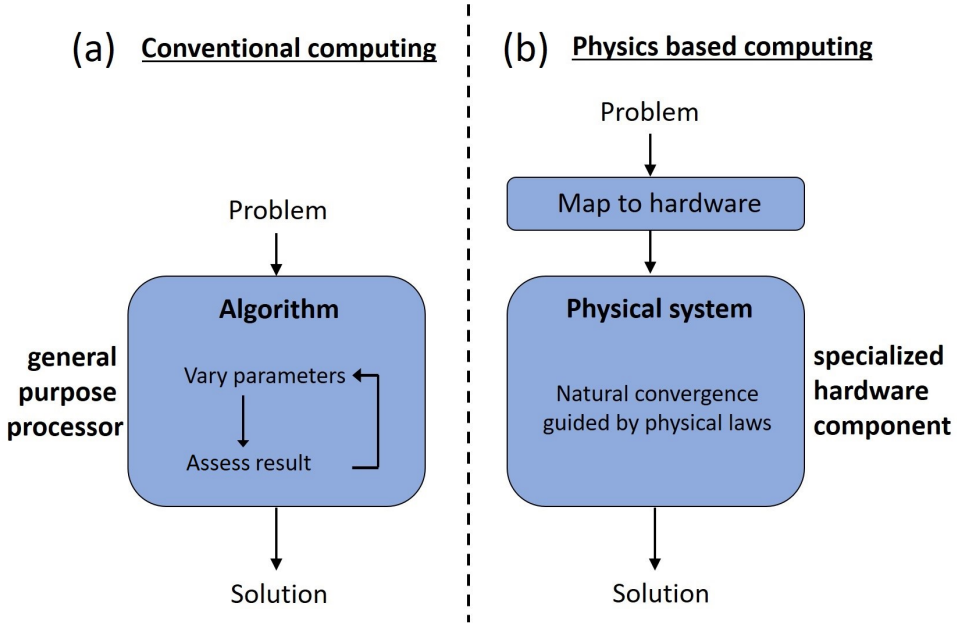

Fig. 1.1. (a) A conventional computer implements an iterative algorithm to compute the solution of the given optimization problem. (b) Certain optimization problems can be mapped directly to a physical system, where the solution is encoded in the the system ground state. The system then naturally converges to the ground state and the solution is obtained by observing its configuration.

1.2 Spintronics technology for specialized hardware

The field of spintronics promises to provide such specialized hardware, owing to an array of novel physical phenomena, compatibility with the standard CMOS process, and its proven success in the technology industry in the field of memory and data storage applications. Spintronics based devices have been well adopted by industry for memory applications after the invention of the magnetic tunnel junction (MTJ) in the 1990's [21, 22]. Magnetoresistive random access memories (MRAMs) have grown to become one of the leading candidates for the next generation of memory technologies, owing to the theoretical prediction [23, 24] and experimental demonstration [25] of spin transfer torque (STT) as a scalable writing mechanism [26]. Discovery of material stacks exhibiting perpendicular magnetic anisotropy (PMA) [27] greatly en-

hanced the scalability of these devices. More recently, spin orbit torque (SOT) has been demonstrated as another writing mechanism, with the benefit of being more energy efficient and scalable compared to STT. More importantly, SOT mechanism [28] allows the separation of read and write paths, resulting in a three terminal structure that is beneficial in terms of endurance in MRAM application, and motivates a path towards realizing a logic device.

This work benefits greatly from the above mentioned inventions such as PMA materials and the mechanism of SOT. The main contribution of this work is in the application of these established and emerging physical phenomena in the field of spintronics to realize hardware units called "p-bits", short for probabilistic bits, which are suitable for a new computing paradigm called probabilistic computing.

1.3 Probabilistic spin logic with p-bits

Conventional computing is based on binary representation of information in terms of "0" and "1", called "bits". These bits of information are processed and stored by stable deterministic devices like the metal oxide semiconductor field effect transistors (MOSFETs) or MTJs with stable magnets having energetic barriers of the order of 40-60 times the thermal energy at room temperature. Probabilistic spin logic (PSL) is a new paradigm of computing [29, 30] that relies on probabilistic bits (p-bits for short) that fluctuate randomly between 0 and 1, with probabilities that can be tuned by an input. Fig. 1.2 shows the concept of the p-bit using a thermally unstable nanomagnet.

The ideal p-bit behavior is described by the following two equations:

$$m_i = sgn\left\{tanh(I_i) - r\right\} \tag{1.1}$$

$$I_i = \sum_j J_{ij} m_j + h_i \tag{1.2}$$

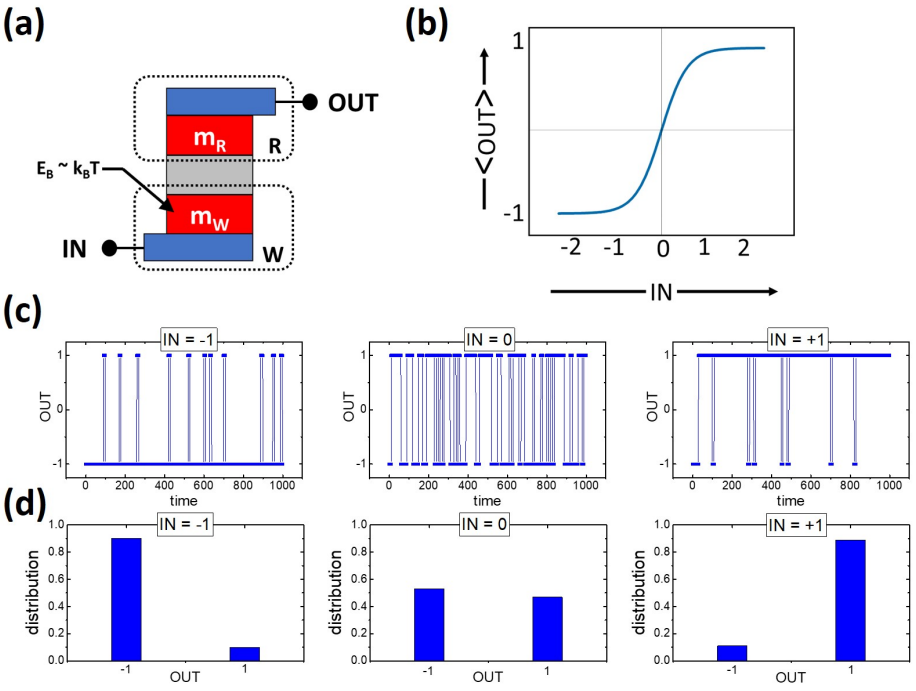

Fig. 1.2. (a) A generic representation for a p-bit is shown with READ and WRITE units represented by m_R and m_W. (b) The time averaged value of magnetization as a function of the input (current or voltage) shows a sigmoidal curve.(d) Telegraphic behavior for various inputs with histograms below them showing fraction of times the magnetization was in the "+1" state and "-1" state.

where the first equation represents the state of the i^{th} p-bit (given by m_i) as a function of its input (I_i). 'r' is a random number with a uniform distribution between -1 and 1, that captures the stochastic aspect of the output. The second equation provides the expression for the input I_i in terms of the connection strengths (J_{ij}) of other p-bits in the network to the i^{th} p-bit and the local bias h_i. This is analogous to the concept of a Binary stochastic neuron (BSN) used in the field of stochastic neural networks [31].

1.3.1 Application domains of probabilistic spin logic

p-bits have recently been shown as natural hardware accelerators for unconventional computing tasks that can be broadly divided into two categories: (i) Neuromorphic inspired and (ii) Quantum inspired.

The neuromorphic inspired domains of application include the compact hardware implementation of Boltzmann machines (BMs) and their variation- restricted BMs as "inference networks". Through numerical simulations, p-bits have been shown to provide hardware acceleration to restricted BMs in digit recognition task [32]. Recently, Kaiser et al. [33] showed hardware acceleration of specific machine learning algorithms using p-bits. Another application is the hardware acceleration of directed graphs called Bayesian networks [34]. In ref [35] Faria et al. have shown through numerical simulations that the conditional probability tables that form the building blocks of Bayesian networks can be efficiently mapped to the connection weights and biases between p-bits. Such circuits can then provide hardware acceleration to the stochastic algorithms like Gibbs sampling [36], utilized to perform Bayesian inference [37]. Chapter 4 in this thesis presents an experimental implementation of the Bayesian network building block using hardware p-bits.

One example of quantum inspired application is the implementation of an Ising network for solving optimization problems like the travelling salesman problem as described by Sutton et al. [38]. Chapter 2 presents an experimental demonstration of a small Ising network using dipolar coupled nanomagnets. It is shown that magnetization of the system goes to the minimum energy configuration, which encodes the solution to the problem mapped to the Ising network. Another example of quantum inspired application is the implementation of "invertible logic" using p-bits [30]. These circuits are analogous to digital CMOS logic gates. However, the interesting advantage in these circuits is that they can be operated in the backward direction: the outputs can be clamped externally and the circuit provides all the possible inputs that are consistent with the clamped output. A 4-bit multiplier, having the feature

of invertibility to function as a factorizer was demonstrated using p-bits by Camsari et al. [30]. In both the types of networks described above, the solution is obtained by guiding the network of p-bits to go to their ground state configuration through the process of "classical annealing". In ref [39], using the example of a transverse Ising Hamiltonian [40], it is argued that the hardware acceleration of "simulated quantum annealing" [41] can be achieved for sign free Hamiltonians [42,43] by using replicated arrays of p-bits.

1.3.2 Hardware implementation of p-bits

Natural stochasticity in low barrier nanomagnets

Low barrier nanomagnets (LBNM) are one of the natural candidates for implementing p-bits, and is the technology studied in this thesis for implementation of p-bits.

The magnetization of a uniaxial anisotropy nanomagnet has two stable directions along its anisotropy axis: "UP" and "DN" for nomenclature. The two states are separated by an energy barrier, E_B, which stabilizes the magnetization in one of the states. The magnetization stays in that state with an average retention time given by:

$$\tau = \tau_0 exp\left(\frac{E_B}{k_B T}\right) \tag{1.3}$$

Where τ_0 is called the attempt time and is a material dependent parameter of the nanomagnet, ranging in value from 10 ps-1 ns [44].

Traditionally, nanomagnets are engineered to have a large E_B in order to increase their retention times. The magnetic hard drive industry uses nanomagnets with energy barrier 40-60 times the average thermal energy ($k_B T$). This ensures a retention time in several years, leading to the nonvolatile memory unit used in magnetic hard drives and now in the magnetoresistive random access memory.

In contrast to the approach used for memory applications, to achieve the stochastic element essential for the p-bit, nanomagnets are engineered to have low E_B. As seen

from eq. 1.3, for $E_B \rightarrow k_BT$, the retention times can be made as small as nanoseconds and the magnetization can show spontaneous fluctuations at GHz speeds. Eq. 1.3 is actually an approximation in the large E_B/k_BT regime, and should be substituted by more accurate expressions provided in ref. [45, 46]. However, the possibility of GHz fluctuations by reducing E_B/k_BT is well supported by this analysis as well. These fluctuations arise from the ambient thermal noise and hence are expected to be "truly random", as opposed to the pseudo random numbers generated from CMOS platforms, like linear feedback shift register (LFSR), that rely on a seed. Experimental design of low barrier nanomagnets out of industrially relevant magnetic stacks composed of CoFeB and Permalloy magnets, along with evaluation of their randomness quality is discussed in Chapter 3.

Three terminal device implementation of p-bit

The LBNM fluctuations form the basis of the stochasticity in p-bits. However, these fluctuations need to be converted to electrical signals (voltages or currents) in a three terminal device, to be useful in building circuits. Moreover, the fluctuations need to be tunable as described in Fig. 1.2. Fig. 1.3 shows two 3-terminal device implementations of p-bits with different "write units" to get the tunability and "read units" to convert the fluctuations into usable electrical signal. These implementations, named here as p-bit design A and design B are presented in detail in references [30] and [47] respectively.

Fig.1.3 (a) shows the schematic of p-bit design A, where the magnetic fluctuations are converted into a resistance fluctuation by using an MTJ whose free layer is an LBNM. As the LBNM fluctuates between a parallel and an anti-parallel orientation with respect to the fixed layer, the resistance across the MTJ shows fluctuations between a larger R_{AP} and a smaller R_P value due to the tunneling magnetoresistance (TMR) effect [21, 22]. This resistance fluctuation is converted into a fluctuating voltage (V_{OUT}) by using a normal resistor R_0 in series with the MTJ and using a

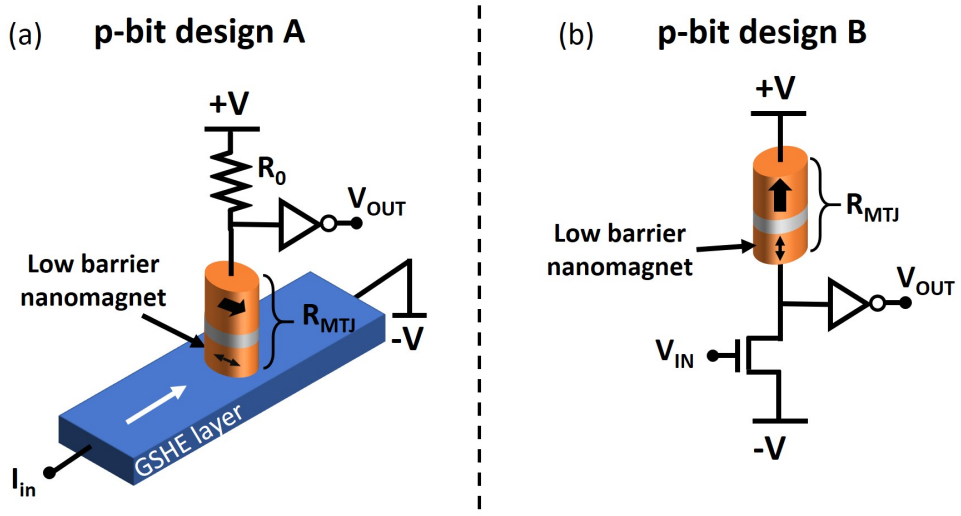

Fig. 1.3. Three terminal device implementations of the p-bit.

resistive divider scheme, which forms the read unit of the device. For tuning the average of the magnetization fluctuations, a giant spin Hall effect (GSHE) underlayer is introduced. An input charge current (I_{in}) to the GSHE layer produces a spin current that biases the LBNM free layer magnetization to be parallel with the spin polarization direction. By changing the magnitude and sign of I_{in}, the probability of the magnetization state being parallel or antiparallel to the spin polarization state can be tuned, hence forming the write unit. It should be noted that in plane anisotropy magnets are suitable as the free layer LBNM for this scheme as the generated spin currents that are responsible for the tunability are polarized in a direction that lie along the plane of the film. If perpendicular anisotropy magnets are used, achieving complete tunability of its magnetization state is non trivial but possible, as is shown in Chapter 3.

Fig.1.3 (b) shows the schematic of another, fundamentally different, three terminal device implementation of the p-bit, with a voltage controlled input. In this device, the read unit is still the resistive divider formed by the fluctuating MTJ resistance and the output resistance of the NMOS transistor. However, the tunability is achieved by tuning the output resistance of the transistor through its gate voltage, which forms

the input (V_{IN}) of the p-bit. For small V_{IN}, the transistor is OFF and hence the output voltage is pulled to $+V$. For large V_{IN}, the transistor is ON and its R_{out} is designed to be much smaller than R_P of the MTJ, which ensures that the V_{OUT} is pulled to $-V$. For intermediate V_{IN} values, the average resistance of the MTJ and the R_{out} of the transistor are matched and the MTJ fluctuations are converted to the fluctuations in V_{OUT}. Note that the tunability achieved in this device is through tuning the transistor output resistance, while the MTJ resistance always fluctuates between the R_P and R_{AP} states with 50% probability for each. This is in contrast to the previous device, where the tunability was achieved through the impact of spin orbit torque on the direction of the magnetization.

Both the above implementations have features that can be attractive depending upon the circuit implementation. The p-bit design B has voltages as its terminal quantities (V_{IN} and V_{OUT}) and hence could be more power efficient by avoiding the I^2R ohmic loss associated with current controlled devices. The GSHE controlled p-bit design A has a low impedance input terminal and uses currents as its inputs. Hence, it has a natural way to implement the weighted sum of outputs coming from other p-bits, which is a desirable feature for many neuromorphic architectures.

In addition to the above two considerations, there is a more subtle difference between the two p-bit implementations. In both p-bit design A and design B, the rate at which the output generates random numbers with the statistic controlled by the input current is determined by the fluctuation time scale, τ_{mag}, of the LBNM in the free layer of the MTJ. However, the time it takes for the output to go to either $+V$ or $-V$, depending on the input(called the step response time, τ_{step}), is controlled by the NMOS transistor delay in design B and is proportional to τ_{mag} in design A. The fact that state of the art transistors are much faster than the magnetization fluctuation rate in typical nanomagnets, we have $\tau_{step} \ll \tau_{mag}$. This point is described through numerical simulations in [45] and is an important consideration while designing networks of p-bits.

In both the device designs, there are two engineering challenges that need to be overcome for proper operation as a p-bit:

- **Read disturb:** the finite read current passing through the MTJ could potentially bias the generated random numbers at the output of the device due to spin transfer torque (STT) effect. This read disturb issue depends on the relative magnitude of the read current compared to the current (I_{pin}) required for complete pinning of the free layer LBNM. So, the important parameter here is I_{read}/I_{pin}.

- **Dipolar stray field:** the fixed layer of the MTJ produces a magnetic dipolar field on the free layer LBNM, thus biasing its orientation. The impact of this unwanted field is dependent on its relative magnitude in comparison with the pinning field of the LBNM. Hence, the important parameter here is B_{stray}/B_{pin}.

In this thesis, p-bit design A is the subject of experimental implementations. Chapters 3, 4 and 5 present different variations of this device. The write unit is implemented using the giant spin Hall effect of tantalum. The MTJ read unit is replaced by an experimentally simpler scheme of utilizing the anomalous Hall effect (AHE) to read out the state of a perpendicular nanomagnet, which also avoids the STT read disturb and the stray field issues. However, some of the experimental results obtained in Chapter 3 regarding single LBMN properties provide potential solutions to the two challenges listed above. Due to the weaker output voltage generated using AHE compared to that obtained from the MTJ, we utilize CMOS elements to amplify the output in order to concatenate it to other p-bits. It is to be understood that with the replacement of the AHE with MTJ based read mechanism, the CMOS amplifiers can be replaced by a single CMOS inverter [30, 47].

1.4 Thesis overview

Chapter 2 tests the suitability of thermally unstable nanomagnets "engineered in the laboratory" for converging to the theoretical minimum energy configuration of an

associated Ising Hamiltonian. The connectivity between the magnets was controlled by lithographically designing their separation. Although a small scale demonstration, the important conclusion from this study is that the nanomagnet network was able to converge the true ground state even in the presence of another energetically close local minimum. This motivates the experimental study of nanomagnet design for suitable p-bits that can be electrically controlled and interconnected instead of relying on fixed dipolar interaction.

Chapter 3 then explores the plethora of options available in nanomagnetism to design thermally unstable nanomagnets. Firstly, in plane anisotropy systems are studied, where stochasticity was achieved by two routes: (i) reducing the total magnetic moment and (ii) reducing the shape anisotropy. It was found that reducing the nanomagnet energy barrier by reducing shape anisotropy is advantageous in terms of reducing the "pinning field", i.e., making the output response easily tunable when external agent responsible for the tuning is an effective magnetic field. Secondly, perpendicular magnetic anisotropy systems are investigated. The CoFeB/MgO based perpendicular anisotropy systems provide a convenient method to tune the anisotropy by changing the magnetic layer thickness, due to the presence of the competition between a thickness dependent "interface anisotropy" and the standard demagnetization field. This property is exploited to design thermally unstable nanomagnets. An easy electrical read method, enabled by anomalous Hall effect, allowed the collection and study of large data sets for the quantification of the quality of random bits generated. Finally, the symmetry in response of perpendicular magnetization to in plane polarized spin current is utilized to generate random numbers by initializing thermally stable nanomagnets along their hard axes. Different from the spontaneously fluctuating unstable nanomagnets, this method produces random bits at a frequency dictated by that of the pulse train provided for hard axis initialization. This allows for a clocked circuit operation, as is presented in the next chapter.

Chapter 4 utilizes the hard axis initialization technique, and adds a simple "Oersted ring" to make p-bits that can be read from and written into electrically. Using

two such devices, Bayesian network building blocks are implemented. It is shown that the conditional dependency between two nodes of a Bayesian network can be represented by the electrical connection weights and biases between the two such p-bits. A case study with five different conditional probability tables, with wide ranging parameters are shown to be mimicked by the two p-bit network.

Chapter 5 studies the behavior of electrically coupled p-bits made out of thermally unstable perpendicular nanomagnets. First, a novel method to fully tune the state of the perpendicular magnetization using in plane polarized spin currents from spin orbit torque is demonstrated. A slight tilt in the anisotropy of the nanomagnet is hypothesized to be the reason for the observed tunability, with experiments and numerical simulations testifying the hypothesis. Taking advantage of this phenomenon, an electrically addressable p-bit with spontaneously fluctuating output is designed by the use of CMOS peripheral elements to amplify the signal. The two such devices are connected in a unidirectional way to study the temporal relation between their fluctuating outputs. There were two important findings from this study: (i) finite correlations between the two p-bit outputs were established with a weak coupling current that is an order of magnitude smaller than that required for deterministic switching at zero temperature. (ii) the correlation was established despite a large difference (more than two orders of magnitude) in the natural time scales of the two devices.

Chapter 6 studies some other interesting properties of the p-bits described in chapter 5. It is shown that the random fluctuations at the output of the p-bit can be made to synchronize in phase to sub-threshold sinusoidal current excitations, when the frequency of the sinusoid matches the average fluctuation frequency of the nanomagnet. This is the signature of a phenomenon known as stochastic resonance observed in many physical systems, but is demonstrated using spin orbit torque on a perpendicular nanomagnet for the first time. Further, by introducing an electrical feedback of the device output to its input, the synchronization frequency is shown to be tunable.

Chapter 7 and 8 are on two projects undertaken during the course of this PhD work, which are not directly related to probabilistic computing or the study of p-bits, but are experiments that take advantage of the physical phenomena in the field of spintronics to engineer a prototype logic device (chapter 7) and to improve the performance of an existing memory device (chapter 8).

Chapter 7 presents the design and experimental demonstration of a prototype logic device, based on the idea of deterministic charge spin logic [48]. A composite stack composed of an in plane anisotropy and a perpendicular anisotropy magnet is designed. The information stored in the state of the in-plane magnet (the write unit) is transferred to the perpendicular magnet (the read unit) through a weak symmetry breaking dipolar field (the coupling mechanism). Field free, fully electrical operation of the device is demonstrated. The main conclusion from this study was that the use of a symmetry breaking field to transfer information from the write to the read unit alleviates the strict requirement of a strong dipolar coupling, which is an integral part of the charge spin logic device.

Chapter 8 focuses on the improvement of charge to spin conversion efficiency of tantalum, an industrially relevant material for magnetoresistive random access memory applications. It is shown that the insertion of a monolayer of WSe_2 under the tantalum layer improves the spin Hall angle by more than 25 times in ultra thin tantalum. Harmonic Hall measurements performed in this study suggest that the suppression of spin back diffusion from the tantalum back interface is a possible reason for the observed improvement.

Chapter 9 summarizes the contributions of this thesis and discusses the path moving forward.

2. NANOMAGNET NETWORKS AS HARDWARE FOR ISING COMPUTING

Most of the materials in this chapter have been extracted verbatim from the paper: Debashis, Punyashloka, et al. "Experimental demonstration of nanomagnet networks as hardware for ising computing." Electron Devices Meeting (IEDM), 2016 IEEE International. IEEE, 2016.

The work presented in this chapter tests the suitability of using stochastic nanomagnet networks for Ising computing. The idea here is to map a given problem to a physical system [49] and then "anneal" the system towards its ground state, which becomes the optimum solution. Yamaoka et al. demonstrated an all CMOS implementation based on a similar idea [12], which comes at a high cost in terms of hardware resource and memory for implementation of a single spin and its nearest neighbor coupling. By performing statistical experiments, matched by theory and extensive simulations, we demonstrate for the first time that using geometrical designs to control dipolar-coupling strengths, a nanomagnet network can be related to an Ising Hamiltonian and that the most probable configuration of the system corresponds to the ground state of that Hamiltonian.

2.1 Realizing a stochastic building block

In this study we first adopted hard elliptical magnets employing the randomization method used by Morgan et al. [50] as means to study network statistics. Elliptical nanomagnets with shape anisotropy have two well defined low energy states, separated by a barrier that is directly proportional to the volume of the magnet. During the growth of these nanomagnet islands, below a certain thickness, the energy barrier between the two states for individual magnets are small enough to be overcome by

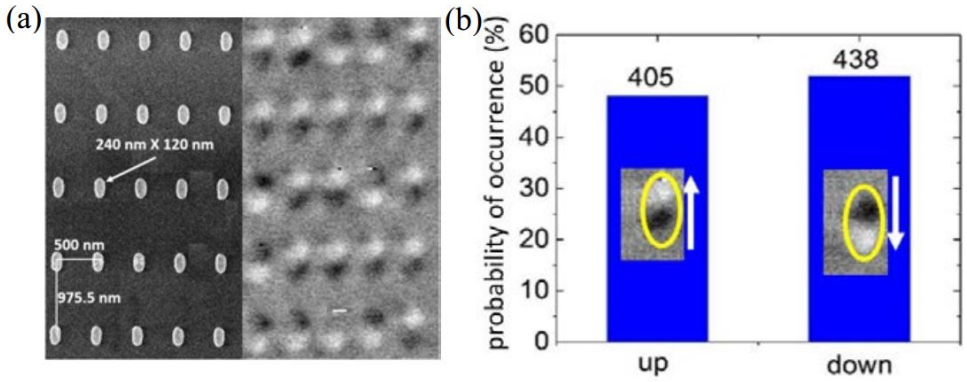

Fig. 2.1. **Stochastic elliptical nanomagnets:** (a) SEM image (left half) and MFM phase contrast plot (right half) of an array of isolated elliptical magnets. The individual magnet islands get randomized during growth due to thermal fluctuation. (b) Histogram obtained from MFM phase plot showing almost 50%-50% distribution of magnets point up or down at zero bias.

thermal fluctuations. Hence an array of such nanomagnets behaves as a superparamagnetic ensemble whose dynamics slows down as the thickness increases and eventually gets frozen once the thickness crosses a threshold during the growth. This process is equivalent to "annealing", which is another required feature of a probabilistic network in order to smoothly transition into its ground state without getting stuck at a local minimum. We observed that the lateral size of the magnets as well as the growth substrate strongly influence the randomness of the frozen super-paramagnetic array. By properly designing both these parameters, we show that the array produces a nearly 50- 50% binary probability distribution that is essential for the building blocks of any Ising model (fig. 2.1).

2.2 Probabilistic Ising network implementation

In the following two experiments, we demonstrate how weak dipolar coupling can be used to manipulate the probability distribution of nanomagnet networks (fig. 2.2). By comparing experimental results with the solution of the associated Ising Hamil-

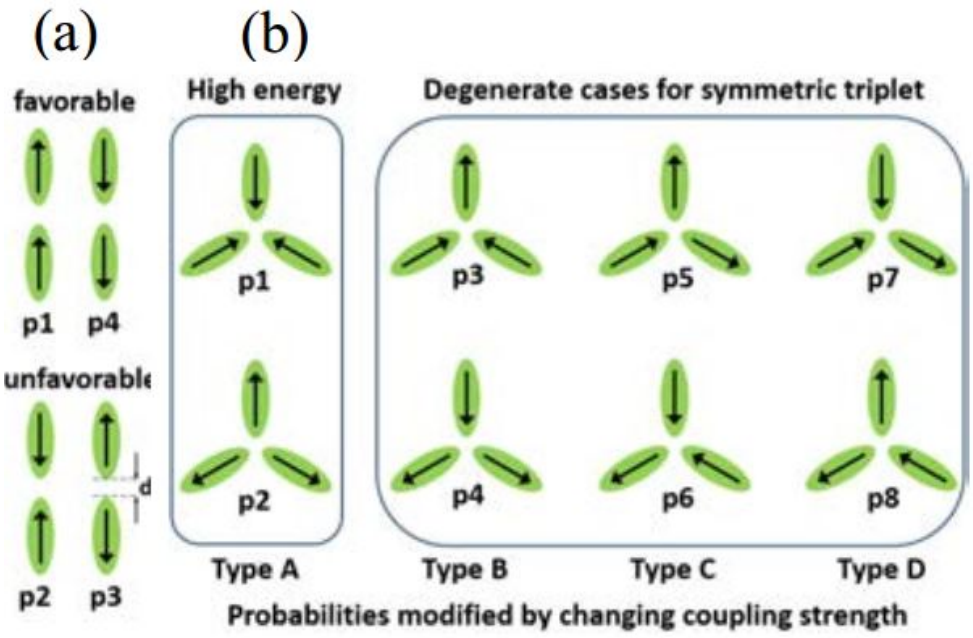

Fig. 2.2. **Nanomagnet configuration studied:** (a) for controlling coupling strength in nanomagnet pairs and (b) for controlling frustration in a nanomagnet triplet.

tonian, we show that the nanomagnet network is a physical implementation of that Ising network and produces the ground state solution with high probability. The results are also well matched to stochastic Landau-Lifshitz Gilbert (LLG) simulations, suggesting that the dynamics is essential to achieve the ground state, as explained later.

2.2.1 Controlling coupling between a nanomagnet pair

First, we demonstrate that for two longitudinally placed nanomagnets at separations larger than that required for deterministic switching, the probability distribution can be affected by weak dipolar coupling. At any stage of the experiment the separation between magnets is kept large enough to ensure that the dipolar coupling field between magnets is around five times lower than their coercive fields as shown in fig. 2.3 (a), (b). For well-separated pairs, all four magnetic configurations are nearly

degenerate and hence are equi-probable. However, when we reduce the separation, dipolar interaction lifts this degeneracy and the parallel cases become energetically more favorable, directing the probability distribution. This can be seen by the decrease in probabilities of the anti-parallel cases (p2 and p3) and increase in that for the parallel cases (p1 and p4), as shown in fig. 2.4. Both the Ising Hamiltonian solution and stochastic LLG simulations give well matched results. Since the coupling field is much weaker than the coercive field of the magnets, the stochastic behavior of the nanomagnet pairs during growth is essential to obtain a probability distribution of this type.

2.2.2 Controlling frustration in a nanomagnet triplet

To study a nontrivial system, asymmetric nanomagnet triplets were designed, i.e., the separations between all three magnets are different. This is a nontrivial case of reduced frustration in which the probabilities change depending on the coupling strengths. Through magnetic force microscopy (MFM) analysis, the probabilities were found to weekly obey the Ising rule, i.e., all in and all out configurations were the least favorable. While the other six configurations should be equally probable for the case of a perfectly symmetric triplet, by slightly altering the arrangement of the three magnets, we introduced an asymmetric interaction. The closest pair should influence the probability distribution most. Indeed, that is observed in our MFM results (fig. 2.5). p3 and p4 correspond to cases in which the closest pair is facing the same direction with respect to the center. Hence, these cases are the least probable. p5 and p6 correspond to similar cases for the next closest pair and are hence the next least probable ones. p7 and p8 correspond to the farthest pair and hence have the highest probabilities. The solution for the Ising Hamiltonian of this system matches well with the experiment, which suggests that the system is able to reach its ground state efficiently. During the super-paramagnetic phase, the system explores every possible configuration before settling into the energetically

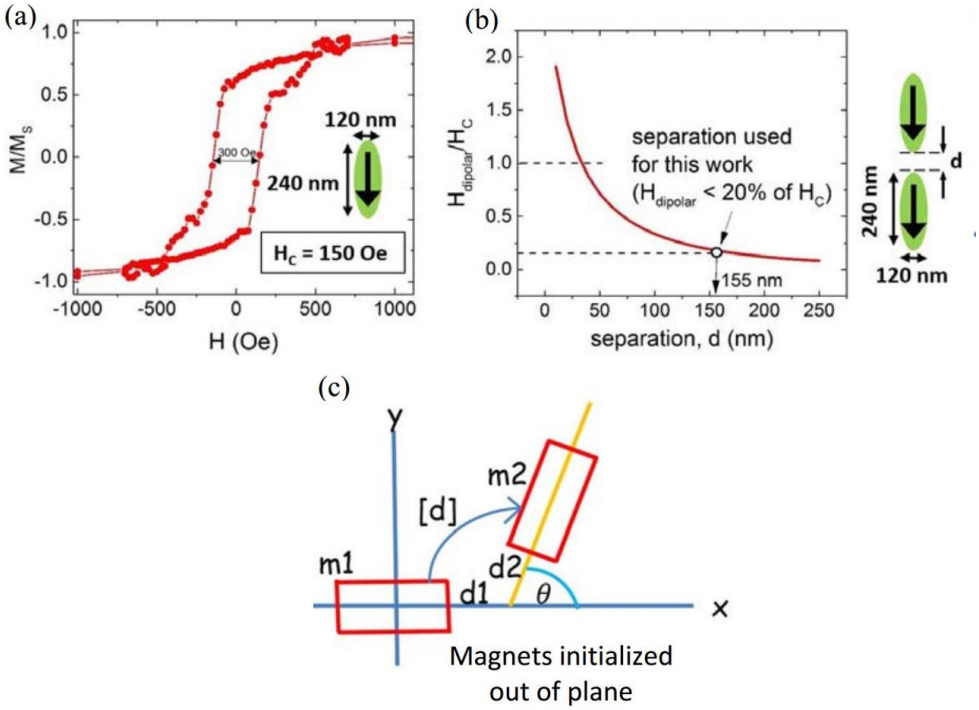

Fig. 2.3. **Ensuring weak coupling:** In order to design the spacing between nanomagnets to introduce week coupling, a knowledge of the coercive field of individual magnets is important. We fabricated a large array (1 million elements) of non-interacting nanomagnets, each of size 120nm x 240nm on Si3N4 substrate. (a) VSM characterization, done on the array, is reflective of individual magnet property. The coercive field of individual magnets was obtained to be 150 Oe. (b) simulated graph of the field exerted on such a nanomagnet due to another at a separation of 'd' from it. We designed our networks such that the interaction field between magnets is around five times lower than the coercive field, hence eliminating the possibility of flipping of nanomagnets deterministically. (c) Schematic of the stochastic LLG simulation setup. The magnets are assumed rectangular bar magnets. The dipolar field at magnet due to magnet can be written as $h_i^d = [d]_{ij} m_j$ where $[d]_{ij}$ is the dipolar tensor and m_j is the magnetization of magnet j. All magnets were initialized out of plane and let to relax under the influence of thermal noise and this dipolar field.

most favorable one when the magnetic islands grow past a certain thickness. At this point the configuration gets frozen, with the ensemble statistics reflecting the temporal statistics of the superparamagnetic regime.

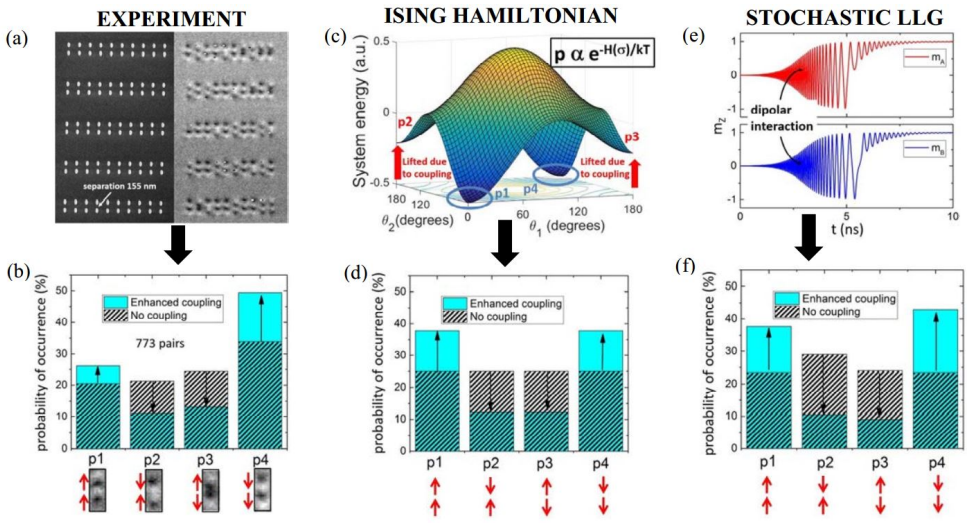

Fig. 2.4. **Coupled magnet pair:** (a) SEM image (left half) and MFM phase contrast plot (right half) showing magnets to be in up or down state. (b): Histogram obtained from the MFM phase images, showing skew in probability distribution towards parallel configuration as weak coupling is introduced in the system. (c) Energy landscape of the magnet pair with lifted quadruple degeneracy. (d) Histogram obtained from the energy levels of the four possible configurations. Rise in energy levels of anti-parallel configurations correspond to decrease in p2 and p3. (e) stochastic LLG simulation with hard axis initialization (physical parameters taken from experiment). (f) Histogram obtained from an ensemble of such LLG simulations. Dipolar interaction during the transient evolution guides the system to towards its low energy state.

2.3 Theoretical framework

(NOTE: The theoretical work and simulations were done by Rafatul Faria.)

Our experimental observations are in excellent qualitative agreement with theoretical estimates based on (A) configuration energies obtained from the Ising Hamiltonian, and on (B) stochastic LLG simulations including thermal noise. Note: The work presented in this section is performed by Rafatul Faria, the second author of the paper on which this chapter is based.

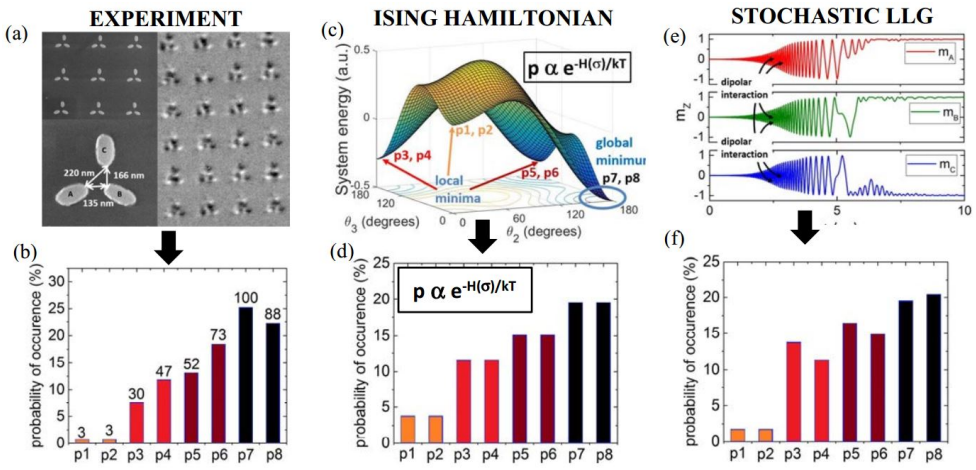

Fig. 2.5. **Coupled magnet triplet:** (a) SEM image (left half) and MFM phase contrast plot (right half) showing magnets to be in 'in' or 'out' state. (b) Histogram obtained from MFM phase, showing reduced frustration (p3-p8 unequal). (c) Energy vs. magnetization angle w.r.t own easy axes for the three magnet system (1 is fixed at 0 degree for plotting purpose) (d) Histogram obtained from Ising Hamiltonian energy levels. Despite three of the four minima being closely spaced in energy, the system does not get stuck at these and produces the true ground state with maximum probability (e) Time domain response of magnetizations (from LLG with hard axis initialization) for a representative case. (f) Histogram obtained from stochastic LLG simulation with physical parameters taken from experiment. The experimental probabilities follow the same trends as the theoretical models, suggesting that the nanomagnet network mimics an Ising network that can be configured by designing the coupling strengths between individual elements. Also, the system is able to come out of local minima due to an effective annealing during its transient evolution.

2.3.1 Ising Hamiltonian implementation

The normalized energy of a system of magnets can be written as:

$$E = \sum m_i[n]_i m_i + \sum 2m_i[d]_{ij} m_j \tag{2.1}$$

where $[n]$ is the demagnetization tensor and $[d]$ is the dipolar tensor. Assuming that the magnetizations of all magnets are constrained to lie along their easy axes in equilibrium, the energy can be approximated by a general Ising Hamiltonian:

$$H = -\sum J_{ij} s_i s_j - \sum h_i s_i \tag{2.2}$$

with magnetizations m_i, m_j playing the role of s_i, s_j and where the coupling coefficient J_{ij} and bias h_i can be defined as:

$$J_{ij} = J_{ji} = 2(d_{xx}^{ij} cos(\theta_{ij}) + d_{xy}^{ij} sin(\theta_{ij})) \tag{2.3}$$

Here $h_i = 0$; d_{xx}^{ij}, d_{xy}^{ij} and θ_{ij} are the dipolar tensor components and angle between m_i and m_j. Classically, each spin configuration $\sigma(s_i)$ has a probability of occurence $(1/Z)e^{-H(\sigma)/k_B T}$. In our experiment, d_{xx}^{ij}, d_{xy}^{ij} and θ_{ij} can be controlled by manipulating the magnet dimensions, separations, and their relative alignment, resulting in a controlled probability distribution of different polarization configurations.

2.3.2 Stochastic LLG simulations

We have carried out stochastic LLG simulations to compare with the experimental results. In the simulation, a network of inplane magnets having shape anisotropy based large energy barriers, is forced to point out of the plane by application of a large external magnetic field. When the magnetic field is removed, the magnets in the network are then allowed to fall into one of the two possible in-plane directions along their own easy axes under the influence of thermal noise and dipolar coupling field (fig. 2.3 (c)). While for an isolated magnet, both magnetization directions are equally probable, for a network of magnets, during the relaxation process, the energy landscape of the configuration influences the probability distribution. Since the coupling strength depends on the in-plane component of the magnetization, it is small to begin with and gradually increases as the magnets fall towards their in-plane easy axis, mimicking the "annealing" during growth. This is captured by the energy term introduced by the dipolar tensor in the LLG equation.

2.4 Conclusion

We have demonstrated that nanomagnets satisfy two important features of a probabilistic computing network, i.e., (i) being a stochastic building block, and (ii) allowing for controllable coupling which permits mapping problems to the physical system. By introducing coupling through spin currents or other reconfigurable controls, such blocks can be interconnected to solve complex optimization problems such as the Travelling Salesman Problem [38] among others that can be mapped to an Ising Hamiltonian.

Acknowledgment

This project was supported by the Nanoelectronics Research Corporation (NERC), a wholly-owned subsidiary of the Semiconductor Research Corporation (SRC), through the Institute for Nanoelectronics Discovery and Exploration (INDEX).

3. DESIGN OF STOCHASTIC NANOMAGNETS AS P-BITS FOR PROBABILISTIC SPIN LOGIC

Most of the materials in this chapter have been extracted verbatim from the papers: Debashis, Punyashloka, et al. "Design of Stochastic Nanomagnets for Probabilistic Spin Logic." IEEE Magnetics Letters 9 (2018): 1-5. and Debashis, Punyashloka, et al. "Correlated fluctuations in spin orbit torque-coupled perpendicular nanomagnets.", in press, Physical Review B (2020).

The simulations presented in this chapter were performed by Rafatul Faria.

Probabilistic spin logic (PSL) is a new computing paradigm that has been theoretically shown to be more suitable than conventional CMOS for performing tasks such as intrinsic optimization, probabilistic inference from Bayesian networks, and invertible Boolean logic [30, 34, 38, 51, 52]. PSL relies on unstable stochastic bits called probabilistic bits (p-bits) that are essentially random signal generators with a tunable mean output. They can either be analog (generating any random values between "0" and "1") or binary random number generators (generating randomly "0" or "1").

3.1 Designing p-bits from in plane anisotropy magnets

A stochastic nanomagnet with low barrier energy E_B can form a natural hardware for implementing the p-bit as its magnetization randomly fluctuates between its metastable states with an average retention time of [44]:

$$\tau = \tau_0 exp\left(\frac{E_B}{k_B T}\right) \tag{3.1}$$

where τ_0 is the material-dependent parameter called the attempt time of the nanomagnet. The most commonly stated value for τ_0 in the literature is generally assumed to be between 100 ps to 1 ns [44]. Hence, a low-barrier nanomagnetbased p-bit with

$E_B \approx k_BT$ can produce random numbers at gigahertz speed. The mean value of magnetization (and as a result, the mean of the produced random numbers) can be tuned by an external input, such as spin current from the giant spin Hall effect (GSHE) [30, 38, 51], spin transfer torque (STT) [53, 54], or an effective magnetic field from the magnetoelectric effect [55]. The ease of tunability is judged by evaluating the input required to pin the fluctuating magnetization state to one value. For example, the magnitude of the effective magnetic field generated by the electric field in the case of voltage control of magnetization [56] is an important metric for energy efficiency to achieve low-power computation. Significantly, both speed and energy consumption of the p-bit can be carefully engineered through proper design of the nanomagnet involved in the device. In this letter, the following three methods to obtain stochastic nanomagnets have been explored: (1) by reduction of anisotropy; (2) by reduction of net magnetic moment; and (3) by hard-axis initialization. In conjunction with Boltzmann theory and stochastic Landau–Lifshitz–Gilbert (sLLG) simulations, the first two methods are compared in terms of pinning field and speed.

3.1.1 Stochasticity by scaling moment and scaling anisotropy

In order to make a fast stochastic nanomagnet that randomly fluctuates with an average retention time of 1 ns, its energy barrier E_B needs to be scaled to k_BT , according to (1). Since E_B is a product of the anisotropy field H_K and the net moment $M_S \times Vol.$, both can be reduced to achieve an energy barrier of k_BT. The response of such stochastic nanomagnets to magnetic fields can be captured by the following analysis based on the Boltzmann law. The energy of a magnet in the macrospin limit under the application of an external B-field, H_{ext}, can be written as

$$E = 2\pi M_S^2(Vol.)m_x^2 - H_{ext}M_S(Vol.)m_z - \frac{1}{2}H_K M_S(Vol.)m_Z^2 \tag{3.2}$$

where $m_X = sin(\theta)cos(\phi)$ is the magnetization along the out of plane hard axis (x), $m_Z = cos(\theta)$ is that along the easy axis (z), θ being the angle of the magnetization direction with respect to the easy axis, M_S is the saturation magnetization, H_K is

the uniaxial anisotropy along the z-axis, and $Vol.$ is the volume of the magnet. The first, second, and third terms are contributions from the shape anisotropy, external magnetic field, and uniaxial anisotropy field, respectively. The probability of finding the magnetization in (θ, ϕ) configuration can be found by the equilibrium Boltzmann distribution

$$p(\theta, \phi) = \frac{1}{Z} exp\left(-\frac{E}{k_B T}\right) \tag{3.3}$$

where Z is a normalization constant. The average magnetization along the z-axis can be written as

$$\langle m_Z \rangle = \frac{\int\int d\phi d\theta p(\theta, \phi) cos(\theta) sin(\theta)}{\int\int d\phi d\theta p(\theta, \phi) sin(\theta)} \tag{3.4}$$

Based on the above-mentioned equations, fig. 3.1 shows the plot of the field that is required to pin a stochastic nanomagnet as we scale its energy barrier. Scaling the H_K results in almost negligible change in pining field. However, scaling moments to smaller values results in much larger corresponding pinning fields. The inset of fig. 3.1 considers two magnets with $E_B = 1 k_B T$ obtained by reducing H_K (red curve) and $M_S \times Vol.$ (blue curve), respectively. Compared to a stable 40 $k_B T$ magnet, the first magnet has 40 times smaller H_K and the second has 40 times smaller moment. Even though both magnets have the same E_B, leading to the same time scale of fluctuation (τ), the field required to pin the low H_K is appreciably smaller than that for the low $M_S \times Vol.$ magnet (see inset of fig. 3.1). Since this translates to a smaller energy requirement in a voltage-driven PSL [55] circuit, designing stochastic nanomagnets by reducing anisotropy seems to be the better option compared to reducing the volume. We then go on to test this theoretical prediction experimentally. To compare the effect of reduced anisotropy versus reduced volume, it would be ideal to fabricate the two 1 $k_B T$ magnets, as described previously. However, in practice, it is challenging to make two stochastic nanomagnets that are 40 times different in net moment. Therefore, two nanomagnets that are about 4 times different in their net moment are fabricated in the following experiments.

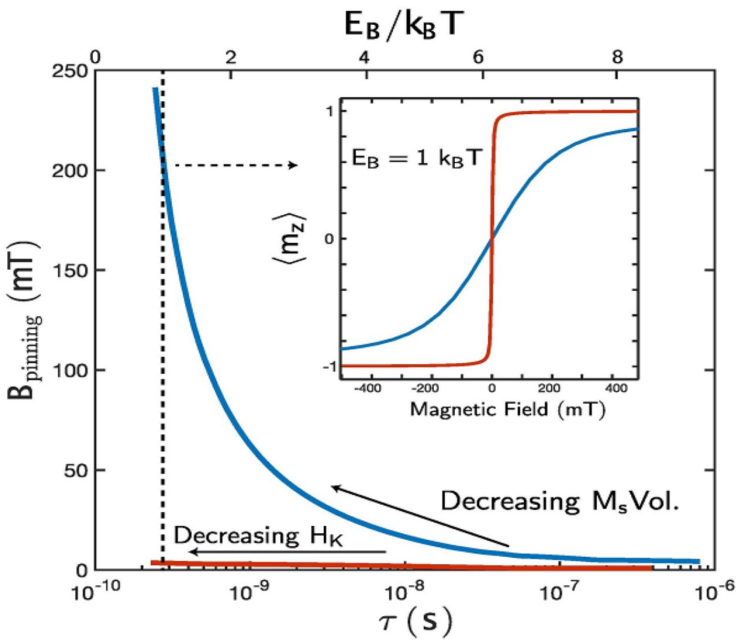

Fig. 3.1. **Pinning field versus the speed of fluctuation:** Calculations based on Boltzmann law show that making magnets faster by scaling anisotropy (red curve) is more efficient than scaling net moment (blue curve) in terms of the field required to pin the scaled magnet. The inset shows the average magnetization versus B-field for a 1 k_BT magnet. It suggests that the pinning field is much smaller for the case of magnet B (red curve) compared to magnet C (blue curve).

Achieving Stochasticity by Reducing Anisotropy

Experimentally, a low H_K magnet is realized by a circular disk magnet of $Co_{60}Fe_{20}B_{20}$ with a diameter of 110 nm and thickness of 1.3 nm. Circular disk in-plane magnets have been proposed as p-bits [51, 57], as they fluctuate in random in-plane directions as a function of time. Such a stochastic element has been realized in our experiments with monodomain circular disk nanomagnets [57, 58] with careful material and design choices, guided by the trade off between exchange stiffness and dipolar self energy [59]. Starting from a sputter deposited stack of Ta(15)/CoFeB(1.5)/MgO(1)/Ru(4) (thicknesses in nanometers), an array of 25 million nominally identical circular disk nanomagnets is fabricated using e-beam lithography and Ar ion milling. Then, their

response is measured using a superconducting quantum interference device in Quantum Design MPMS-3. Fig. 3.2 (a) shows the scanning electron microscopy (SEM) image of a portion of the array. Fig. 3.2 (b) shows a hysteresis-free, sigmoidal output curve of the average magnetization of the array. It should be noted here that although the average steady-state behavior is determined completely by the applied magnetic field, the time-domain behavior of each nanomagnet is stochastic, owing to their low energy barrier. Such individually stochastic units whose average behavior exhibits a sigmoidal response as a function of an input parameter can be used as a building block for a class of stochastic neural networks in machine learning [31] among other PSL applications.

Achieving Stochasticity by Reducing moment

Next, an array of 100 million elliptical nanomagnets is fabricated using e-beam lithography, physical evaporation of Permalloy (Py), followed by liftoff. Since they are elliptical, shape anisotropy [60] creates a large H_K . Hence, to reach stochasticity, the net moment has to be reduced to obtain small E_B. This is achieved in our magnets with dimensions of 49 nm $\times$ 61 nm $\times$ 5 nm. Also, through heat treatment (heating to 400 K for 1 h, then at 500 K for another hour, followed by cool down to room temperature, all at 150 mTorr pressure in Helium), reduced saturation magnetization of 250 kA/m is obtained for our Py nanomagnets. Fig. 3.2 (c) shows the SEM picture of an array of such nanomagnets. At 300 K, E_B is small enough to make the magnets stochastic, resulting in a sigmoid curve shaped normalized magnetization shown in fig. 3.2 (d) with black curve. Using experimentally measured saturation magnetization and magnet volume, H_K of 25 mT can be extracted by fitting the curve with a sigmoid function obtained from the Boltzmann law. This then results in $E_B 9 k_B T$ and consequently $\tau = 8\mu s$ (assuming $\tau_0 = 1$ ns). Since our conclusion from this experiment relies on the fact that these elliptical magnets have large anisotropy, H_K obtained from fitting needs justification. To ensure that the fitted value of H_K

is reasonable, further measurements at reduced temperatures are carried out. A sigmoidal response is still observed at T = 200 K with a sharper slope (see fig. 3.2 (d), red curve), consistent with the expectation from the Boltzmann law. Finally, at T = 100 K, magnets are essentially frozen and the ensemble behaves like a ferromagnet, showing hysteretic magnetization response to the applied field with a clear remanence at B = 0 T (see fig. 3.2 (d), blue curve). Considering the saturation magnetization, magnet volume, and the fact that the magnetization of these nanomagnets transition from being stochastic to stable in a temperature window between 100 K and 200 K, the bounds for H_K are estimated to be between 10 and 30 mT, which is consistent with the fitted H_K value of 25 mT. Both sigmoidal curves at 300 and 200 K show excellent agreement with the Boltzmann law using the same set of H_K and M_S with temperature corrections.

Comparing the Two Methods

Using the experimentally measured values of M_S and $Vol.$, the net moment $M_S \times Vol. = 1.2 \times 10^{17} Am^2$ and $0.3 \times 10^{17} Am^2$ are calculated for the CoFeB circular disk magnet and the Py elliptical magnet, respectively. As expected, when the two scaling methods are compared in fig. 3.2 (e), the pinning field for the circular disk magnet is 20% smaller than that of the elliptical one, despite its $M_S \times Vol.$ being 4 times larger. This is also confirmed by stochastic LLG simulations. The excellent agreement between experiment, Boltzmann law, and stochastic LLG simulations for both circular disk and elliptical magnets is shown in fig. 3.2 (e). Since the circular disk magnet has negligible E_B because of the absence of a shape anisotropy, as long as the circular disk magnet is small enough to behave as a monodomain body by avoiding vortex formation, its fluctuation time scale is limited by τ_0, unlike the elliptical magnet [eq. 3.1]. Hence, the circular disk magnet is both faster and consumes lower energy by requiring a smaller pinning field, compared to the elliptical magnet.

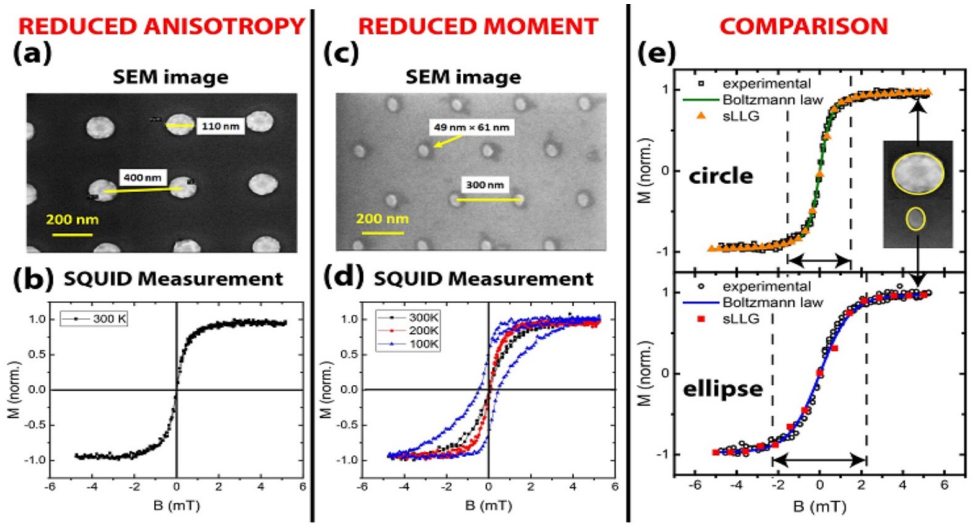

Fig. 3.2. **Two methods of reducing energy barrier:** anisotropy reduction and net magnetic moment reduction. (a) SEM of the array of CoFeB circular disk magnets. (b) Normalized magnetization response to applied magnetic field. The sigmoid shape with no remanence at zero field and saturation behavior is reminiscent of tunable stochastic behavior. (c) SEM of the array of Py elliptical magnets. (d) Normalized magnetization response to applied magnetic field for various temperatures. The sigmoid gets sharper for a lower temperature and eventually a hysteresis behavior is observed as the magnet fluctuations slow down. (e) Comparison of the two magnet behaviors matched with predictions by LLG simulations and Boltzmann law with experimental parameters. The required pinning field for the circular disk magnet is 20% less compared to that for the elliptical magnet, despite the fact that the former magnet has 4 times more $M_S \times Vol.$ compared to the latter magnet.

3.2 Designing from p-bit from weak anisotropy perpendicular magnets

The thermal stability factor of a nanomagnet is given by E_B/k_{BT}, where $E_B = K_{eff}V/2$ is the energetic barrier separating the two stable magnetization states. Here, K_{eff} is the effective anisotropy energy density and V is the volume of the nanomagnet. When E_B is comparable to the ambient thermal energy k_{BT}, the magnetization randomly fluctuates between the two stable states, thus realizing a "stochastic nanomagnet".

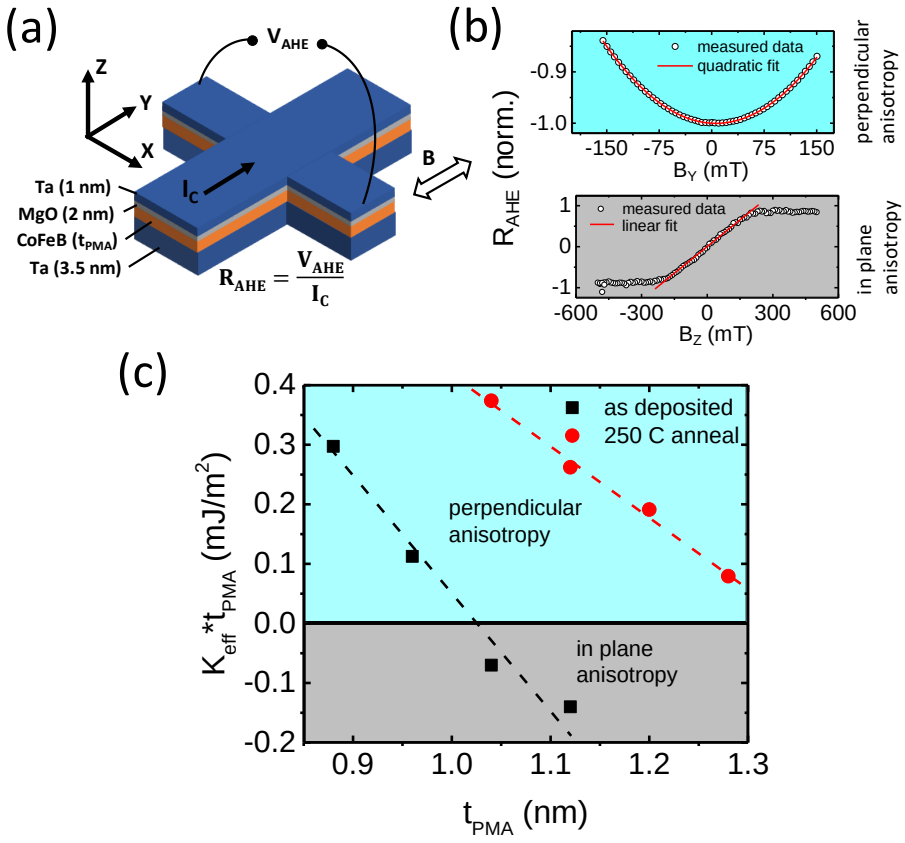

Fig. 3.3. (a) PMA stack with varying CoFeB thickness. (b) Anomalous Hall resistance as a function of magnetic field along the hard axis. For a PMA magnetic stack, the field is applied in the in-plane direction and the measured data are fitted with a parabolic curve to extract the effective anisotropy field (H_K). For an IMA magnetic stack, the field in applied perpendicular to the plane and the resultant plot is fitted with a linear fit to extract H_K (c) $K_{eff} \times t_{PMA}$ as a function of CoFeB layer thickness before and after 250^o C anneal.

We first engineer K_{eff} of our magnetic material (CoFeB) by varying the thickness (t_{CoFeB}) of the deposited PMA films, shown in fig. 3.3 (a). The anisotropy of such a stack is given by [27]:

$$K_{eff} = \frac{K_i}{t_{CoFeB}} - \frac{M_S^2}{2\mu_0} \tag{3.5}$$

arising from the competition between the interface anisotropy (K_i) and the demagnetization ($\frac{M_S^2}{2\mu_0}$) [27]. We then follow the method used by Hayashi et al. [61] to

characterize K_{eff} of our stacks, as shown in fig. 3.3 (b). For films with out-of-plane anisotropy, the obtained anomalous Hall resistance (R_{AHE}) in the presence of an in-plane magnetic field is fitted with a second order curve to obtain H_K (where H_K is the effective anisotropy field, given by K_{eff}/M_S). For films that have net in-plane anisotropy, H_K is obtained through a linear fit of the R_{AHE} vs. out-of-plane field curve. We observe a clear decreasing trend of $K_{eff} \times t_{CoFeB}$ vs. t_{CoFeB} for as deposited films as well as samples annealed at 250^o C for one hour, as shown in fig. 3.3 (c). The annealed stack with t_{CoFeB}=1.3 nm, corresponding to the lowest K_{eff}, is then chosen to fabricate the stochastic nanomagnet devices. The fabricated devices consist of lithographically defined PMA nanomagnets with a diameter of 100 nm on top of tantalum (Ta) Hall bars, as shown in fig. 3.4 (a). The combination of low K_{eff} through the thickness optimization and low volume through the lithography patterned small diameter results in a small E_B at room temperature. Consequently, these uniquely designed stochastic nanomagnets fluctuate randomly between the "UP" and "DN" magnetic states as depicted in the cartoon in the top right inset of fig. 3.4 (b). This random fluctuation is electrically read out through the anomalous Hall effect (AHE), giving the random telegraphic signal as the output, shown in fig. 3.4 (c). The magnetization dwell time in the UP and the DN state forms a distribution that is well fitted by an exponential envelope (fig. 3.4 (d)), which suggests that the fluctuation is a random Poisson process [54].

Please note that the intermediate states observed in fig. 3.4 (c) are artifacts of the finite lockin averaging time of 3ms. Any magnetization flip that occurs during this averaging window shows up as an intermediate state. The device shown in fig. 3.4 (a) has an average dwell time of 50 ms. So, the probability that a random flip occurs during a 3ms time window is = 3/50. In the full measurement set of 10000 data points, we notice that number of intermediate points/ total number of measurement points is almost equal to this ratio. Fig. 3.5 below shows the segregation of the measurement data points into "intermediate states" and "correct states" based on the distribution histogram.

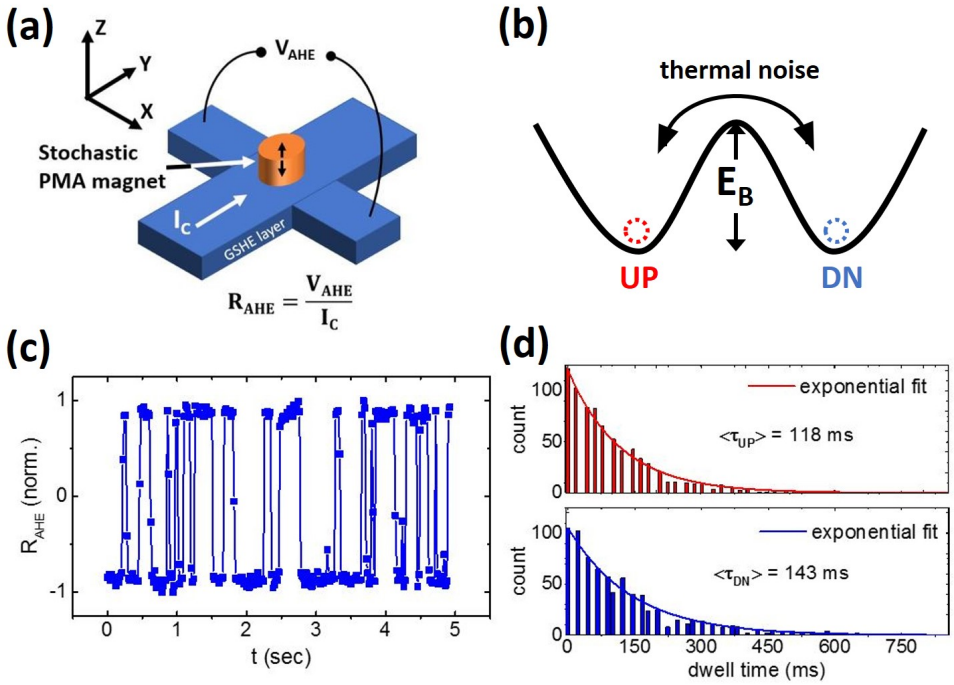

Fig. 3.4. (a) Schematic of the fabricated AHE Hall bar device with a 100 nm x 100 nm nanomagnet island defined on top by lithography and etching. A charge current (I_C) through the Hall bar (y-axis) produces a voltage (V_{AHE}) across the transverse electrode (x-axis). The anomalous Hall resistance (R_{AHE}) tracks the magnetization. (b) Energy barrier between the two states ("up" and "down") of the magnetization is small enough to be overcome by thermal energy at room temperature to produce random fluctuations.(c) A small section of the time varying R_{AHE} measured. It follows a random telegraphic noise as the magnetization flips randomly between the two "up" and "down" states. (d) Histograms of dwell time for "up" and "down" states, showing good agreement to an exponential fit, corresponding to a Poisson distribution.

3.2.1 Speed of fluctuation

Average dwell time in the UP and DN states, i.e. τ_{UP} and τ_{DN} are obtained from the exponential fitting. For a completely symmetrical energy landscape, these two dwell times should be identical. However, we obtain a slightly skewed distribution due to the remanent magnetic field in the measurement setup. The speed of the random

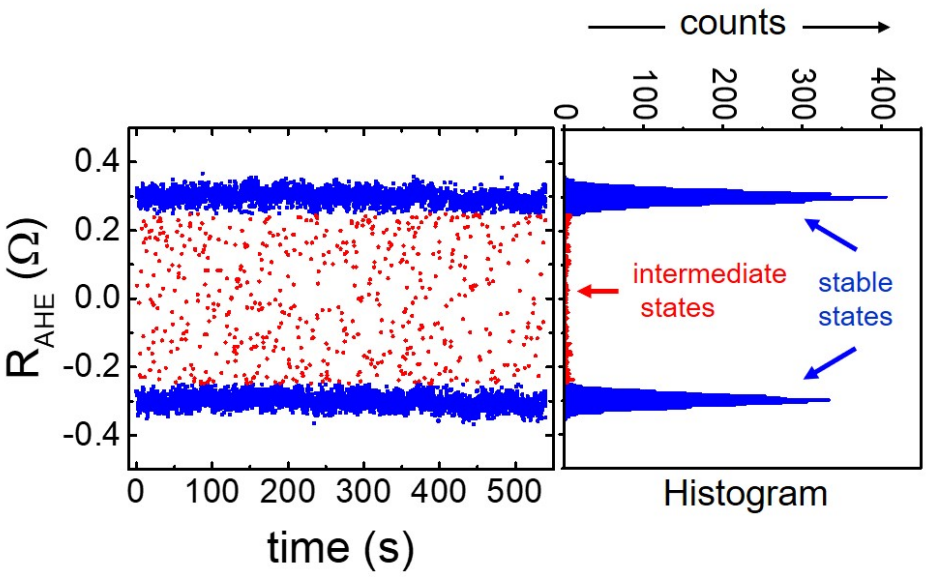

$$\frac{\#\ intermediate\ states}{\#\ total\ states} = \frac{579}{10023} \approx \frac{3}{50} = \frac{\tau_{lockin}}{\tau_{magnet}}$$

Fig. 3.5. The random telegraphic output observed in separated into "correct states" and "intermediate states" based on the histogram of distribution. The distribution of the measured R_{AHE} values clearly shows two peaks corresponding to the UP and DN states (blue points), and some intermediate states (red points).

bit generation can be obtained from the harmonic mean of τ_{UP} and τ_{DN}: $\tau^{-1} = \tau_{UP}^{-1} + \tau_{DN}^{-1}$. This time scale is determined by the energy barrier of the nanomagnet through:

$$\tau = \tau_0 exp(\frac{E_B}{k_B T}) \tag{3.6}$$

Hence, the speed of the random number generation can be increased by reducing the thermal stability factor, $\frac{E_B}{k_B T}$. From the obtained τ, we determine $\frac{E_B}{k_B T} \approx 18$ for the stochastic device presented in fig. 3.4.

Fig. 3.6 shows the experimentally measured effect of changing this stability factor of an LBNM by changing temperature. Please note that a different device is used for the measurement results shown in fig. 3.6, with an LBMN whose volume is about

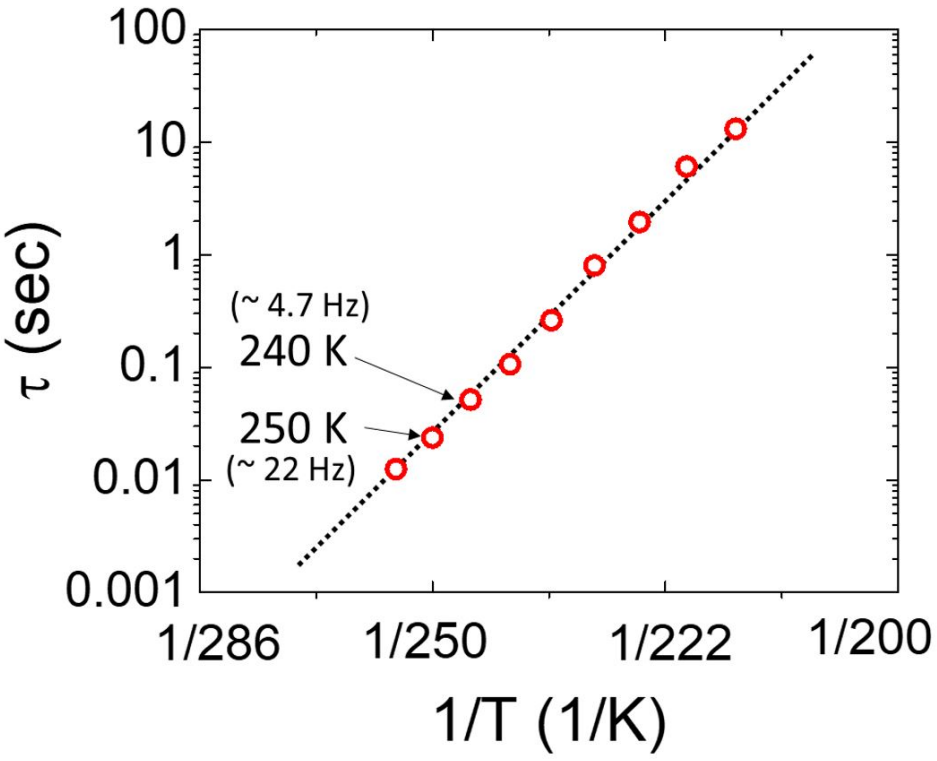

Fig. 3.6. Speed of random number generation can be changed by changing the thermal stability factor E_B/k_BT. To show this, we measure the telegraphic output at different temperatures. This plot shows the Arrhenius plot of the fluctuation time scale, τ of the magnet as a function of temperature. The time scale can be changed by more than 3 orders of magnitude by changing the temperature by 50 K.

half of the volume of that presented in fig. 3.4. As can be seen in fig. 3.6, the fluctuation time scale, τ changes by more than 3 orders of magnitude by changing the temperature. This stability factor can be reduced in practice by scaling the volume of the nanomagnet further to increase the speed of random number generation.

3.2.2 Evaluation of quality of randomness

In this section, we evaluate the quality of the random bits generated from our device using the statistical test suite provided by National Institue of Standards and Technology (NIST) [62]. Various aspects of the generated random sequence are

(a)

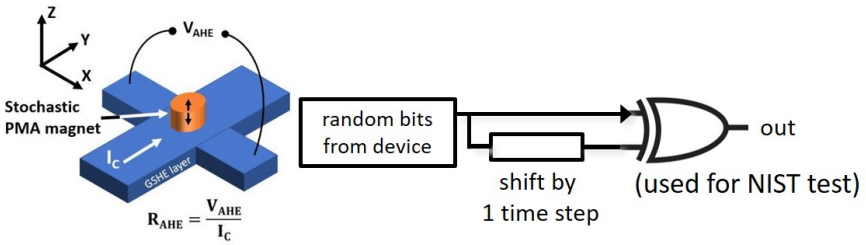

(b)

NIST STS randomness quality test results		
Test Name	**Description**	**p-value**
Frequency	Total number of 0's and 1's mismatch	0.3764
Block frequency	Number of 0's and 1's mismatch within a subset	0.6526
Runs	Too many sequences of consecutive bits of one type	0.9693
Longest run	Too many consecutive bits of one type	0.6600
Binary matrix rank	Linear dependence among fixed length substrings	0.4613
Discrete Fourier transform	Periodicity in bit stream	0.9884
Serial	Multiple low entropy sequences in a row	0.0344, 0.5958
Approximate Entropy	Bit sequence too unlikely	0.0601
Cumulative Sums (forward)	Running sum deviates too far from half the length	0.2143
Cumulative Sums (backward)	Same as previous, but in reverse direction	0.6776

Fig. 3.7. **Quality of randomness:** (a) Processing of the generated bit stream prior to performing the NIST randomness tests (b) Resutls of the NIST STS test (p-value >0.01 signifies that a test has been passed). All tests that were allowed by the limited size of the data set (10,1000 bits) were passed.

tested for qualifying as cryptographic quality random numbers. These tests compute the statistics of the input sequence such as mean value, standard deviation, entropy, repeated structures, linear dependencies, autocorrelation, etc. and compares them against theoretical expectations from a perfectly random sequence.

Prior to performing the tests, we do some pre-processing of the collected data in order to reduce any bias present. After digitizing the data, we take the XOR of the bit stream with a shifted version of itself, as shown in fig. 3.7 (a). The resulting p-values of the NIST test are given in fig. 3.7 (b). A p-value >0.01 means the test

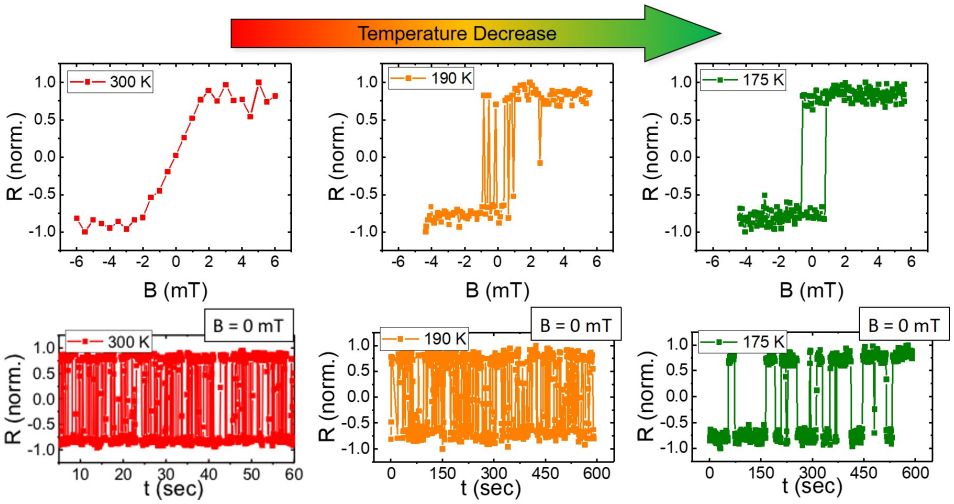

Fig. 3.8. **Field tunability and blocking:** Average anomalous Hall resistance ($\langle R_{AHE} \rangle$) as a function of out-of-plane magnetic field at different temperatures. As temperature decreases, the magnetization flipping slows down progressively towards a stable ferromagnetic behavior.

has been passed. The generated bit stream by our device passed all the 9 tests that were performed. Some of the tests required $> 10^6$ bits and were not performed due to the limited size of our data set (10,000 bits).

3.2.3 Tunability with magnetic field

Next, we demonstrate the modulation of the mean value of the RTN by using an out-of-plane magnetic field (B) that creates an asymmetry in the energy of the two stable states. The average $\langle R_{AHE} \rangle$ vs. B produces a sigmoidal curve, as shown in fig. 3.8. Here, 1 s averaging was performed during the voltage reading. To ensure that the sigmoidal curve is indeed due to averaging of a RTN signal from the PMA, we performed a temperature study. At 190 K, the average dwell time of the magnet is comparable to the averaging time of the measurement. Hence, its RTN signal gets progressively pinned to one of the stable states as the magnitude of the external field

is increased. At 175 K, the average dwell time increases further and the magnetization shows a hysteretic ferromagnetic behavior.

3.3 Stochasticity by hard-axis initialization of a perpendicular anisotropy magnet

In this section, a novel method to generate random numbers, achieved by the hard-axis initialization of a perpendicular magnetic anisotropy (PMA) magnet, is demonstrated. Supported by the Fokker–Planck theory and sLLG simulations, its pinning field and speed are discussed. Based on this, stochastic devices with electrical inputs and outputs are fabricated to implement a hardware Bayesian network building block.

A thermally stable PMA magnet whose easy axis is along the z-axis is considered. It is initialized along its hard axis direction (xy plane) by means of an external force. When the external force is removed, the magnet makes a stochastic choice to fall into one of the two stable states along its easy axis. When this is done in the presence of a small external z-directed magnetic field, the magnetization prefers one state over the other, producing the sigmoidal curve for the average magnetization. This is depicted in fig. 3.9.

To test this idea, tantalum Hall bar devices with a PMA magnet island at the center are fabricated from a stack of Ta(10)/CoFeB(1)/MgO(1.5)/Ta(5) (thicknesses in nanometers) by successive lithography and ion milling steps, as shown in the AFM image of Fig. 3 (a). A charge current in the “y”- direction produces a voltage along the “x”-direction due to the anomalous Hall effect (AHE) of the PMA magnet, where the sign of this voltage depends on whether the magnet is pointing up (+z-direction) or down (–z-direction). We use this method to read the magnetization direction of the PMA magnet. fig. 3.10 (b) shows the measured hysteresis loop of the PMA magnet by means of AHE with an external field sweeping in the “z”-direction.

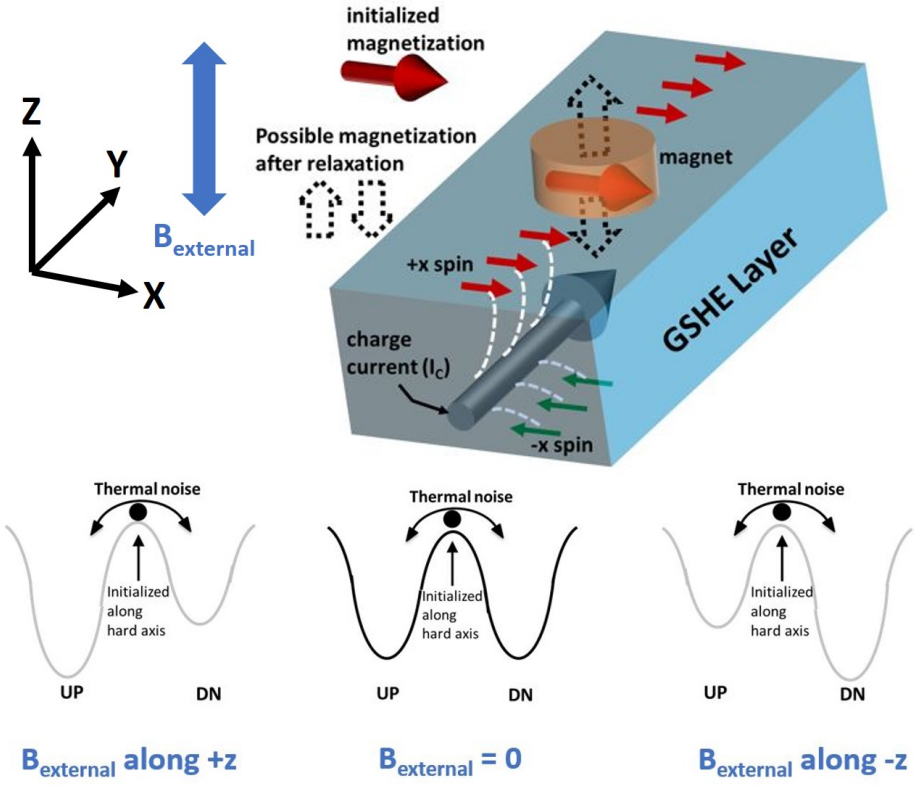

Fig. 3.9. **Hard axis initialization (concept):** When the spin current density is large enough, the magnetization of a perpendicular magnet gets pinned in the direction of the spin polarization, i.e. the magnets hard axis. Once the spin current is removed, the magnetization can become either "up" or "down" with equal probability [4] due to the symmetric energy landscape for these two states.

Next, an efficient way to put a PMA magnet in its hard axis and releasing it is demonstrated in the following experiment. It is well understood that a moderate current pulse along the y-axis of Ta can produce a spin transfer torque to the PMA magnet along the x-axis and cause its magnetization rotation in the yz plane [63]. However, when a large current pulse ($J = 3.1 \times 10^7 A/cm^2$) is applied through the Hall bar, the spin torque becomes so large that the PMA magnet can develop a magnetization along the x-direction, as predicted by Liu [63]. Once the large torque is released, the PMA magnet will go back to one of its easy axis magnetizations by random choices [see fig. 3.10 (c)], which can be monitored by the R_{AHE} reading.

This pulsing is repeated several times to show the complete randomness of the two RAHE states after each pulse. A similar experiment was performed by Bhowmik et al. [64] for spin Hall clocking of nanomagnetic logic. Furthermore, a small out-of-plane magnetic field is applied and the above-mentioned, procedure is repeated. The plot of the average magnetization after 51 pulsing events for each applied magnetic field is shown in fig. 3.10 (d). Here, the average magnetization is calculated by

$$\langle R_{AHE} \rangle = \frac{1}{N} \Sigma \left(\frac{R_{AHE}}{|R_{AHE}|} \right) \tag{3.7}$$

where N is the number of pulsing events (51 in this case). The subplots of fig. 3.10 (d) show the individual pulsing events for each point on the sigmoidal curve. This shows that at any given magnetic field B, the magnetization of the PMA magnet after releasing from its hard axis behaves stochastically, with an overall mean that is tunable by the magnetic field.

Next, the observed experimental hard-axis initialization of PMA magnets is systematically analyzed using stochastic LLG simulations. In the absence of any magnetic fields the critical current to place a PMA magnet in its hard axis is of the order of $I_{SC} = \frac{2q}{\hbar} M_S Vol. \frac{H_K}{2}$ [65]. We apply repeated current pulses of this magnitude to obtain the average magnetization in the presence of thermal noise and a z-directed external magnetic field that is on the entire time (see fig. 3.11 inset). Three different spin-current pulses are investigated based on how fast they are turned off. In the case of the fast turn off, the magnetization dynamics can be directly solved by a one dimensional Fokker–Planck equation (FPE) [66] that describes the exact evolution of the ensemble, since when the spin current is off, the external magnetic field and the anisotropy are both in the ±z direction. The FPE equation for a z-directed PMA magnet is described by:

$$\frac{\partial p(m_Z, \tau_N)}{\partial \tau_N} = \frac{\partial}{\partial m_Z} \left[(i - h - m_Z)(1 - m_Z^2) p + \frac{1 - m_Z^2}{2E_B} \frac{\partial p}{\partial m_Z} \right] \tag{3.8}$$

Here, i is the normalized z-polarized spin current I_S/I_{SC} where $I_{SC} = 4q/\hbar\alpha E_B(k_B T)$ with α being the damping coefficient and E_B being the thermal energy barrier of the

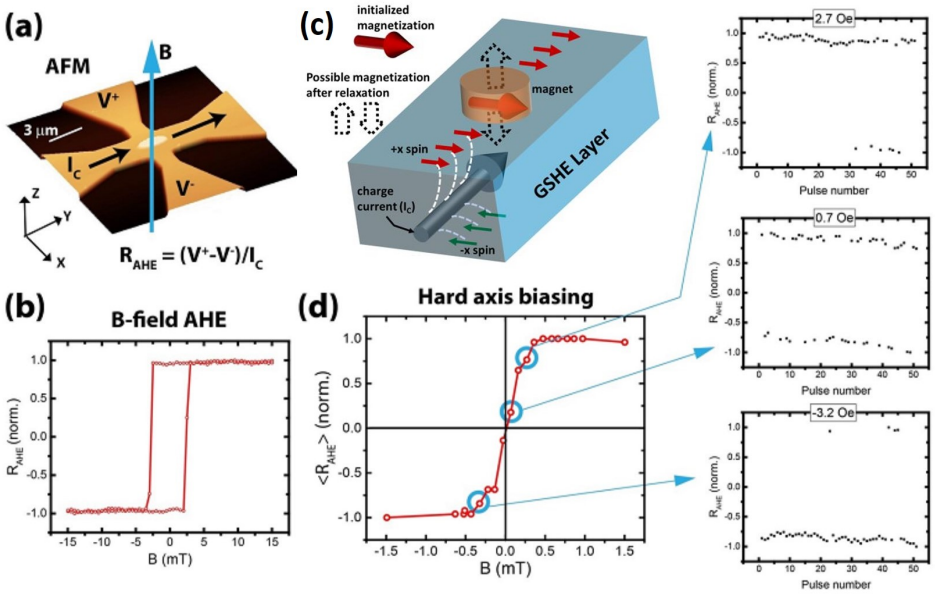

Fig. 3.10. **Hard axis initialization (experiment):** Tunable random number generator from hard-axis initialization of a PMA magnet. (a) AFM of the fabricated device with marked current, voltage, and external magnetic field directions. The AHE resistance is calculated by taking the ratio of the voltage developed and the charge current supplied. (b) R_{AHE} as a function of external B field. The hysteretic behavior is indicative of a good, stable PMA magnetic behavior. (c) Cartoon depicting the physical picture of hard-axis initialization. (d) Sigmoid obtained by putting the PMA magnet in hard axis by GHSE torque and then letting it relax back to either "up" or "down" position in the presence of a small external field along the z-axis. Each point in this curve is obtained by taking the average of 51 GSHE pulsing events. Three indicative points are shown in the three panels to the right-hand side of the graph.

magnet; h is the normalized z-directed external magnetic field H_{ext}/H_K; τ_N is a normalized time which is related to the real time t by $t = \tau_N(1+\alpha^2)/\alpha\gamma H_K$. After the x-polarized GSHE spin current is turned off, $i = 0$ in the FPE equation.

The FPE is solved starting from the time when the pulse is turned off, with an initial condition $p(m_Z, \tau_N = 0)$ that places the initial probability distribution to the

hard axis, approximated by a Gaussian distribution of $p(m_Z)$ with mean zero and a very small standard deviation. For a fast turn off of the spin current, FPE is in good agreement with a direct stochastic LLG simulation. This suggests that the slope of the sigmoid depends only on the energy barrier (E_B) and the ratio of the external magnetic field to the anisotropy field (H/H_K), since these are the only parameters that enter the FPE. So, for a given energy barrier, having a lower H_K results in a smaller pinning field, as evident from the x-axis of fig. 3.11.

The speed at which random numbers can be generated by the hard axis initialization method is ultimately limited by the time it takes for the magnetization to relax back to one of the stable states once released from the hard axis. This is determined by the natural time scale (τ_N) of the magnet mentioned earlier, and is independent of its energy barrier, unlike the case of low barrier magnets. Second, since the randomization occurs when the magnet relaxes from its hard axis and is not affected by any prior events, the pulse rise time trise and the pulse width t_{ON} does not affect the process if their sum is larger than τ_N . However, the pulse fall time (t_{fall}) affects the process of magnetization relaxation from the hard axis. We observed that for slow current the ramp down the sigmoidal curve becomes sharper. The inset of fig. 3.11 illustrates this behavior for ten samples for different spin-current pulses at a slightly negative magnetic field.

Second, this method provides a potentially better alternate to the STT-MTJ-based true random number generators (TRNGs) [67]. In our case, the current pulse passes through the adjacent heavy metal layer (Ta) instead of passing through the tunnel barrier as in the case of STT-MTJ-based TRNGs, and hence, our device has potentially better endurance and capability of producing more random numbers. Also, compared to TRNGs based on superparamagnetic MTJs [54], this device does not require an external magnetic field to cancel the dipolar field from the reference layer.

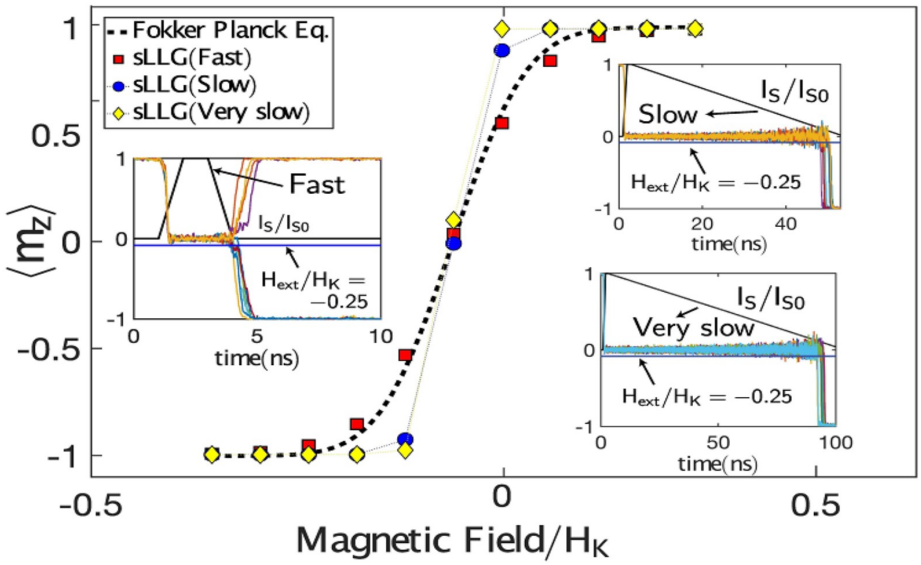

Fig. 3.11. **Hard axis initialization (theory):** Stochastic LLG simulations of a hard-axis initialized PMA magnet. At each point, at least N = 200 samples are recorded, and an average magnetization is obtained as in the experiment.

Acknowledgment

This work was supported in part by the Center for Probabilistic Spin Logic for Low-Energy Boolean and Non-Boolean Computing, in part by one of the Nanoelectronic Computing Research Centers as task 2759.003 and 2759.004, and in part by a Semiconductor Research Corporation program sponsored by the National Science Foundation through CCF 1739635. A part of this work was also supported by the Nanoelectronics Research Corporation (NERC), a wholly-owned subsidiary of the Semiconductor Research Corporation (SRC), through the Institute for Nanoelectronics Discovery and Exploration (INDEX).

4. BAYESIAN NETWORK BUILDING BLOCK IMPLEMENTATION WITH HARD AXIS INITIALIZED PERPENDICULAR NANOMAGNETS

Most of the materials in this chapter have been extracted verbatim from the paper: Debashis, Punyashloka, et al. "Design of Stochastic Nanomagnets for Probabilistic Spin Logic." IEEE Magnetics Letters 9 (2018): 1-5; and Debashis, Punyashloka, et al. "Hardware implementation of Bayesian network building blocks with stochastic spintronic devices.", under review (2020)

4.1 Introduction

Bayesian networks (BNs) are directed graphical models that are used to represent the causal dependencies among stochastic variables [68]. In a BN, each node represents a stochastic variable, whose probability of occurrence is determined by the states of its parent nodes. The dependence between a set of such nodes is given by a conditional probability table (CPT). BNs are traditionally implemented in software aiming at applications in areas such as forecasting, diagnosis, and computer vision [6]. However, as the complexity of the BNs grows, i.e., as the number of parent nodes affecting the probability of a particular child node becomes large, both the assessment of that child node probability, and the inference about the possible cause becomes impractical [69]. Specifically, as the network size grows, the number of terms in the calculation of the joint probability using probability chain rule increases rapidly [69].

Direct representation of Bayesian networks in hardware has been proposed as an alternative way to perform the two above mentioned tasks, i.e., probability assessment and inference. In this case, each "node" in a Bayesian network is represented by a stochastic device, having a distinct probability of being in one of two possible states.

This probability is controlled by the input it receives dependent on the states of its parent nodes, through the weights of the connections between them. The CPT is encoded in the weights of these connections. By representing a BN with a hardware network of this kind, the required probability of a particular event is readily obtained by sampling the output of the corresponding stochastic device. Moreover, inference about the possible cause of a particular event can be evaluated by observing the joint distribution of the two stochastic devices corresponding to the "event" node and the particular "cause" node of interest.

Several hardware implementations of BNs have been proposed based on CMOS hardware. For example, Zermani et al. [70] demonstrated FPGA based BN implementation utilizing suitable architectural design and memory allocation schemes. Cai et al. [71] demonstrated another FPGA based architectural design along with a suitable pseudo random number generator. Manisinghka et al. [72] implemented a BN in digital circuits using a novel abstraction. Chakrapani et al. [73] and Weijia et al. [74] proposed a probabilistic CMOS hardware for BN implementation, however there has not been an experimental demonstration in literature to our knowledge. Nevertheless, there is an interest in a compact implementation of the stochastic nodes of a BN and their conditional relations.

In this work, we present an experimental demonstration of a spintronics based compact hardware implementation of BNs. The stochastic elements are implemented naturally by a compact device consisting of a perpendicular nanomagnet. The CPTs are translated directly to the connection weights, implemented by resistive connections between such devices.

Unstable nanomagnet based spintronic devices have recently attracted much research interest for probabilistic spin logic (PSL) [30, 35, 38, 39, 51, 57, 75–81] and are given the name "p-bit", which is the short form of "probabilistic bit". It has been proposed that inherently unstable nanomagnet can be a natural implementation of the stochastic variable in a BN [35, 75, 76, 82]. We first present a p-bit implementation using a stochastic spintronic device that has isolated input and output to allow for

interconnection in circuitry. The output of such a device is a tunable random number, whose mean is controlled by an electrical input. Then, we build an electrically connected network of two such devices and study the correlation of their outputs for different connections and biases. We show that any CPT can be implemented by changing the connections and biases of this circuit, thus representing a hardware BN building block. Finally, using parameters taken from the experiment, we perform a stochastic Landau Lifshitz Gilbert (sLLG) simulation of a four node BN and compare the results of the forecast with those expected from calculating joint probability distributions.

4.2 Hard axis initialized PMA magnet as p-bit

In our experiment, the stochastic device is based on a hard axis initialized magnet with perpendicular magnetic anisotropy (PMA), whose output probability is controlled by the magnetic field produced by a charge current passing through an isolated metal ring [78, 79, 81]. The top left of fig. 4.1 (a) shows the schematic of our device. It consists of a nanomagnet island with perpendicular magnetic anisotropy (PMA) shown in orange, on top of a heavy metal (Ta) Hall bar, shown in blue. It is well understood that the magnetization of a PMA magnet can be deterministically switched by the Spin Obit Torque (SOT) of a heavy metal under-layer in the presence of a symmetry breaking in-plane magnetic field [28, 83]. However, when the spin current density is large enough, and when this field is absent, the magnetization gets pinned in the direction of the spin polarization, i.e. the magnets hard axis. Once the spin current is removed, ambient thermal noise makes the magnetization relax to either "up" or "down" with equal probability due to the symmetric energy landscape for these two states [64, 78, 79] as depicted by the cartoon in the top right of fig. 4.1 (a).

The magnetization state is read out by the anomalous Hall effect (AHE), where the transverse V_{OUT} is +ve for a magnetization in the "up" direction and -ve for "down". The probability of relaxing back to the "up" or "down" direction can be

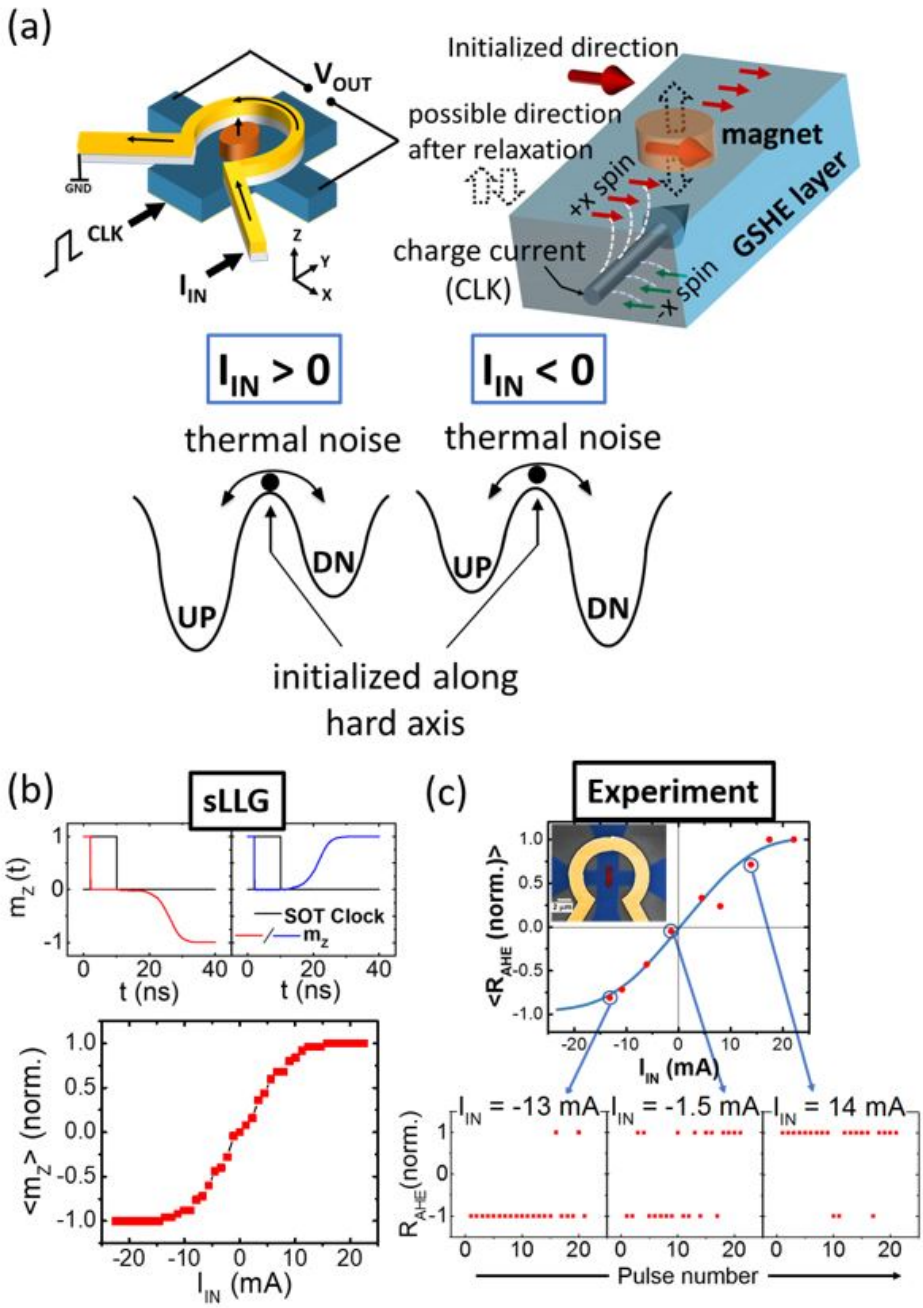

Fig. 4.1. (a) Schematic of the probabilistic device and illustration of the hard axis initialization by spin orbit torque. (b) Stochastic LLG simulation of 500 ensembles, showing tunable random behavior of the device. The two top panels show representative cases where the magnetization relaxes to the "UP" and "DN" direction after being released from the hard axis. (c) Experimental measurements on the device showing stochastic behavior with tunability using a charge current through an isolated Oersted ring. The bottom panels show the stochastic outputs, whose averages show the sigmoidal behavior as a function of the input current.

controlled by applying a small out-of-plane magnetic field that lifts the degeneracy of the energy landscape. A positive field in the z-direction lowers the energy of the "up" state and raises that of the "down" state, thus making the "up" state more favorable. A negative z-directed field does the exact opposite. This is depicted in the energy landscape diagrams shown in the bottom panel of fig. 4.1 (a). This z-directed field is provided by a ring-shaped electrode called the "Oersted ring" henceforth, shown in yellow in the device schematic. A current "I_{IN}" passing through the Oersted ring of radius "r" produces a magnetic field given by $B = \mu_0 \times \frac{I_{IN}}{2r}$. fig. 4.1 (b) shows the sLLG simulation of such a device. The top panels show the magnetization dynamics during the pulsing of the device. The current pulse through the GSHE layer is shown in black color in both the panels. The z-component of magnetization (m_Z) is shown in blue and red. It can be seen that m_Z goes to zero while the current pulse is ON. After the pulse is removed, m_Z relaxes to -1 in the first case and it relaxes to +1 in the second, nominally identical case, highlighting the stochastic nature of the process. The time scale of this relaxation is governed by the material parameters of the nanomagnet such as M_S, H_K and damping. The bottom panel of fig. 4.1 (b) shows the average of the magnetization (after the dynamics have settled) in the z-direction (perpendicular easy axis) as a function of the input current, resembling a sigmoidal activation function.

For experimental implementation, starting the following stack of Ta(5nm)/CoFeB(1nm)/MgO(2nm)/Ta(1nm) thin film, a Hall bar device with a PMA magnetic island located at the center is fabricated by means of successive e-beam lithography and Ar ion milling steps. To generate the out-of-plane field for tunability, the "Oersted ring" is fabricated on top and electrically isolated from the Hall bar by a dielectric layer. A false colored SEM image of the fabricated device is shown in the inset of fig. 4.1 (c).

For the operation of the device, a Keithley 6221 current source is used to provide a current pulse of duration 100 μs through the Ta Hall bar. This current pulse experimentally implements the required hard axis biasing scheme as shown in the

sLLG simulation of fig. 4.1 (b). Although the magnet can respond to much faster pulses, as shown in fig. 4.1 (b), we chose to use 100 μs to be safely within the delay times of the measurement circuit. After the pulsing event, the state of the magnetization is read by a lock-in scheme, with a sinusoidal current provided by the same Keithley current source and an SRS830 lock-in amplifier. The device is pulsed repeatedly, and the state of the magnetization is read after each individual pulse. fig. 4.1 (c) shows the average magnetization as a function of the input current "I_{IN}". Each data point is obtained by averaging 25 pulsing events, as shown for three representative cases in the bottom panels. These measurements clearly demonstrate the successful implementation of a device with an electrical input and output, which behaves stochastically for individual events, but produces a sigmoidal curve for the average output. This is the desired characteristic for many probabilistic spin logic applications including hardware BNs.

4.3 Implementing a two node Bayesian network in hardware

Next, we show how the stochastic devices described in the previous section can be used to implement a two node Bayesian network in hardware. The essential characteristic of a BN is captured in the CPT. Fig. 4.2 (a) shows the example of a two-node network, with the first or the parent node (m_1) representing the packaging material for blocks of cheese in a dairy farm, and the second node (m_2) representing the probability of finding a stale cheese block. The values "a" and "b" in the CPT represent the probability of a cheese block being stale if the packaging material is of low quality ($m_1 = 0$) vs. high quality ($m_1 = 1$). Since the packaging material positively affects the shelf life, in this case, a > b. If instead of packaging material, m_1 represents the print design on the package, then the shelf life is not affected by it, and hence, a=b in this case. Similarly, if some other variable, that negatively affects the shelf life is represented by m_1, then the CPT would have a < b. Now, for the first case, if the cheese was stored in a cold and dry storage, then the shelf life is increased, irrespec-

tive of the packaging material quality. This corresponds to adding a positive value to both a and b in the CPT. Hence, the variables in the CPT can span the entire space between 0 and 1 independently, depending on the problem being modeled.

We first demonstrate that the CPT between the two probabilistic random variables in our example can be implemented by design of proper electrical connections between two of our stochastic devices (of the type shown in fig. 4.1). Then, by testing the circuit with designed parameters, we show that the probability of the output device (m_2) follows the probability of finding a stale cheese block, obtained from calculating the joint probability distribution. We also show that the inference about the potential cause of stale cheese that is evaluated by Bayes theorem is well matched to the directly observed values from the joint distribution of the device outputs. The results are also verified by stochastic LLG simulations with magnet parameters (M_S, H_K and volume) taken to match the sigmoidal activation function obtained from the experiment. Fig. 4.2 (a) shows the given CPT that represents the relation between the stochastic variables m_1 and m_2. This CPT is translated into the parameters J_{21} and h_2 of the PSL model as shown in fig. 4.2 (b). This translation can be obtained from the analysis below: The total input, I_2, received by the second device is given by:

$$I_2 = J_{21} \times m_1 + h_2 \tag{4.1}$$

where J_{21} corresponds to the connection from the first to the second device, m_1 corresponds to the state of the first device and h_2 corresponds to the constant bias given to the second device. As eq. 4.1 represents the physical input to node 2 (which is current in our hardware design), m_1 has to enter as a bipolar value (+1 for 'UP' state and -1 for 'DN' state). The average state of the second device is given by:

$$< m_2 >= \sigma(I_2) = \sigma(J_{21} \times m_1 + h_2) \tag{4.2}$$

where σ represents the sigmoidal activation function for device 2. The conditional dependencies can be directly seen from this expression. The probability of m_2 being

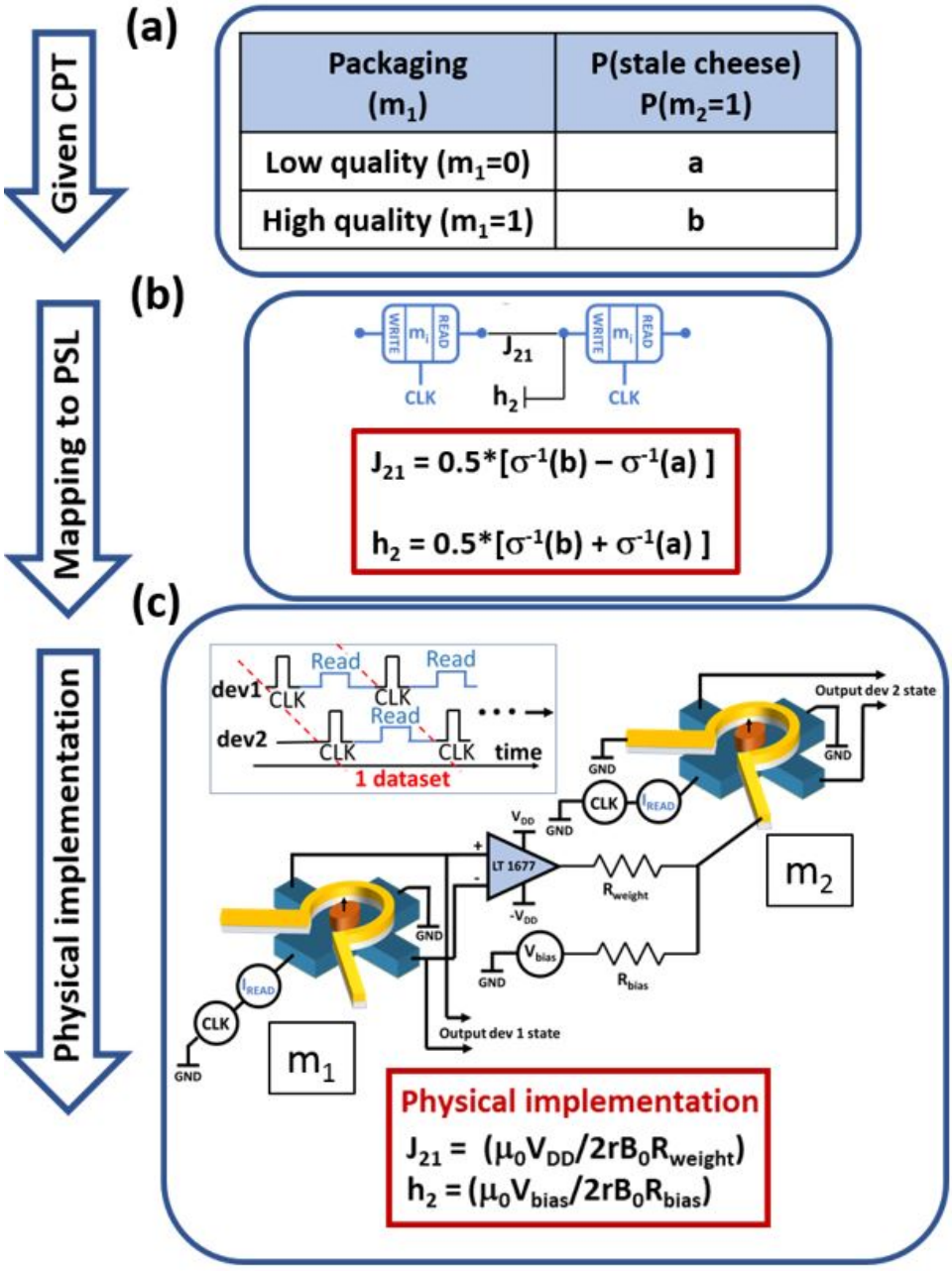

Fig. 4.2. Hardware design of a two-node network. (a) The given conditional probability table (CPT) representing the causal dependency of two probabilistic variables, i.e., the quality of packaging and state of cheese (b) PSL model of the two node BN with the CPT parameters translated to PSL parameters (c) Circuit schematic of two connected devices to implement two coupled Bayesian nodes. Inset on the top left shows the timing diagram of various operations performed on device 1 and 2.

high given m_1 high is obtained by evaluating $< m_2 >$ from eq. 4.2 by setting $m_1 = 1$. Since this probability should match the value specified in the given CPT, we obtain:

$$b = \sigma(J_{21} + h_2) \tag{4.3}$$

Similarly, 'a' can be obtained by setting m_1 = -1 (as bipolar entry corresponding to m_1 being 'DN' is -1 instead of 0) in eq. 4.2

$$a = \sigma(-J_{21} + h_2) \tag{4.4}$$

From eq. 4.3 and 4.4 , we obtain the values of the PSL parameters J_{21} and h_2, from the given CPT table as follows:

$$J_{21} = 0.5 \times \left[\sigma^{-1}(b) - \sigma^{-1}(a)\right] \tag{4.5}$$

$$h_2 = 0.5 \times \left[\sigma^{-1}(b) + \sigma^{-1}(a)\right] \tag{4.6}$$

The parameters J_{21} and h_2 are then used to design the hardware connection strengths and biases to two stochastic devices, as will be discussed in the following paragraphs.

Fig. 4.2 (c) shows the schematic of our circuit. The output voltage from the first device is amplified by a LT1677 low noise, rail-to-rail precision Op Amp operating in an open loop configuration. The output level of the Op Amp is determined by its $\pm V_{DD}$ supply voltages. This output is then connected to the Oersted ring of the second device through a weight resistor "R_{weight}" that determines how much current passes through it, and hence controls the output probability of the second device, corresponding to the J_{21} term in a BN. Additionally, a voltage source "V_{bias}" is connected to the input of the second device through a resistor "R_{bias}" to mimic the fixed bias (h_2) in a BN. The values of the circuit parameters V_{DD}, V_{bias}, R_{weight} and R_{bias} are obtained from the required J_{21} and h_2 by the following design analysis:

In our circuit as shown in fig. 4.2 (c), J_{21} is the magnetic field produced by the Oersted ring of device 2, normalized with the field required to saturate its magnetization in the UP or DN state, denoted by B_0. This is given by:

$$J_{21} = \pm \left(\frac{\mu_0}{2rB_0}\right)\left(\frac{V_{DD}}{R_{weight}}\right) \tag{4.7}$$

where r is the radius of the Oersted ring, μ_0 is the permeability of vacuum and the $\pm$ sign depends on the connection polarity. Similarly, h_2 is the additional magnetic field produced by the constant bias V_{bias}, normalized to B_0.

$$h_2 = \left(\frac{\mu_0}{2rB_0}\right)\left(\frac{V_{bias}}{R_{bias}}\right) \tag{4.8}$$

Note that h_2 contributions due to the remnant magnetic field in the measurement setup have been subtracted out in this analysis for brevity. This additional h_2 contribution is just added to the calculated h_2 in eq. 4.8.

Next, we show that the same circuit can capture any given CPT, by changing the R_{weight} and R_{bias}. In the circuit shown in fig. 4.2 (c), the total input received by device 2 is given by:

$$I_2 = \pm \left(\frac{\mu_0}{2rB_0}\right)\left(\frac{V_{DD}}{R_{weight}}\right) \times m_1 + \left(\frac{\mu_0}{2rB_0}\right)\left(\frac{V_{bias}}{R_{bias}}\right) \tag{4.9}$$

For $R_{weight} = \infty$, which means $J_{21} = 0$, the coefficient of m_1 in eq. 4.9 vanishes, and so does the correlation between the two devices. For a finite R_{weight}, the connection polarity dictates the sign of the correlation between the two devices, with a strength inversely proportional to R_{weight}. V_{bias} makes the correlation asymmetric as its corresponding term in eq. 4.9 does not change sign with the state of m_1. Therefore, we can span all possible conditional probabilities between two nodes of a BN (given by a and b in the CPT) by changing the circuit parameters R_{weight}, polarity and R_{bias}.

4.4 Experimental testing of the hardware Bayesian network

We take five different CPTs with a and b spanning the range between 0 and 1, shown in fig. 4.3 (a). We then calculate J_{21} and h_2 for these five cases and design

our circuit according to eq. 4.7 and. 4.8. The designed circuits are then tested by repeating a sequential pulsing scheme. The inset of fig. 4.2 (c) shows the timing diagram of the measurement procedure. The two devices are pulsed sequentially by a Keithley 6221 current source that provides the clocking scheme for our devices. During the pulsing of the second device, a constant DC read current is passed through the first device in order to generate the input voltage to the second device. Then, this sequential pulsing is repeated to generate the required statistics. The two devices produce random outputs, but with correlated statistics, as is required by the CPT between the two random variables. The output after each pulse is measured by a lock-in amplifier and then digitized. Representative sections of the device outputs are shown in fig. 4.3 (b) for three different connection configuration. It is worth noting that the pulsing method being followed in the presented experiments (shown in the inset of fig. 4.2 (c)) is analogous to Gibbs sampling [36, 37], which is widely used is used for statistical inference [84, 85]. Here, each node of the network is pulsed (sampled) sequentially under the influence of all the other nodes, which are fixed to their current values.

The probability of finding a stale cheese block can be found from the joint probability distribution by using the probability chain rule:

$$\begin{aligned} p(m_2 = 1) &= \textstyle\sum_{m_1} p(m_1, m_2 = 1) \\ &= \textstyle\sum_{m_1} p(m_2 = 1|m_1) \times p(m_1) \\ = p(m_2 = 1|m_1 = 0) \times p(m_1 = 0) &+ p(m_2 = 1|m_1 = 1) \times p(m_1 = 1) \\ &= a \times p(m_1 = 0) + b \times p(m_1 = 1) \end{aligned} \tag{4.10}$$

where p($m_1 = 0$ or 1) is an input parameter. The number of terms in the above expression grows as 2N where N is the number of parent nodes for the particular child node of interest [69]. Instead of performing this algebra, the required probability can be obtained from the circuit by directly observing the stochastic output of device 2 and obtaining its mean value over several pulsing cycles. This luxury of having to observe only the nodes of interest while disregarding all the other nodes is an advantage of

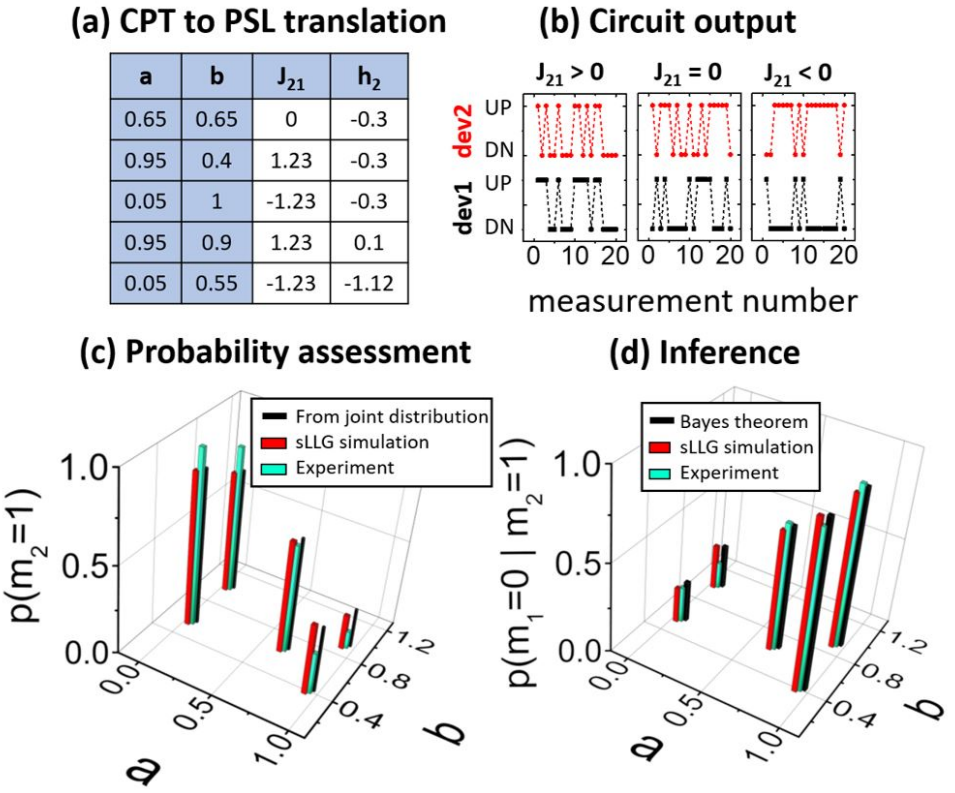

a	b	J_{21}	h_2
0.65	0.65	0	-0.3
0.95	0.4	1.23	-0.3
0.05	1	-1.23	-0.3
0.95	0.9	1.23	0.1
0.05	0.55	-1.23	-1.12

Fig. 4.3. Testing of the two node BN circuit. (a) Five different combinations of the CPT parameters that are experimentally implemented in hardware. (b) Representative sections of the measured data for positive, negative and no connection between device 1 and device 2 as shown in fig. 4.2(c). (c) Obtained output probabilities of cheese being stale for the five different given CPTs. The experimentally obtained probability values are in good agreement with theory and stochastic LLG simulations. (d) Inference about probability of the packaging being bad quality given that a stale cheese is found is plotted for the different CPTs, showing good match between direct experimental observation, Bayes theorem and stochastic LLG simulations.

using a probabilistic hardware, versus calculating the probabilities using deterministic rules as discussed by Feynman [86] and utilized in many sampling schemes [36].

Similarly, given that a randomly drawn cheese block from a large lot is stale, the probability that it was caused by a low quality packaging material can be found by using Bayes theorem:

$$\begin{aligned} p(m_1 = 0|m_2 = 1) &= p(m_1 = 0, m_2 = 1)/p(m_2 = 1) \\ &= p(m_2 = 1|m_1 = 0) \times \tfrac{p(m_1=0)}{p(m_2=1)} \\ &= \tfrac{a \times p(m_1=0)}{a \times p(m_1=0) + b \times p(m_1=1)} \end{aligned} \tag{4.11}$$

The number of terms required in the evaluation of the above expression also grows as 2N where "N" is the number of potential binary causes of a particular effect [69]. However, from the hardware BN, this probability can be directly obtained by observing the joint distribution of states of the two devices. It is to be noted here that this way of performing the inference always involves observing the joint distributions of only two nodes of the BN: nodes corresponding to the effect and the potential cause of interest, irrespective of N.

In our experiment, after 100 pulsing cycles, the obtained output probabilities for all the five circuits (representing the five different CPTs of fig. 4.3 (a)) is comparable with the expectation from calculating the joint probability distribution and is also verified by stochastic LLG simulations, as shown in fig. 4.3 (c). Similarly, the obtained probabilities from inference is comparable with that from Bayes theorem and stochastic LLG simulations, seen in fig. 4.3 (d).

4.5 Circuit Implications and Improvements

Previously proposed hardware implementations of Bayesian networks have used CMOS based pseudo random number generators realized with XOR-SHIFT circuits [72] or RAM-based Linear Feedback Gaussian Random Number Generators [70, 71] that require a large area footprint. What we have demonstrated here is a compact true random number generator (TRNG) capable of operating at few hundreds of MHz. The

speed of the device is only limited by the time required for SOT hard axis initialization and magnetization relaxation after removal of SOT, which normally requires a few nanoseconds as shown in the sLLG time plot panels of fig. 4.1 (b). Compared to previously demonstrated spin based TRNG [54, 67, 87], this implementation employs a different scheme to generate random numbers. In our approach, any applied current that is larger than that required for hard axis initialization of the magnet will result in the generation of a random number with the correct statistic once the current pulse is removed [81, 82]. Hence, in a large network, the device to device variation in the required current can be easily mitigated by choosing the largest value of the required current among all devices. Possible variations in the shape and offset of the sigmoidal activation function of our devices can be controlled by appropriately choosing the parameters B_0 and h_2 while translating the given CPTs into the connection weights, shown in eq. 4.5, 4.6, 4.7, 4.8. Also note that the Bayesian network proposed here does not require analog voltage sources or CMOS MUX to realize the CPT as proposed previously by Shim et al [82]. Using current controlled tunability of the device and auxiliary nodes, any CPT can be realized by using only p-bits, one voltage level (V_{DD}) and analog memristive elements for interconnections and individual biases similar to RRAM based neural networks. Such programmable analog memristive elements have been successfully demonstrated recently [88, 89]. The energy requirement of the device demonstrated here can be improved by using the voltage-controlled magnetism (VCM) effect for hard-axis initialization as proposed by Scott et al. [90] in their benchmarking study (section IV of the main text). In addition, employing magnetic tunnel junctions (MTJs) instead of AHE can eliminate the need for OP-AMPs for readout. The typical difference in the two stable resistive states of an MTJ is of the order of 10 K, whereas in case of AHE, it is a few ohms for standard material stacks. This allows the elimination of the OP-AMPs for readout. Implementations of an MTJ based readout scheme, where the state of the free layer magnet is converted to a voltage by a potential divider formed by the MTJ and a normal resistor was presented by Camsari et al. [30] (figure 3 of the main text) and Hassan et al. [45]

(figure 4 of the main text). In these references, the voltage swing generated at the output is large enough to be converted to a "rail-to-rail" swing by a single inverter. In the above references, the MTJ free layer was designed to be a low barrier magnet, but the analysis of the output swing remains unchanged for our hard axis initialization scheme with stable magnets.

4.6 Conclusion

We have experimentally demonstrated that by connecting two stochastic spintronic devices and designing the connection and bias parameters, BN building blocks can be implemented in hardware. By implementing BNs using such hardware, both probability assessment and inference can be performed by sampling the output of only the relevant nodes. This demonstration serves as a step towards building large scale hardware systems for implementing Bayesian networks.

Acknowledgment

I would like to gratefully acknowledge that the work related to Bayesian network was done in close collaboration with Vaibhav Ostwal. This work was supported in part by the Center for Probabilistic Spin Logic for Low-Energy Boolean and Non-Boolean Computing, in part by one of the Nanoelectronic Computing Research Centers as task 2759.003 and 2759.004, and in part by a Semiconductor Research Corporation program sponsored by the National Science Foundation through CCF 1739635.

5. CORRELATED FLUCTUATIONS IN A TWO P-BIT NETWORK

Most of the materials in this chapter have been extracted verbatim from the paper: Debashis, Punyashloka, and Zhihong Chen. "Tunable Random Number Generation Using Single Superparamagnet with Perpendicular Magnetic Anisotropy." 2018 76th Device Research Conference (DRC). IEEE, 2018, and Debashis, Punyashloka et al."Correlated fluctuations in spin orbit torque-coupled perpendicular nanomagnets", in press, Physical Review Applied (2020)

5.1 Introduction

In chapter 3, we demonstrated that by designing proper thickness of the magnetic layer, the perpendicular anisotropy can be made week in a Ta/CoFeB/MgO/Ta stack. Utilizing that, we demonstrated a device where the state of the low barrier nanomagnet (LBNM) can be read electrically via the anomalous Hall effect (AHE). We characterized the speed and the quality of the generated random numbers. However, for being useful as a p-bit, the probabilities of occurence of the output states must be tunable electrically.

Several implementations of LBNM based true random number generators have been demonstrated in the last few years, while only a few included the output tunability. One such device is based on an SMTJ with an in-plane LBNM as the free layer, where the tunability of the output state is obtained through spin transfer torque (STT) [54]. It is well known that the major reliability issue in STT-MRAM is the result of the read and write operations sharing the same access path through the entire MTJ stack. Furthermore, having a common read and write path does not allow for the isolation of the input and output signals, and hence makes it difficult

to concatenate these devices into a network. Therefore, a three-terminal device with SOT based output tunability is much more desirable due to the separation of the write current path from the read current path [91]. Such devices have been proposed for in-plane LBNMs [51, 78, 92]. However, recent simulation studies suggest that a dense array of in-plane LBNMs have significant magnetic dipolar interactions [54]. Such interactions could lead to compromised randomness and unwanted correlations between SMTJs in a large network. Moreover, SOT tunability of in-plane magnetization occurs through the so-called anti-damping mechanism, which is energy inefficient since it must overcome a large demagnetization field [28]. Therefore, LBNMs with perpendicular magnetic anisotropy (PMA) are ideal for high density, smaller pitch size arrays that are essential for large network implementations. However, current material systems that exhibit SOT can only generate spins with in-plane polarization, which is orthogonal to the magnetization of the low barrier PMA magnet, hence, complete tunability of its output state is not possible through SOT alone [79]. In case of stable PMA magnets, in-plane polarized spin currents can switch the magnetization deterministically between "UP" to "DN" state in the presence of a small symmetry breaking in-plane magnetic field, as first shown by Miron et al. [83] and Liu et al. [63]. Later, several approaches were demonstrated to remove the requirement of this undesirable external field by introducing a built-in symmetry breaking field. This is achieved by means of either a tilted anisotropy [93], lateral structural anisotropy [94], interlayer exchange coupling [95, 96], GSHE of an antiferromagnet [97, 98] and ferroelectric substrate [99,100]. These approaches could potentially be adopted to tune the stochastic output of a PMA LBNM. However, experimental demonstration of such a SOT tunable LBNM based device is not present in literature to the best of our knowledge.

In this work, we demonstrate for the first time, an SOT tunable random number generator made of a PMA LBNM. The SOT tunability is realized through a small tilt in the magnetic anisotropy axis, as is evidenced by our experiments and supported by sLLG simulations. We then couple two such devices via electrical connections and

study the correlation in their output fluctuations. Our experiments show that a weak coupling strength, that is 10 times smaller than the critical current required for deterministic switching, is sufficient to establish correlations between the outputs of the two devices. By changing the connection polarity, we show that the correlation can be changed from positive to negative. Our studies also show that two LBNMs with different time scales of fluctuation can get correlated efficiently. We perform simulations (not part of this thesis) on this coupled 2 p-bit system using a dynamical model of autonomous circuits with all the required parameters taken from experiments. The simulation results show good matching with the experiments. This demonstration of a novel tunable TRNG and its behavior in an electrically coupled network provides important insights towards realizing large p-bit networks for unconventional computing tasks.

5.2 Tunability with spin orbit torque

We demonstrate that the mean value of the random numbers can also be tuned by a DC current through the giant spin Hall effect (GSHE) Ta Hall bar, as shown in fig. 5.1. Fig. 5.1 (a) shows the measurement configuration, where a constant DC current (I_{DC}) through the GSHE underlayer is applied on top of a small AC read current (I_C). As shown in fig. 5.1 (d), depending on the sign and magnitude of I_{DC}, the magnetization direction favors the "UP" or "DN" direction, resulting in the sigmoidal curve for the average. We call this device a probabilistic bit, i.e. a p-bit. Representative signals at three different I_{DC} are presented in the panels to the right of fig. 5.1 (d). The effect of DC current can also be seen by plotting the dwell time in "UP" and "DN" states for various I_{DC}, as shown in fig. 5.1 (e) (measurement done at 250 K). This modification in the dwell time directly results in the tunability of the average magnetization. It is worth mentioning here that the small read current can also affect the state of the output, especially for a LBNM having a thermal barrier close to zero, and hence has to be carefully mitigated by design. This read disturb

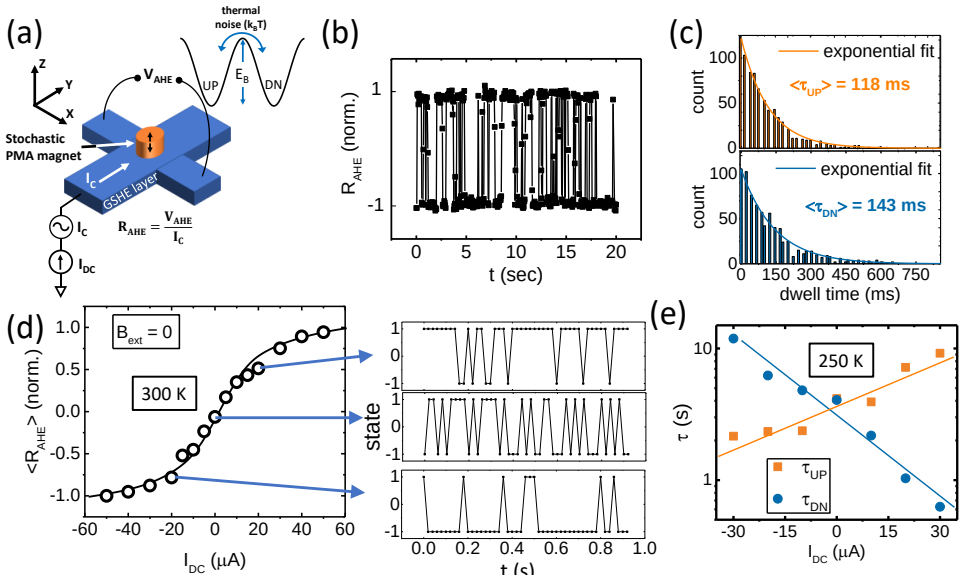

Fig. 5.1. (a) Schematic of the measurement configuration with the fabricated device. The magnetic island has a diameter of 100 nm. Cartoon representing the energy diagram of the perpendicular magnetization is shown in the top right inset. The two states, i.e, "UP" and "DN" are separated by a small energy barrier E_B, so that thermal energy is sufficient to randomly fluctuate the magnetization between the two states. (b) Measured anomalous hall resistance for a fixed small read current (I_C) and no DC current (I_{DC}). The random telegraphic signals arise from the random fluctuations of the perpendicular magnetization between UP and DN states. (c) Histogram of the dwell time in UP and DN states. Both histograms are well fitted by an exponential envelope, showing that the magnetization flipping can be represented by a random Poisson process. The average dwell time (τ_{UP} and τ_{DN}) are calculated from the exponential fit. (d) Measurement with a DC charge current through the GSHE underlayer to obtain tunability. A sigmoidal curve is obtained for the average R_{AHE} vs. I_{DC}, showing tunability for a PMA LBNM without any external magnetic field. Each point on this curve is obtained by averaging the random telegraphic output, representative data sets shown in the three panels on the right. (e) The dwell times in UP and DN state changes as a function of I_{DC}, which leads to the sigmoidal curve for average magnetization state.

issue however is negligible in our case, where the energy barrier of the LBNM is $\approx$18 k_BT. Please note that the steeper dependence of τ_{UP} compared to τ_{DN} is just an

experimental artifact, that could be the result of a small X-directed remnant magnetic field in the measurement chamber, which results in different tilt angles for the UP and DN directions with respect to the sample normal. However, there is no evidence of this in several of our devices, and hence we do not attempt to analyze this effect.

5.2.1 Physics of tuning low barrier PMA magnet through in-plane spins

Since the polarization direction of the generated spins due to the charge current through the GSHE underlayer lies in the X-Y plane, it is surprising to see a tunability of the perpendicular magnetization by the DC current. An obvious hypothesis that we first considered was: the Oersted field generated by I_{DC} points along the Z-axis at the edges of the hall bar, and could potentially favor one magnetization state over the other, leading to the observed tunability. This is illustrated in fig. 5.2 (a). To test this hypothesis, we measure the magnetization response as a function of an applied magnetic field along the Z-direction. As expected, the average magnetization shows a sigmoidal behavior, as this external field favors the UP direction for positive field values and DN direction for negative field values.

We then repeat the same measurement in the presence of a constant I_{DC}. Any constant Oersted field in the Z direction produced by this I_{DC} would result in a horizontal shift or offset of the sigmoidal response, by an amount equal to the average magnetic field exerted on the magnet along Z-direction due to I_{DC}. We measure this shift, "B_{offset}" for various I_{DC} and plot B_{offset} vs. I_{DC} in the right graph of fig. 5.2 (b). There are two observations from this graph that contradict the hypothesis of the Oersted field induced tunability. Firstly, B_{offset} is not a linear function of I_{DC}, which is different from the Oersted field linearly following the current, $B = \mu_0 I_{DC}/2W$. It can be clearly seen that B_{offset} saturates for $|I_{DC}| > 10\ \mu A$. Secondly, in the region where B_{offset} is linear with I_{DC}, the slope, $B_{offset}/I_{DC} = 4 \times 10^{-1}\ mT/\mu A$, is much larger than the expected value of $\mu_0/2W = 3 \times 10^{-3}\ mT/\mu A$ for the case of current induced Oersted field. The possibility of a second order anisotropy term [101] being

responsible for the observed tunability was also considered through sLLG simulations and was found to be inadequate to explain the experiments. The simulation model and results are presented in supplementary section III of the parent paper of this chapter.

We therefore hypothesize that a slightly tilted magnetic anisotropy direction is responsible for the observed tunability, as illustrated in fig. 5.2 (c). Essentially, if the magnetization tilt is in the X-Z plane, it can lead to X-polarized spins in the SOT underlayer favoring one state over other. A +X directed spin will favor the (X, Z) quadrant for the magnetization, resulting in a positive m_Z, which will register as an UP in the AHE measurement (since R_{AHE} is proportional to m_Z). On the other hand, a –X directed spin will favor the (-X,-Z) quadrant, resulting in a negative m_Z or DN direction for the magnetization. This is similar to the engineered tilted anisotropy work by You et al. [93] applied on stable, large barrier magnets. In our case, since the magnetic stack is designed to have a very low perpendicular anisotropy, any small in-plane anisotropy developed during the film deposition process can lead to a significant tilt angle that is otherwise undetectable in magnets with strong perpendicular anisotropy. To test out this hypothesis, we carry out AHE measurements as a function of external magnetic fields along Z, Y and X directions on another device made of the same stack. Firstly, we carry out R_{AHE} vs. B_Z measurements as shown in fig. 5.2 (d) left plot. It can be seen that the saturation value of R_{AHE} is noticeably larger than the remanent value. The tilt angle, θ can be estimated by the relation $\theta = cos^{-1}(R_{AHE,remanent}/R_{AHE,saturation})$ as is done by You et al. [93]. From the measured data, $\theta$is estimated to be around 25 degrees. Next, we carryout R_{AHE} measurements in the present of B_X (black curve) and B_Y (blue curve), shown in fig. 5.2 (d) right plot. In these measurements, the R_{AHE} saturates to a zero value for large applied fields (B > B_{sat}) since the perpendicular component of the magnetization vanishes as the magnetization is progressively forced to lie in the X-Y plane. By comparing B_{sat} for the X directed field and Y directed field, it is seen that the magnetization can be forced along the X direction more easily than the Y direction,

as $B_{sat,X} < B_{sat,Y}$. This suggests that the tilt direction is in the Z-X plane, toward the X-axis.

In the fabricated devices, a precise tilt angle was not engineered. However, it was observed that the DC current tunability curves for most of our working devices had similar current requirements (as shown in Supplementary information, section IV of the parent paper of this chapter). This leads us to believe that orientation and magnitude of tilt was consistent among devices.

Furthermore, the feasibility of SOT based output tunability of a p-bit made of a low barrier PMA magnet with tilted anisotropy is confirmed by numerically solving the stochastic Landau-Lifshitz-Gilbert (sLLG) equation with a monodomain macro-spin assumption.These simulations, presented in the parent paper, reproduce the experimentally observed tunability with DC current when the tilt angle was set to $\theta > 10^o$.

Further, sLLG simulations are performed for the magnetization of the LBNM as a function of an externally applied Z-directed magnetic field in the presence X-polarized DC spin current. This simulation is performed to capture the experimental scenario of fig. 5.2 (b). The B_{offset} values are extracted following the same protocol as in fig. 5.2 (b). The B_{offset} vs. I_{DC} curve obtained from this sLLG simulation with tilted anisotropy captures the key features of the experimental observation: (i) the B_{offset} value saturates for large I_{DC} values, (ii) the slope of B_{offset} vs. I_{DC} is much larger than that expected from the Oersted field associated with I_{DC}. When the tilt angle of the anisotropy axis was set to 0^o, neither of the two features are observed in the simulation. These simulation results further strengthen our hypothesis that the observed effects are due to a tilted magnetization anisotropy of the LBNM.

NOTE: The sLLG simulations discussed in this section is performed by Rafatul Faria.

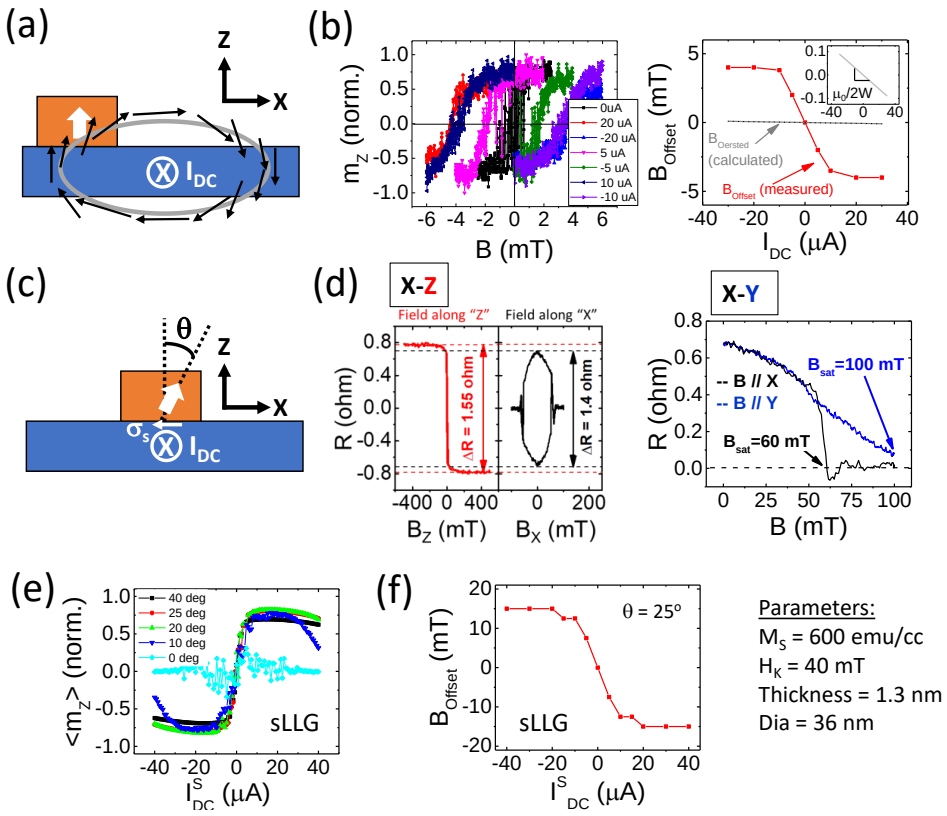

Parameters:
M_S = 600 emu/cc
H_K = 40 mT
Thickness = 1.3 nm
Dia = 36 nm

Fig. 5.2. (a) Possible explanation of the obtained tunability. A lithographic misalignment could lead to the magnet island being situated towards one edge of the Ta electrode, where the perpendicular component of the Oersted field due to the charge current could lead to the observed tunability. (b) Device output as a function of external magnetic field in the Z-direction, in the presence of DC current through the GSHE underlayer. Offset field (B_{offset}) due to I_{DC} is obtained from the horizontal shift in the output curves. The plot on the right shows B_{offset} vs. I_{DC}, which clearly displays a saturating behavior. Also, the slope in the linear region is more than two orders of magnitude larger than that expected from the Oersted field shown in grey (zoomed in figure in inset). (c) Another possible explanation of the obtained tunability. A tilted anisotropy in the nanomagnet leads to a non-zero m_x component of the magnetization that can be tuned by the spin current through the GHSE underlayer. Due to the tilted anisotropy field, tuning m_x by the in plane spin currents leads to tuning m_z. (d) Measured anomalous Hall signal as a function of magnetic field in X, Y and Z direction. From the X-Z plot, we can deduce the tilt angle θ from the ratio of saturation signal. From the X-Y plot, we notice that it is easier to saturate the magnetization in plane in the X direction compared to the Y direction, suggesting that the tilt of magnetization lies in the X-Z plane. (e) sLLG simulations of the above device with an applied DC charge current for various magnetization tilt angles. The charge current flows in the Y direction in the GSHE underlayer, producing spins with polarization along X direction that are responsible for the observed tunability. (f) The experimental scenario of (b) is numerically simulated to extract the B_{offset} vs. I_{DC}, which shows the qualitative features of experimentally obtained curve: (i) saturation of the B_{offset} for large I_{DC} (ii) large slope of B_{offset} vs. I_{DC} compared to that expected from Oersted field. The quantitative value of slope and saturation field is different because of the different magnet dimensions compared to the experiment.

5.3 Electrically coupled network of two p-bits

In this section, we study two electrically coupled p-bits. The stochastic output of the first p-bit ("driver") is amplified and provided as the input to the GSHE underlayer of the next p-bit ("follower"). The amplification is done by SRS 830 lockin amplifiers, with an averaging time of 3 ms, which is much smaller than any other time scale in the experiment. The outputs of the lockin amplifiers are then fed to comparators in order to digitize the signals. We vary the connection configuration between the two devices to observe their behaviors. Fig. 5.3 (a) illustrates the circuit setup with the device on the left being the drive and the device on the right being the follower. The connection strength between the two devices is controlled by changing the R_{weight} shown in the same figure. We study three configurations: no connection ($R_{weight} = \infty$), positive connection ($R_{weight} = 400\ K\Omega$ and amplifier gain is positive) and negative connection ($R_{weight} = 400\ K\Omega$ and amplifier gain is negative). Fig. 5.3 (b) shows the normalized autocorrelation of the output signals of the two devices ($\hat{A}_{driver}$ and $\hat{A}_{follower}$) for the three configurations, obtained by the following formula:

$$\begin{aligned} A_{driver}(\Delta t) &= \textstyle\sum_{t=0}^{T-\Delta t}(X_t - \bar{X})(X_{t+\Delta t} - \bar{X}) \\ A_{follower}(\Delta t) &= \textstyle\sum_{t=0}^{T-\Delta t}(Y_t - \bar{Y})(Y_{t+\Delta t} - \bar{Y}) \end{aligned} \tag{5.1}$$

$$\begin{aligned} \hat{A}_{driver}(\Delta t) &= \tfrac{A_{driver}(\Delta t)}{A_{driver}(0)} \\ \hat{A}_{follower}(\Delta t) &= \tfrac{A_{follower}(\Delta t)}{A_{follower}(0)} \end{aligned} \tag{5.2}$$

In the above formulae, X_t and Y_t are the state of the driver and follower respectively at time t; $\bar{X}$ and $\bar{Y}$ are the respective mean values; T is the total measurement time. As seen in fig. 5.3 (b), when unconnected, the two devices fluctuate at different time scales, evidenced by the markedly different full width at half maximum ($FWHM$) of their autocorrelation peaks. However, when either a positive or negative connection is established between the two devices, the fluctuation time scale of the follower ($FWHM_{follower}$) becomes closer to that of the driver ($FWHM_{driver}$).

Fig. 5.3 (c) and (f) show representative sections of the time traces of the output signals of the driver (X_t) and the follower (Y_t) for positive and negative connection

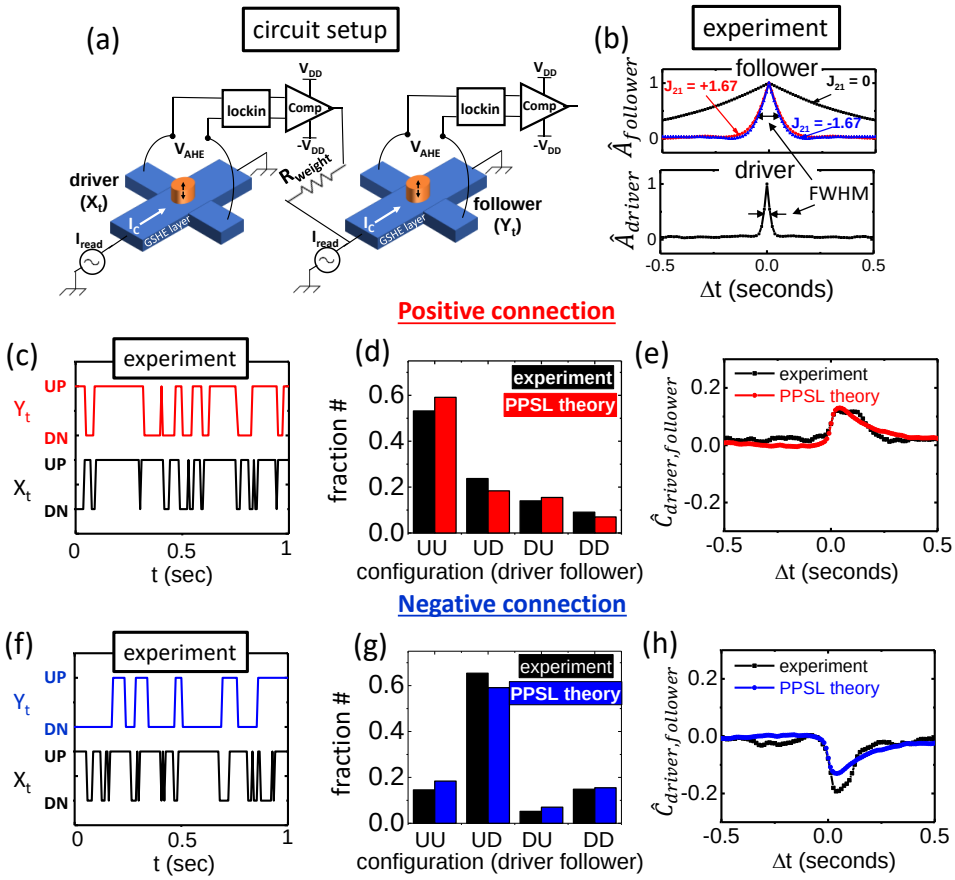

Fig. 5.3. (a) The circuit to implement directed connection between two p-bits. (b) Normalized auto correlation of the outputs of the driver (bottom) and the follower (top) for different connection configurations. Follower p-bit is much slower than driver for no connection case, but starts to respond faster when positive or negative connection is established between the two p-bits. (c) Time traces of the two p-bits. With positive connection established between them, positive correlation starts appearing, which is also seen from by plotting the histograms of the four possible states in (d). The parallel configurations (UU) are more frequent. This is closely matched by PPSL simulations. (e) The "relatedness" between the driver and follower signals is quantified by the cross correlation, which shows a positive peak. The correlation coefficient given by the height of the peak and the time scale of the correlation, given by the $FWHM$ of the peak are both closely matched by PPSL simulations. (f) (g) and (h) are for the case of negative correlation.

respectively, where the emergence of positive and negative relation can be observed. To quantify the relatedness between the two signals, the histogram of the four possible configurations are plotted in fig. 5.3 (d) and (g). It is observed that the driver signal has some inherent bias towards the UP state, possibly due to the presence of an unwanted magnetic field in the measurement chamber. Therefore, to accurately quantify the relatedness between the two outputs, we calculate the cross correlation between the two signals ($C_{driver,follower}$), obtained by introducing a relative time shift (Δt) between the two output signals and calculating the inner product as a function of this shift according to the following formula:

$$C_{driver,follower}(\Delta t) = \sum_{t=0}^{T-\Delta t} (Y_t - \bar{Y})(X_{t+\Delta t} - \bar{X}) \tag{5.3}$$

This metric is less prone to the inherent bias as the correlations are calculated from signals after subtracting their respective mean values. Also, this metric preserves the time dependence of the relatedness. Any misleading relatedness observed in the histogram due to inherent biases in the two signals would not have time dependence, and hence would not contribute to the peak structure on the cross correlation plots.

We plot the normalized cross correlation obtained from the following normalization:

$$\hat{C}_{driver,follower}(\Delta t) = \frac{C_{driver,follower}(\Delta t)}{(A_{driver}(0) \times A_{follower}(0))^{1/2}} \tag{5.4}$$

The black curves in fig. 5.3 (e) and (h) show $\hat{C}_{driver,follower}$. The correlation coefficient is just the peak value of $\hat{C}_{driver,follower}$. From the above analysis we obtain the following insights for the different connection configurations.

No Connection: For the no connection case ($R_{weight} = \infty$), the outputs of the two devices are essentially two independent random bit streams. An important finding from this experiment is that the two unconnected p-bits here have markedly different time scales of fluctuation, as is seen by the FWHM of the auto correlation plots for driver and follower signals in fig. 5.3 (b). The driver fluctuates at a faster time scale, with an $FWHM_{driver} = 24$ ms, whereas that for the follower p-bit is much slower with a $FWHM_{follower}$ of 648 ms.

Positive/Negative connection: Next, we use $R_{weight} = 400\ K\Omega$ and choose the connection polarity to implement a positive correlation. The choice of R_{weight} and V_{DD} together result in a current of 25 μA input to the second device, which is smaller than the critical current required for deterministic switching of the magnetization direction. Considering a magnet with an energy barrier of $E_B \approx 15k_BT$, spin Hall angle of Tantalum, $\theta_{SHE,Ta} = 0.07$ and the Hall bar width of W =200 nm, the critical switching current without thermal assistance can be calculated to be $I_{critical}$ ≈300 μA from the formula given by Liu et al. [63]. Therefore, the current required here for establishing a correlation between the two p-bits is more than 10 times smaller than $I_{critical}$. The effect of a positive connection can be seen in the time traces of fig. 5.3 (c), where the follower's output signal weakly follows that of the driver, while showing intermittent random flips. From fig. 5.3 (e), we see that the cross-correlation ($\hat{C}_{driver,follower}$) peaks around $\Delta t = 0$ and dies off with a $FWHM_{driver,follower}$ =162 ms, suggesting that the follower p-bit responds to the input provided by the driver in the time scale of the driver. It is also interesting to see that the follower, which was much slower than the driver in the unconnected case, starts to respond with a speed close to that of the driver for the positive connection case. This is quantified by the $FWHM_{follower}$ decreasing to 100 ms, as shown in fig. 5.1 (b) red curve. Similarly, for the negative connection case, a negative peak in the cross correlation can be seen around $\Delta t = 0$ as seen in fig. 5.3 (h). The speed of the follower becomes closer to that of the driver, as quantified by the reduction in the $FWHM_{follower}$ to 75 ms, as shown in fig. 5.1 (b) blue curve.

There are two findings from the above experiments that are of critical importance for large networks of interconnected p-bits: 1. A weak electrical interconnection, which is more than 10 times smaller current than that required for deterministic switching, is sufficient to induce correlations between two p-bits. Weak interconnection strength is crucial for low power consumption in a large network. Moreover, as correlations are present even with weak interconnection strengths, it allows for electrical annealing [38], where the interconnection strength can be gradually turned

up to further enhance the desired correlations and suppress the undesired ones. 2. A large difference in the natural time scales of the two devices does not hamper the operation of such circuits. Another important factor for a large p-bit network is its robustness against device to device variations. Specifically, the natural fluctuation time scales of the p-bits depend exponentially on the energy barrier of the individual nanomagnet, which can have a distribution due to process variability. Therefore, for a network of p-bits with different energy barriers to work as desired, correlations need to be established even with different individual fluctuation time scales. This important requirement has been verified in our experiments, where correlations were successfully established between the two p-bits despite their natural time scales being very different (24 ms and 648 ms for driver and follower respectively). The effect of time scale variation on the cross correlation between the driver and the follower p-bit is studied using numerical simulations of eq. 8-10 and is presented in supplementary information, section V of the parent paper.

5.4 Conclusion

In summary, we have demonstrated for the first time, a stochastic nanomagnet with perpendicular anisotropy, tunable by an in-plane spin current. We hypothesize the possibility of a tilted anisotropy being responsible for the observed tunability, which is supported by both experiments and sLLG simulations. We further demonstrate a coupled network of two such stochastic devices, namely p-bits, and show that correlations between their stochastic outputs can be manipulated through weak electrical interconnections, despite having difference in their natural fluctuation time scale.

Acknowledgment

P.D. would like to gratefully acknowledge Prof. Pramey Upadhyaya for suggesting the thickness optimization method to obtain weak anisotropy PMA stacks. This work

was supported by the Center for Probabilistic Spin Logic for Low-Energy Boolean and Non-Boolean Computing (CAPSL), one of the Nanoelectronic Computing Research (nCORE) Centers as task 2759.003 and 2759.004, a Semiconductor Research Corporation (SRC) program sponsored by the NSF through CCF 1739635.

6. PHASE SYNCHRONIZATION AND FREQUENCY TUNABILITY IN WEAK ANISOTROPY PERPENDICULAR NANOMAGNETS

Most of the materials in this chapter have been extracted verbatim from the paper: Debashis, Punyashloka et al. "Phase synchronization and frequency tunability in weak anisotropy perpendicular nanomagnets" 77th Device Research Conference (DRC). IEEE, 2019; and Debashis, Punyashloka et al. "Spin orbit torque controlled stochastic oscillators with phase synchronization and frequency tunability", in preparation (2020)

6.1 Introduction

Recently, there has been emerging research in the area of stochastic oscillators, which utilize the ambient thermal noise to facilitate synchronization. In such oscillators, the state of the device shows self-sustained random fluctuations between two metastable states driven by the ambient thermal noise, which determines an average fluctuation rate. A clear advantage of such stochastic oscillators is that no power is required to sustain the oscillations, unlike the periodic oscillators [102–106]. Furthermore, it has been shown theoretically [107, 108] that such oscillators can be synchronized with external periodic excitations through the phenomenon of stochastic resonance [109]. Experimentally, there are very few demonstration with nanoscale solid state devices [110–113]. Locatelli et al. [53] demonstrated stochastic resonance using spin transfer torque (STT) in a two terminal device based on a low barrier MTJ.

In this work, we demonstrate stochastic resonance based synchronization in a three terminal device geometry, utilizing spin orbit torque (SOT). Furthermore, by

feeding the device output back to its input through a simple resistor, we show that this synchronization frequency can be tuned electrically.

6.2 Synchronization with an external periodic drive

We described in the chapter 5, how the application of a DC current to the GSHE input of the device can be viewed as producing an effective tilt in the energy barrier towards one of the UP or DN states, depending on the current polarity. When a sinusoidal current is applied to the giant spin Hall effect (GHSE) input of the device, the energy landscape is periodically tilted towards the UP and the DN states during the positive and negative half cycle of the sinusoid respectively as shown in fig. 6.1. When the frequency of this sinusoidal perturbation to the energy landscape matches that of the average transition frequency of the magnetization between the two states, the phenomenon of stochastic resonance [109] takes effect. In this case, the magnetization periodically fluctuates between the two states, completely in synchronization with the external periodic perturbation. It is to be noted here that the amplitude of the external periodic perturbation is much smaller than that required for deterministic forcing of the magnetization to one state or the other. Fig. 6.2 (a) shows the measurement configuration with the external sinusoidal current provided to the device input. With the input turned off, the device output shows random fluctuations as seen by its time trace. The histograms of dwell times are well fitted by an exponential envelope (fig. 6.2 (b)) to give the average natural frequency (f_0) to be 5 Hz.

Next, a sinusoidal current is provided to the device input and its output is recorded. This measurement is then repeated for different frequencies (f_{in}) of the input sinusoidal current. Fig. 6.2 (c) shows the output time traces of the device for three different input frequencies, while fig. 6.2 (e) plots the dwell time histograms for these time traces. First, for $f_{in} = 100$ Hz, which is much larger than f_0, it can be seen that the device output is random and the corresponding dwell time histogram

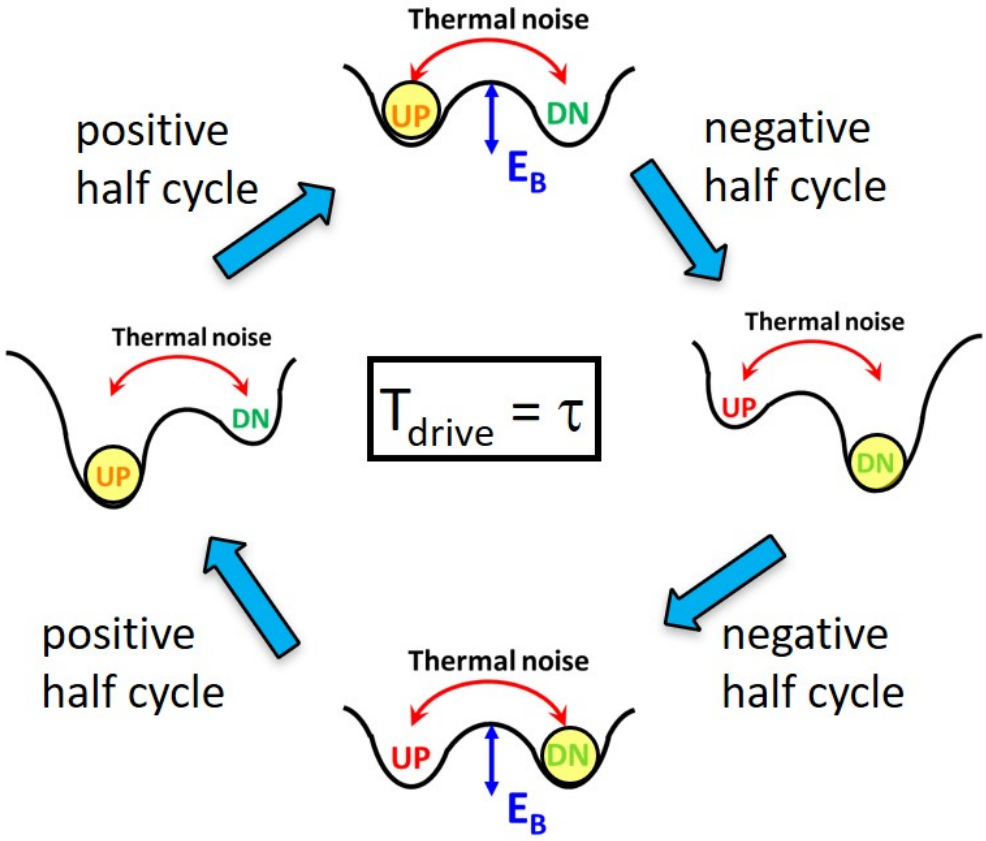

Fig. 6.1. A system having a double well potential is shown, with the two metastable states being named UP and DN, separated by energy barrier E_B. It involves two time scales: (i) the average thermal transition rate (τ^{-1}), fixed by the energy barrier separating the two wells and (ii) the rate of external periodic perturbation (T_{drive}^{-1}). When $T_{drive}^{-1} = \tau^{-1}$, the transitions themselves become periodic.

has an exponential envelope. This suggests that for $f_{in} = 100$ Hz, the device output is unaffected by the input current. Next, when f_{in} is changed to 5 Hz, matching f_0, the device output becomes periodic and the dwell time histogram does not have an exponential envelope, rather shows a peak structure around $\tau_{UP} = \tau_{DN} = T_{in}/2$ (where $T_{in} = 1/f_{in}$), as expected for periodic output with same frequency as that of the input signal. Finally, when f_{in} is further reduced to 1 Hz, the output has a weak dependence on the input and switches sign when the input current is reversed.

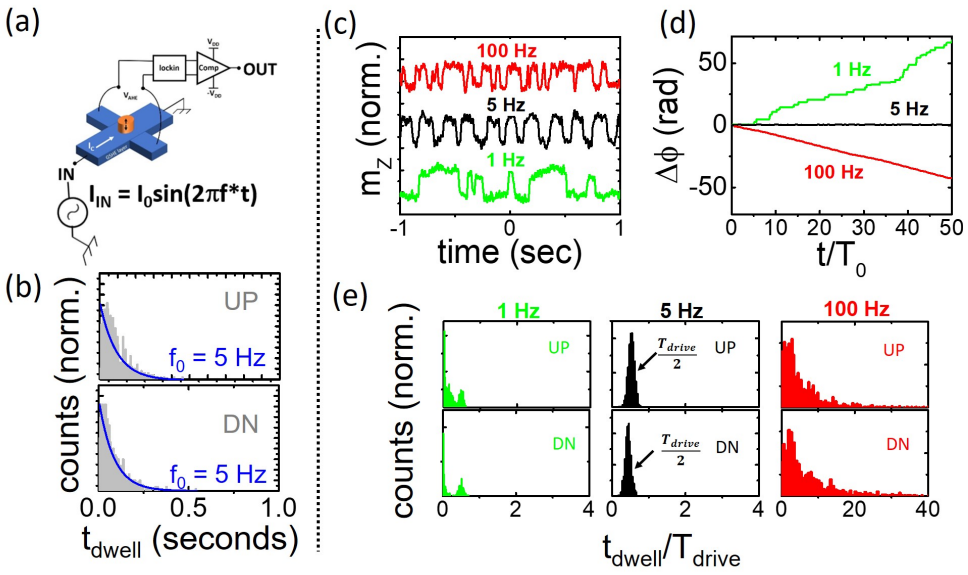

Fig. 6.2. (a) Device configuration with an external sinusoidal input with frequency f. (b) Device behavior with the external input turned off. The time trace of the output shows random telegraphic signal, confirmed by the dwell time histograms shown below it, having exponential envelopes. (c) Response of the device to sinusoidal input with different frequencies. We can see that the output looks periodic when the frequency, f, matches with the natural frequency of the device, i.e, 5 Hz. (d) This is quantified by plotting the phase difference between the input and the device output. For the 5 Hz input, the phase difference stays very close to zero (e) This is also reflected in the dwell time histograms. The peak at $t_{dwell}/T_{drive} = 0.5$ for f = 5Hz shows that the magnetization state stays in one state for half the drive time period before flipping to the other state in sync with the drive. This peak structure is not present for other input frequencies.

However, there are a large number of small dwell time transitions or "glitches". This is also evident in the dwell time histogram, where a peak is seen around $T_{in}/2$, but there is a large population of small dwell times, corresponding to the glitches discussed before. In this case, since the input current remains at a particular polarity for longer time than the average thermal transition rate of the LBNM, the probability of random switching events of the magnetization within one half cycle of the input sinusoid increases.

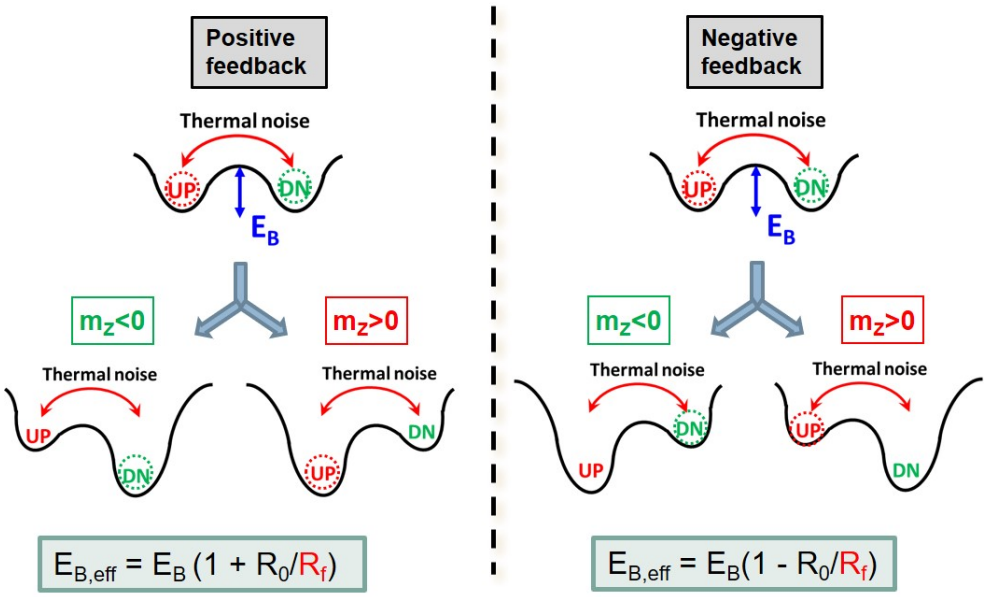

Fig. 6.3. Effect of feedback in dymanically changing the energy barrier by tilting the energy landscape towards or away from the currently occupied state in case of positive or negative feedback respectively.

In order to quantify the synchronization of the device output to the input periodic drive, fig. 6.2(d) show the linear reconstructed phase difference [108] between the input and the output signal. It can be seen that for $f_{in} = 5$ Hz, the phase difference stays around zero, showing complete phase locking of the input and output signals. For the other two frequencies, the phase difference diverges indefinitely.

6.3 Tuning the fluctuation rate through electrical feedback

When the magnetization state is amplified and fed back to the giant spin Hall effect (GSHE) underlayer, the magnetization fluctuation becomes slower or faster, depending on the polarity and strength of the feedback, analogous to temperature annealing. This can be understood by again considering the change to the energy landscape of the LBNM, as shown in fig. 6.3. In the positive feedback configuration, when magnetization is in the UP state, the device output feeds back a positive current to its input, thus tilting the energy barrier in favor the UP state, i.e, the barrier that

needs to be overcome to transition from the UP to the DN state is larger than the barrier for the reverse transition. Similarly, when the magnetization is in the DN state, barrier for going from the DN to the UP state is larger than the barrier for the reverse transition. So, the energy barrier is dynamically modified in a way such that the energy barrier appears be higher to transition from the occupied state to the other state. This in effect reduces the f_0 of the LBNM. The situation is exactly opposite in the case of the negative feedback configuration. In this case, the effective energy barrier to transition from the occupied state to the other state is lowered, hence increasing the f_0 of the LBNM.

Fig. 6.4 (a) shows the experimental schematic. The effective increase in the energy barrier due to positive feedback is seen from the steeper slope of τ vs. H_Z measurement shown in Fig. 6.4 (b). Fig. 6.4 (c) shows the time traces of the output fluctuations for different feedback configurations of another device. Fig. 6.4 (d) shows that the f_0 can be increased or decreased depending on the feedback strength and polarity (controlled in the experiment through V_{DD} of the amplifier).

6.4 Tuning the synchronization frequency of the device

We now use this method to tune the synchronization condition with an external sinusoidal input. With no feedback, the f_0 of the device is 24 Hz (fig. 6.5 (a)), as hence it synchronizes with an external sinusoidal drive when f_{drive}=25 Hz. This is seen in the phase plots of the device output and the external input (fig. 6.5 (a) bottom panel). Now, by introducing a positive feedback, the f_0 of the device changes to 8 Hz (fig. 6.5 (b)). Hence, the device output synchronizes with external drive when $f_{drive} = 15$ Hz (fig. 6.5 (b) bottom panel). Thus, we demonstrate electrically tunable synchronization of our stochastic oscillators.

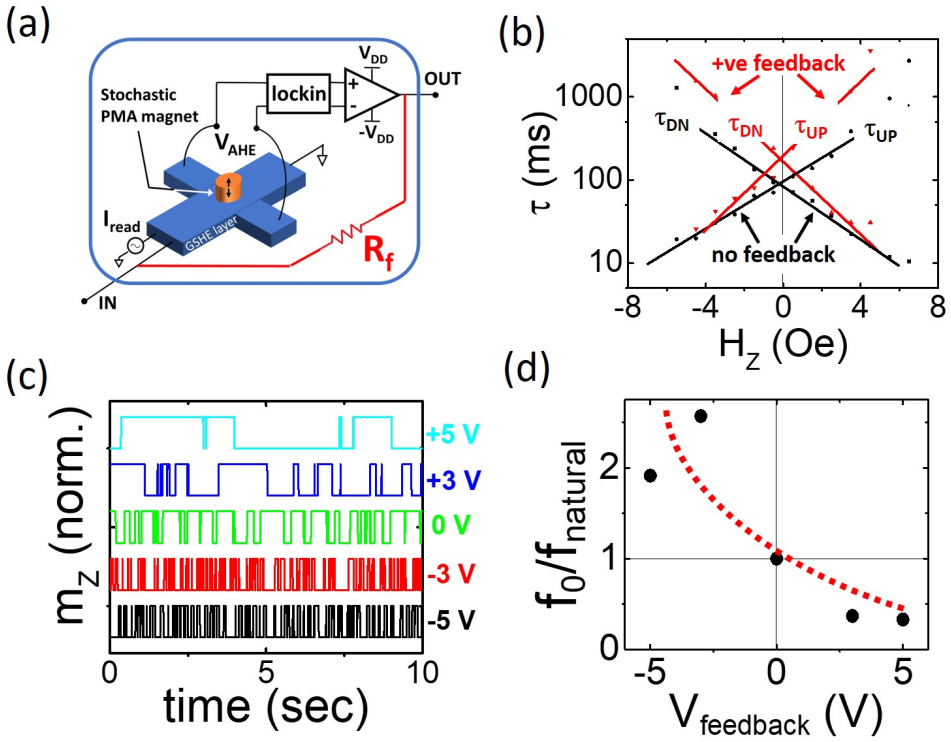

Fig. 6.4. (a) Schematic of the device with feedback provided by R_{weight} shown in red. (b) τ_{UP} and τ_{DN} measurement as a function of externally applied field in Z-direction. The larger slope for the +ve feedback case (red lines) suggests a larger effective E_B. (c) Time traces of another device output for different feedback configurations. The electrical feedback provided by amplifying the output and connecting it to the input through a resistor, R_{weight}. The voltage labels for each time trace corresponds to the V_{DD} of the amplifier used. Negative V_{DD} values mean negative feedback. (b) The mean oscillation frequency vs. V_{DD} of the amplifier, quantifying the effect of the feedback. Here $f_{natural}$ is the average frequency of the device without any feedback.

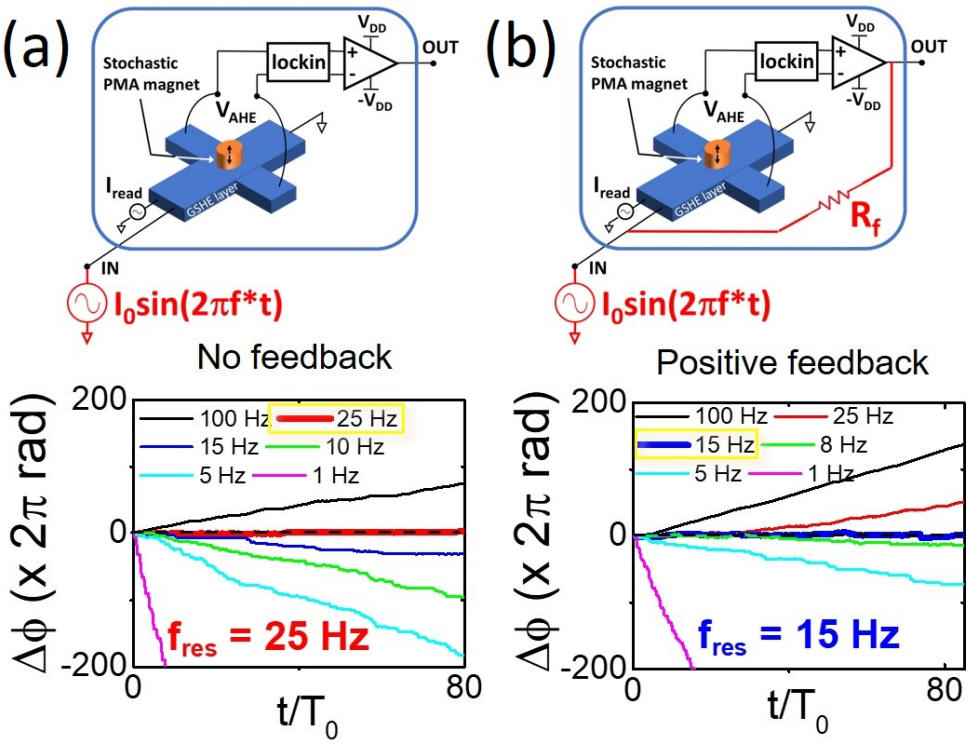

Fig. 6.5. (a) – (b) show the measurements of synchronization to an external sinusoidal drive with and without feedback. (a) shows the phase difference between the device output and an external sinusoidal input for different frequencies of the input. The synchronization frequency for the device output is 25 Hz for no feedback configuration. (b) shows the results of same measurement but with an additional positive feedback in place. The synchronization frequency changes to 15 Hz in this positive feedback configuration.

Acknowledgement

This work was supported by the Center for Probabilistic Spin Logic for Low-Energy Boolean and Non-Boolean Computing (CAPSL), one of the Nanoelectronic Computing Research (nCORE) Centers as task 2759.003 and 2759.004, a Semiconductor Research Corporation (SRC) program sponsored by the NSF through CCF 1739635002E.

7. REALIZATION OF A SPIN LOGIC DEVICE WITH COMPOSITE MAGNETIC STACK

Most of the materials in this chapter have been extracted verbatim from the paper: Debashis, Punyashloka, and Zhihong Chen. "Experimental Demonstration of a Spin Logic Device with Deterministic and Stochastic Mode of Operation." Scientific reports 8.1 (2018): 11405.

Building logic units with spintronic elements is a topic of great interest as they can offer the functionality of a logic device at lower power and at the same time serve as memory elements, owing to the non-volatile nature of nanomagnets. Driven by this idea, many proposals of spin based logic devices have been widely discussed [48, 114–116]. Charge-coupled spin logic (CSL) [48] is one of the most promising implementations due to the use of robust charge currents for long transport distances as terminal quantities. The CSL design consists of a WRITE unit into which information can be written by an external stimulus and a READ unit from which the information can be read out and supplied to the next stage as input. Most importantly, the WRITE and the READ units must be electrically isolated to eliminate feedback, at the same time should be directionally coupled so that information can be transferred from the WRITE unit to the READ unit. In the original CSL proposal, giant spin Hall effect (GSHE) was proposed to be the writing mechanism and magnetic tunnel junction (MTJ) was suggested as the READ unit (fig. 7.1).

Although the physics and operation of GSHE and MTJ are both well established, a final experimental demonstration of a CSL like spin logic device that meets design criteria of a logic device is still missing. One of the essential missing components is the experimental demonstration of an electrically isolated but directionally coupled READ and WRITE unit.

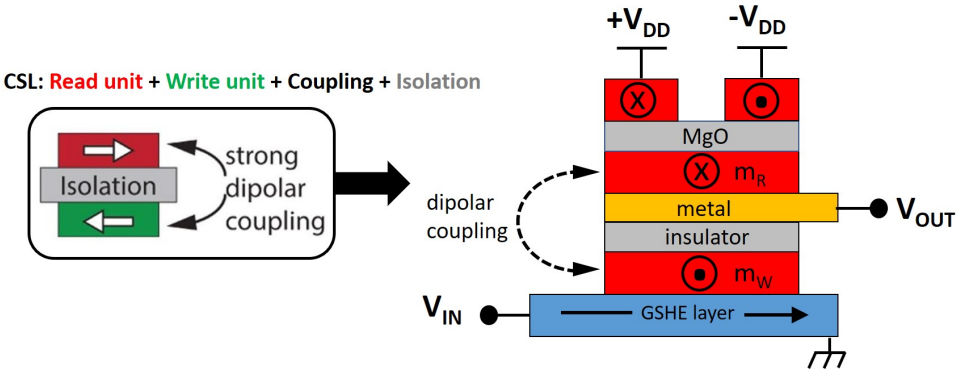

Fig. 7.1. **CSL device implementation:** The original CSL device proposal has a GSHE based write-unit and a MTJ based read-unit. The coupling between the read and the write unit is implemented via dipolar interaction between m_W and m_R

In this work, we present an implementation of the charge spin logic device, that demonstrates the aspect of directional coupling, while utilizing simple mechanisms to implement an electrical READ and WRITE unit. The presented device has (i) an in plane magnetic anisotropy (IMA) magnet driven by Oersted field as the WRITE unit, (ii) a perpendicular magnetic anisotropy (PMA) magnet switched by the giant spin Hall effect (GSHE) of tantalum and utilizing anomalous Hall effect (AHE) as the READ unit and (iii) the symmetry breaking field from the IMA magnet to the PMA magnet as the directional coupling. The nearby IMA magnet dictates the response of PMA to the GSHE spin torque. By writing information into the IMA through Oersted field and reading information from the AHE of the PMA, a new CSL device is successfully implemented with the combined PMA-IMA stack.

In contrast to the originally proposed implementation of CSL, the coupling between WRITE and READ is realized by a very small dipolar field from the IMA that is sufficient to break the symmetry of GSHE switching of the PMA (fig. 7.2). This weak coupling relaxes the design constraints on the isolation layers and magnet dimensions [117], i.e., we can now design thicker isolation layers for improved read-write isolation and endurance, and thinner magnets for lower operation energy.

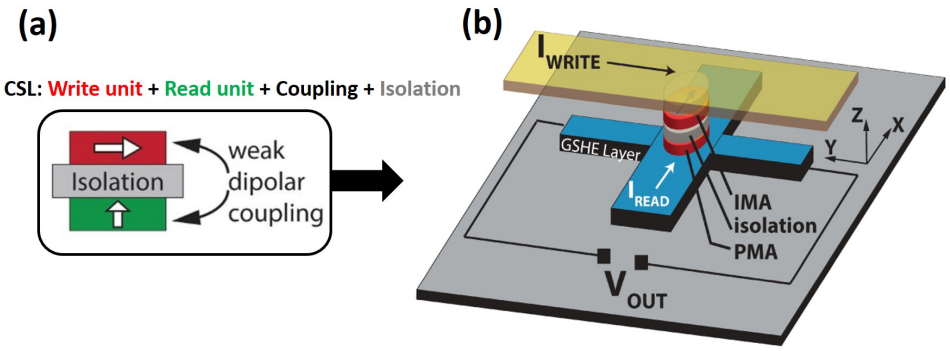

Fig. 7.2. **New CSL device idea:** (a) The original proposal was based on two IMA magnets and a strong coupling between them that can switch them in unison. Here, the idea is to have an IMA magnet and a PMA magnet. A much smaller dipolar field from the IMA magnet is required to break the symmetry of GSHE switching of the PMA magnet underneath, achieving information flow from WRITE to READ unit. (b) Schematic of the coupled IMA-PMA device.

We emphasize that the read and write mechanisms of the presented device can be replaced by more efficient technologies. For example, the WRITE unit can employ spin orbit torque (SOT) switching of the IMA magnet by having a GSHE material like Tantalum adjacent to it [28]. It can also utilize recent advances in voltage control of magnetization [118,119]. The READ unit can include a PMA-MTJ [27] similar to the original CSL proposal. These mechanisms can be integrated based on the application needs or desired performance metrics as long as they fulfill the requirements of the coupled IMA-PMA device design shown in fig. 7.2. The specific design presented in this paper is just one of the designs used for easy integration, while the main focus is to experimentally demonstrate a CSL operation as the first proof-of-concept spin logic unit with input/output isolation and directed coupling.

7.1 Experimental approach and results

We begin with depositing a composite stack of PMA and IMA magnet separated by 6–7 nm MgO that serves as the electrical isolation between them. This composite

stack sits on a 7 nm Ta GSHE layer (fig. 7.3 (a)). Vibrating sample magnetometry (VSM) measurements using a superconducting quantum interference device (SQUID) on control samples reveal good ferromagnetic behaviors, with a high ratio of remnant moment to saturation moment and abrupt magnetization reversal for both IMA and PMA layers (fig. 7.3 (b,c)). Next, the Ta layer is patterned into a Hall bar with the composite IMA-PMA stack sitting on top shaped into an ellipse with major and minor diameter of 3 μm and 1 μm, respectively (fig. 7.3 (d)). AHE measurements done with external out-of-plane feld (fig. 7.3 (e)) show square hysteresis loop (fig. 7.3 (f)), confirming two distinguished magnetization states. Te IMA signal does not impact this measurement as it is isolated by the MgO layer. Note, the coercive field in fig. 7.3 (f) is larger than that in fig. 7.3 (c), as a result of patterning the PMA stack into a smaller island [120]. The impact of the stray magnetic field from the IMA on the PMA magnet's coercive field is minimal as both of its in plane and out of plane components are less than 1 mT.

7.1.1 Switching PMA with in plane polarized spin current

As first shown by Miron et al. [83] and Liu et al. [63], in-plane polarized spin currents can produce SOT that can efficiently rotate the magnetization of a PMA deterministically in the presence of a small symmetry breaking in-plane field. In this scenario, the critical current needed to switch a PMA magnet can be much smaller than for an IMA magnet with the same energy barrier, due to the absence of a demagnetization field for PMA magnet (see eq. 7.4). However, the requirement of an in plane field to deterministically switch the PMA magnetization from "up" to "down" (or "down" to "up") makes it undesirable for computing applications. Many approaches have been demonstrated to get rid of this external field. These approaches introduce a built-in symmetry breaking field, by means of either a tilted anisotropy [93], lateral structural anisotropy [94], interlayer exchange coupling [95] or the GSHE of an antiferromagnet [97]. All these methods rely on a mechanism that

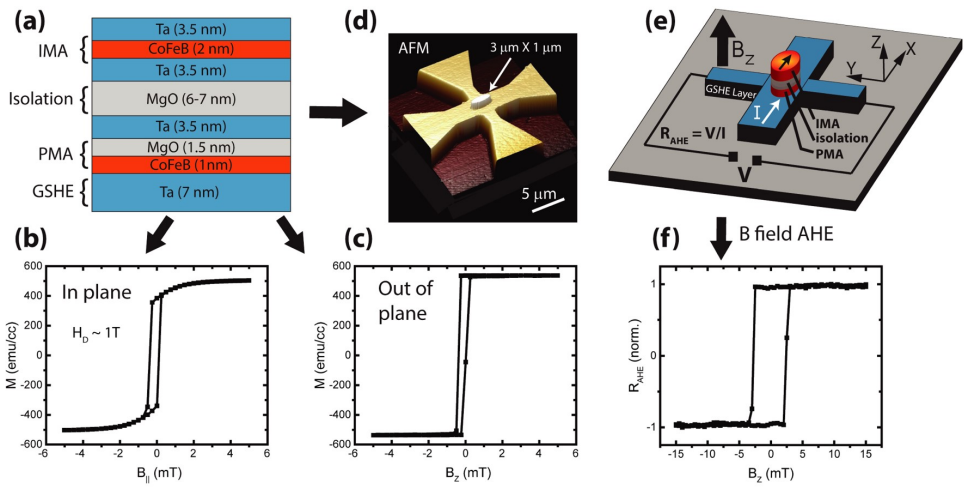

Fig. 7.3. **Composite IMA-PMA stack characterization:** (a) The composite stack of IMA and PMA magnets, separated by 6–7 nm MgO as the electrical isolation. The stack sits on 7 nm Ta that serves as the GSHE layer for the PMA magnet switching. (b,c) SQUID characterization of separately deposited IMA and PMA magnetic stack, showing good in-plane and out-of plane ferromagnetic behavior, respectively. (d,e) AFM and schematic of the fabricated device having a Ta Hall cross and an elliptical island of the composite IMA-PMA stack. (f) AHE resistance vs. externally applied out of plane magnetic field, showing abrupt hysteretic behavior that is indicative of the PMA in the etched island.

produces a fixed in-plane symmetry-breaking field that cannot be manipulated easily once the device is fabricated.

7.1.2 Field free switching by means of a coupled IMA

We eliminate the requirement of the external symmetry-breaking field by using the dipolar field of the IMA magnet placed on top of the PMA magnet. This approach eliminates the challenging fabrication requirements of refs [93,94] and does not require complicated interlayer and antiferromagnetic material stack as in the case of refs [95, 97]. More importantly, this approach allows for an independent electrical control

of the magnetization of the IMA magnet, enabling an input and an output control for logic functionality as will be described in later sections.

The measurement schematic is shown in fig. 7.4 (a). First, we carry out switching loop measurements of the PMA magnet with the assistance of an external magnetic field of +/100 mT, as shown in fig. 7.4 (b). The polarity of the external field and applied current direction determine the final magnetic state of the PMA as "up" or "down", represented by the two R_{AHE} levels. It should be noted here, that the effect of the IMA dipolar field, which is expected to be no more than 1 mT, is overshadowed by the large external in plane field. The switching loop direction and symmetry is consistent with that observed by Liu et al.17 For SOT switching of PMA magnets without any assistance from heat induced thermal activation, the analytical expression for critical switching current is given by [63]:

$$J_{sw,PMA} \approx \frac{2e}{\hbar}\left(\frac{1}{2}M_S H_C t_{PMA}\right)\left(\frac{1}{\theta_{SH}}\right)\left(\frac{1}{1-sech(t_{GSHE}/\lambda_{SF})}\right) \tag{7.1}$$

where M_S and H_C are the saturation magnetization and the switching field of the PMA magnet, t_{GSHE} and t_{PMA} are the thickness of the GSHE and PMA magnet layer, θ_{SH} is the spin Hall angle and λ_{SF} is the spin difusion length of the GSHE layer. Substituting numbers measured from the experiment and taking $\lambda_{SF} = 1.4$ nm and $\theta_{SH} = 0.07$ from ref [63], $J_{sw,PMA} = 3.6 \times 10^6 A/cm^2$ is calculated. Although the above expression for critical current is for a monodomain magnetic body with $H_C \approx H_K$, and is not expected to match our experiment with micron sized magnets, the calculated number is consistent with the experimental values in fig. 7.4. We also performed measurements for switching phase plots of another similar device to establish that the switching mechanism is same as that of Liu et al. [63].

Next, we carry out the switching loop measurements in the absence of external magnetic field (fig. 7.4 (c)). The IMA magnet on top exerts a fringing dipolar feld on the PMA magnet, which is strong enough to break the symmetry of the SOT switching. In the case where the IMA magnet is initialized along the positive (+x) direction, the PMA magnet senses its dipolar field pointing towards the negative (x) direction and switches along the anti-clockwise loop as if it were sitting in a negative

external field. Similarly, IMA magnet initialized along the negative direction produces a clockwise switching loop, consistent with a positive externally applied field. Based on calculations taking into account the IMA magnet size, saturation magnetization and separation from the PMA magnet, the average in plane dipolar field sensed by the PMA magnet is predicted to be ∼0.7 mT, which is strong enough to induce deterministic switching of the PMA. It is important to note that the magnetic field coming out of the IMA magnet contains both in plane and out of plane components, especially near the edges, as the two magnets are lithographically defined to have ≈100% overlap. Nevertheless, the PMA magnet switching loop still reflects the same symmetries as in the case of the uniform external in plane field. Also, the fact that the PMA magnet switches between two distinct states with the same ΔR amplitude, implies that it behaves as a "whole" and does not break into domains, even in the presence of such a non-uniform field. We further confirm that the field free switching we observe is not due to domain wall propagation as seen by Li et al. [121] Unlike in their experiment, we observe that the direction of our PMA switching loop is independent of its initial magnetization direction.

Here, we have eliminated the requirement of an external symmetry breaking field and successfully switched a PMA magnet by introducing an electrically isolated IMA magnet layer. However, initializing the IMA magnet still requires an external magnetic field, which needs to be eliminated to realize a completely field-free magnetic switch with input and output stages.

7.1.3 Completely field free, reversible device operation

As mentioned before, the IMA magnet switching in our device design can be achieved by various means such as the GSHE 11, magnetoelectric (ME) effect [118, 119] etc. In this work, we use Oersted field generated by a current pulse to switch the IMA magnet. A 50 nm thick and 6 μm wide Au electrode is formed on top of the IMA magnet, isolated by 50 nm SiO_2. This extra SiO_2 isolation is not required, but

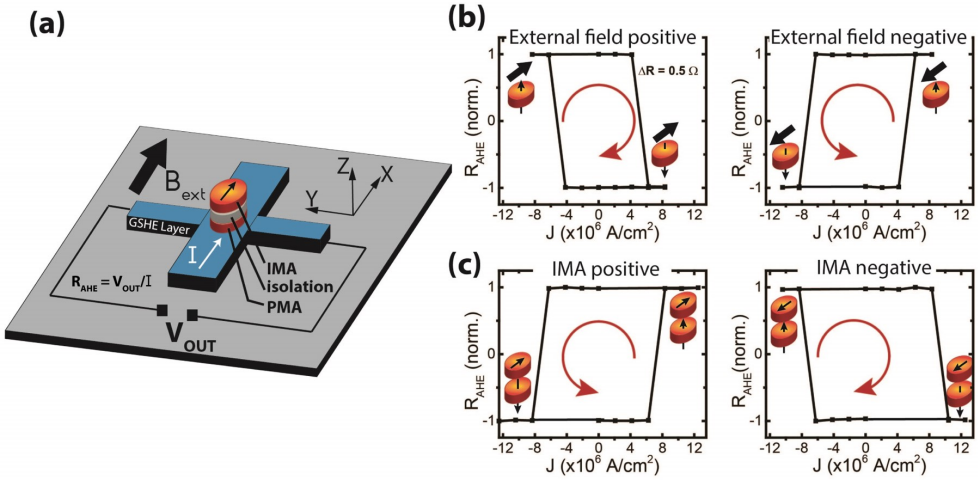

Fig. 7.4. **Field free switching:** (a) Device schematic with measurement configuration (b) GSHE switching loops in the presence of an external symmetry-breaking field. For positive magnetic field (+100 mT), positive current switches the PMA magnet from"up" to "down" magnetization, while negative current switches the PMA magnet from "down" to "up" magnetization, giving a clockwise loop direction. This is reversed when the external field is negative (100 mT), showing a counter clockwise switching loop. (c) GSHE switching loops are obtained without the aid of an external field. The loop directions are opposite to that of the external field case, indicating that a dipolar field from the IMA magnet serves as the symmetry breaking field for the GSHE switching of the PMA magnet.

is made for the ease of fabrication. When a current pulse is passed through the Au bar, transverse Oersted field (in "+x" direction) generated is sufficient to overcome the coercive field of the IMA magnet and switch its magnetization, thus enabling a completely field-free operation of the device. We would like to emphasize here that using Oersted field for IMA magnet switching is only for the ease of device fabrication (easy lithographic lift off process and less critical requirement of a clean interface with the IMA magnet for Au electrode compared to Ta or W) in our experiment. The well-established GSHE can be implemented to switch the IMA magnet by defining a Ta or W electrode through an etching process or a careful metallization process after in situ cleaning of the surface of the IMA magnet. Future generations of device designs

can also utilize magnetoelectric switching or other mechanisms to further improve energy efficiency and scalability. Te main focus of this work is to demonstrate that symmetry breaking dipolar field can be used to realize a spintronic logic device that contains electrically isolated WRITE and READ unit with logic information stored in the form of magnetization being transferred only from the input to the output.

Now we demonstrate the full operation of the device in fig. 7.5. First, the IMA magnet (WRITE unit) is initialized along the "x" direction. This exerts a positive dipolar field on the PMA magnet and the AHE of the PMA magnet shows a clockwise loop. A current pulse of 30 mA is applied to the Au electrode, which switches the IMA magnet to the "+x". This information can be read from the AHE loop of the PMA magnet, which is now in the anti-clockwise direction. Hence, the information stored in the WRITE unit, i.e., the magnetization direction of the IMA magnet, can be read from the switching direction of the PMA magnet, which serves as the READ unit. Similarly, when we apply a 30 mA pulse to the WRITE unit, it switches the IMA magnet back to the "x" direction, and results in the clockwise AHE loop of the PMA magnet. It should be noted that reading the AHE loop direction can be done easily by applying a read current larger than the critical current and reading the sign of the output voltage. For clockwise AHE loop, we always get a negative output voltage ($V_{OUT} = R_{AHE} \times I_{READ}$) and for an anti-clockwise AHE loop, we always end up with a positive output voltage.

To ensure that the GSHE switching of PMA is the responsible mechanism for the READ unit, unwanted Oersted field and Joule heating are two important mechanisms to be excluded. For our device, the Oersted field produced by the read current density of $\sim 1 \times 10^7 A/cm^2$ through the GSHE Ta layer can be estimated by the analytical expression: $H_{Oersted} = \mu_0 \times J \times (t_{GSHE}/2)$. Given all device dimensions, it is calculated to be about 0.5 mT and can be further reduced by scaling the thickness of the GSHE layer. In any case, this field points in the "y" direction, perpendicular to the direction of the current, and hence does not impact the switching symmetry of the device. Also, the Joule heating for a read current density of $\sim 1 \times 10^7 A/cm^2$ is estimated to be

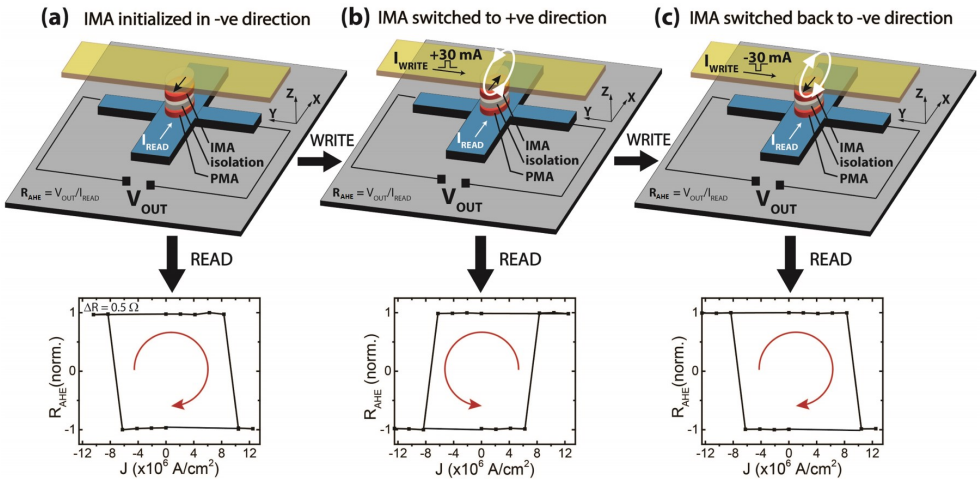

Fig. 7.5. **Full device operation:** (a) The IMA magnet is initialized in the negative direction, indicated by the arrow pointing in x direction. This is revealed by the clockwise GSHE switching loop of the PMA magnet, which serves as the READ unit. (b) A positive current pulse of 30 mA through the Au line generates an Oersted field that switches the magnetization of the IMA magnet to positive (WRITE operation). This is revealed by the counter-clockwise GSHE switching loop of the PMA magnet. (c) A negative 30 mA pulse reverses the IMA magnet direction back to negative, as revealed by the clockwise GSHE switching loop of the PMA magnet. This set of operations is completely field free and achieved by two units (IMA and PMA magnets) that are electrically isolated. Also, the information about the IMA magnet direction influences the state of the PMA magnet switching and not vice versa, hence realizing a directional coupling.

similar to other SOT based switching schemes, owing to the similar current levels. It should be noted that in spin based logic devices, the internal energy dissipated in the magnet during switching is minimal [122] and hence Joule heating is the major source of energy dissipation.

7.2 Circuit implications of the device

7.2.1 Functionality as a NOT or COPY gate

The device operates in two regimes based on the magnitude of read current. In the deterministic logic mode, it acts as a COPY gate, i.e., V_{OUT} copies I_{WRITE} irrespective of the read current polarity. Since the output of the device is the anomalous Hall voltage, which is bipolar, this device can be turned into a NOT gate by simply reversing the output terminals, which can be useful from a circuit design perspective. Since magnetization switching in response to spin current is a thresholded operation involving a critical current, the presented device is highly non-linear. The magnetization of the IMA magnet determines the switching loop of the PMA magnet through the symmetry breaking dipolar field and hence determines the polarity of the output voltage. However, the state of PMA magnet does not affect the switching phenomenon of the IMA magnet. Hence, information only flows in one direction, i.e., from state of IMA magnet to the state of the PMA magnet, ensuring directionality. This device has a built in memory as the information is stored in the state of a nanomagnet, which is non-volatile and can be stable for several years by proper design.

7.2.2 Operating power

Any CSL type of spin logic devices, where information gets transferred from the input to the output by coherent switching of two isolated nanomagnets, will always require energy to switch both of the nanomagnets, albeit it is through GSHE switching of one magnet and dipole coupling to the other in the original CSL proposal [48]. In ref. [48], this was manifested in the required switching current being $2 \times I_{sw}$ (I_{sw} being the switching current for one of the magnets). In our device, the energy is partially divided to the write operation and partially to the read operation, instead of the "traditional" way, where most energy is spent in the write operation and a much smaller energy is spent in the read operation. The write operation can be made

ultra-low power by use of magnetoelectric (ME) effect for switching the IMA magnet of the WRITE unit.

The read operation involves SOT switching of the PMA magnet of the READ unit, which requires less power compared to the SOT or STT switching of IMA magnets that are used in current MRAM technology.The expressions of the critical current for SOT switching of $40k_BT$ IMA and PMA magnets are given by17:

$$I_{sw,IMA} = \frac{4e}{\hbar}\alpha(40k_BT)\left(1+\frac{H_D}{2H_K}\right)\left(\frac{t_{GSHE}+(\sigma_{IMA}/\sigma_{GSHE})t_{IMA}}{L_{IMA}}\right)\left(\frac{1}{\theta_{SH}}\right) \quad (7.2)$$

$$I_{sw,PMA} = \frac{2e}{\hbar}\alpha(40k_BT)\left(\frac{t_{GSHE}+(\sigma_{PMA}/\sigma_{GSHE})t_{PMA}}{L_{PMA}}\right)\left(\frac{1}{\theta_{SH}}\right) \quad (7.3)$$

Hence, the required current to switch a PMA magnet is less than that for an IMA magnet with the same energy barrier by a factor of

$$\frac{I_{sw,IMA}}{I_{sw,PMA}} \approx 2\alpha\left(1+\frac{H_D}{2H_K}\right)\left(\frac{t_{GSHE}+t_{IMA}}{t_{GSHE}+t_{PMA}}\right) \quad (7.4)$$

(Here we have considered $\sigma_{IMA} \approx \sigma_{PMA} \approx \sigma_{GSHE}$ which is reasonable for CoFeB/Ta stacks) Considering values of $\alpha = 0.015$ $H_D/H_K = 150$, $t_{GSHE} = 1nm$, $t_{IMA} = 2nm$ and $t_{PMA} = 1nm$, the switching current for a PMA magnet is >3 times smaller than what is needed for an IMA magnet. Consequently, less power is required for the READ function of our device compared to the write power consumption by SOTMRAM, which is already touted to be better than STTMRAM. Note that, for the switching current comparison between IMA and PMA magnets, we have ignored heating effects that are taken into account in the expression given in reference [63]

Hence, the total operation energy (read plus write) can be significantly smaller than many of the proposed CSL like spintronic logic devices [48, 123, 124]. Note that the operation of this spin logic device is different from that of a CMOS logic device. Owing to its non-volatility, the V_{DD} power supply can be a clock instead of being constantly present. Therefore, there is no constant energy loss through the V_{DD}-ground path.

7.2.3 Concatenability

Oersted field has been used in the present device as the mechanism to write information in the state of the IMA magnet. However, a more energy efficient method such as voltage controlled magnetoelectric effect (ME) to switch the IMA magnet is preferred. In that case, the AHE output is driving a capacitive load, (e.g. the magnetoelectric WRITE unit of the next stage). In this case, the analysis goes as follows (including I_{READ} shunting consideration through PMA magnet and GSHE layer):

$$V_{OUT} = V_{AHE} = \left(\frac{\rho_{AHE}}{t_{PMA}}\right) I_{READ} = \left(\frac{\rho_{AHE}}{\rho_0}\right) \times \left(\frac{W_{PMA}}{L_{PMA}}\right) \left(1 + \frac{t_{GSHE}}{t_{PMA}}\right) V_{DD} \quad (7.5)$$

This V_{OUT} should be the critical switching voltage for the IMA magnet of the next stage.

$$V_{OUT} = V_{sw,IMA} \quad (7.6)$$

Therefore, the required V_{DD} to drive the next stage is given by:

$$V_{DD} = V_{sw,IMA} \times \frac{\rho_0}{\rho_{AHE}} \times \frac{L_{PMA}}{W_{PMA}} / \left(1 + \frac{t_{GSHE}}{t_{PMA}}\right) \quad (7.7)$$

where $V_{sw,IMA}$ is the critical voltage for switching the IMA magnet of the next stage. By proper geometrical design, the last two factors of the above equation can be reduced to 1/3, whereas for a standard material like CoFeB, the factor ρ_0/ρ_{AHE} is $\sim$30 (ref. [125]). Hence, the required V_{DD} would be $\approx 10 \times V_{sw,IMA}$. The recent advances in voltage driven 180 degree magnetization switching [118, 119] can lead to an ultra-low $V_{sw,IMA}$, enabling a low V_{DD} operation of this device. Fan-out can be improved by replacing the AHE reading scheme by a PMA MTJ, where the free layer of the MTJ receives symmetry breaking field from the IMA magnet. Using MTJ resistance instead of AHE comes at the cost of compromising the bipolar nature of output.

7.3 Conclusion

We have demonstrated an experimental implementation of a spin logic device with the essential properties of (i) WRITE unit, (ii) READ unit, (iii) directional coupling, and (iv) electrical isolation. This is achieved by combining an IMA and PMA nanomagnet in a vertical stack, utilizing the dipolar field for information transfer. The device has high non-linearity, directionality as well as inbuilt memory. Te device can be used as a COPY gate or a NOT gate, by simply choosing the polarity of output terminal connections. Te electrical write and read mechanisms can be replaced by established technology such as GSHE or emerging technology such as ME for write, and MTJ for read to reduce energy consumption and make the future generation of this device more efcient. Finally, this device has a stochastic regime of operation under high current pulses, which serves as a hardware form of a true random number generator, desirable in many computing applications

Acknowledgment

I gratefully acknowledge the fruitful discussions with Prof. Joerg Appenzeller, Prof. Supriyo Datta, Dr. Ashish Verma Penumatcha, Vaibhav Ostwal, Rafatul Faria, Dr. Kerem Yunus Camsari, Dr. Neil Dilley, Terry Hung and Tingting Shen. This work was supported by the Center for Probabilistic Spin Logic for Low-Energy Boolean and Non-Boolean Computing (CAPSL), one of the Nanoelectronic Computing Research (nCORE) Centers as task 2759.003 and 2759.004, a Semiconductor Research Corporation (SRC) program sponsored by the NSF through CCF 1739635.

8. MONOLAYER WSe_2 INDUCED ENHANCEMENT IN THE SPIN HALL EFFICIENCY OF TANTALUM

Most of the materials in this chapter have been extracted verbatim from the papers: Debashis, Punyashloka, et al. "Monolayer WSe_2 induced giant enhancement in the spin Hall efficiency of Tantalum." in review (2020).

8.1 Introduction

SOT-MRAM is a promising alternative to Spin Transfer Torque MRAM, since the novel SOT physics allows for the separation of the read and write current path, thereby improving cell endurance and reliability, and reducing the incubation delay [91, 126, 127]. Building energy efficient SOT-MRAM requires innovations in fabricating materials with large spin Hall efficiency. Most work in this regard focuses on engineering the spin orbit coupling (SOC) strength in heavy metal (HM) materials such as Ta, W, and Pt [28, 128, 129]. In ultra-thin HM films, where the thickness becomes comparable to the spin diffusion length of the material, the effective spin Hall angle (θ_{SHE}) is often reduced from the bulk value, due to spin back diffusion [130,131]. However, there could be a different path to improve the spin Hall efficiency, by creating a spin-sink to absorb the unwanted spins and enhance spin accumulation at the interface of the ferromagnet (FM) and spin Hall layer.

In this work, in contrast to the conventional HM films, we present a hybrid spin Hall stack consisting of an ultra-thin Ta layer and a ML WSe_2 that exhibits highly efficient spin generation. The ML WSe_2 acts as a sink for the spins accumulated at the bottom surface of Ta, thus preventing back diffusion of unwanted spins. Materials with large SOC are known to be effective spin sinks [132]. In fact, transition metal dichalcogenides (TMDs) have been shown to act as good spin sinks in graphene spin

valves [133, 134]. WSe_2 has been theoretically predicted to have a large SOC among the TMDs studied in literature [135–137]. Therefore, WSe_2 is expected to be a good choice for spin sink layer and is experimentally studied in this work. Utilizing this spin sink effect, we demonstrate large spin Hall efficiency in ultra-thin Ta films with thickness of 1 nm. ML WSe_2 is shown to be an excellent spin sink, and its large resistivity compared to Ta contributes to negligible current shunting. The desirable combination of large spin Hall efficiency and ultra-thin Ta is compared with other industrially relevant heavy metal stacks in terms of a suitable figure of merit for energy efficient SOT switching of magnetization.

8.2 Experimental results and discussion

8.2.1 Stack deposition and device fabrication

The film stack (starting from the topmost layer) $Ta(1)/MgO(1)/Co_{60}Fe_{20}B_{20}(1)/Ta(t_{Ta})$, is prepared by magnetron sputtering for all samples as shown in fig. 8.1 (c). We investigate two types of control samples with $t_{Ta} = 3.5$ nm (stack A) and $t_{Ta} = 1$ nm (stack B), deposited directly on thermally grown SiO_2 substrates without any underlayer (fig. 8.1 (a)). The test sample (stack C) consists of the film stack with $t_{Ta} = 1$ nm deposited on a WSe_2 underlayer, as shown in fig. 8.1 (b). All numbers in brackets above are in nanometer (nm). For the test sample, stack C, we start with the transfer of chemical vapor deposition (CVD) grown flakes of ML WSe_2 onto SiO_2 substrates, followed by sputtering of the rest of the stack. Raman spectra of the WSe_2 film are taken before and after the sputtering deposition, as shown in fig. 8.1 (d). The ML WSe_2 peaks are present post sputtering, however with a reduced relative peak magnitude, indicating some physical damage to WSe_2. However, this is not of great concern, as the function of the ML WSe_2 underlayer is not to facilitate lateral current transport, but rather to absorb spins flowing in the vertical direction (from Ta to ML WSe_2). In addition, we independently characterize the channel resistance of exfoliated ML WSe_2 films. fig. 8.1 (e) shows transfer characteristics at a drain bias of

$V_{ds} = 1$ V. It is obvious that the total channel resistance of the ML WSe_2 is greater than 1.5 $G\Omega$ without applied gate voltage, which is orders of magnitude larger than that of Ta. Hence, we conclude that in our hybrid spin Hall stack the current flows in the Ta layer. Hall bar devices are then fabricated for stacks A, B and C by e-beam lithography followed by dry etching using Ar plasma. fig. 8.1 (f) shows the optical microscope image of one representative device.

8.2.2 Extracting the value of spin Hall efficiency

The deposited stacks show perpendicular magnetic anisotropy (PMA) as revealed by anomalous Hall effect (AHE) measurements. fig. 8.2 (a) shows the measurement configuration. fig. 8.2 (b) shows the obtained hysteresis loops of the AHE resistance (R_ω) as a function of Z-directed external magnetic field. From these curves, the value of remanent resistance (R_A) for all three stacks are obtained. The R_A value for device B is larger than that of A because a larger fraction of the read current (I_{read}) flows through the CoFeB FM layer, owing to the thinner Ta layer. The saturation value of R_ω for device C (at much larger B field, not shown here) is very close to that of device B, consistent with the fact that the additional WSe_2 layer results in negligible current shunting. However, its R_A value is smaller, possibly because of the FM film breaking into multiple magnetic domains at zero field. This PMA quality can be improved by engineering the deposition conditions as have been shown in literature for other 2-D material underlayers [138–140]. However, in this work, the overall lower quality of PMA in case of stack C compared to the other two stacks is captured by the smaller R_A and a lower H_K (shown later), which are then used to calculate the spin Hall efficiencies in the later sections. This ensures that the calculated spin Hall efficiency is not artificially larger due to a weaker magnetic layer.

Next, the effective perpendicular anisotropy field (H_K) is obtained by measuring R_ω as the external field is held at a constant magnitude (shown as legends in fig. 8.2 (c)) and rotated in the Y-Z plane. The obtained curves are fitted according to the

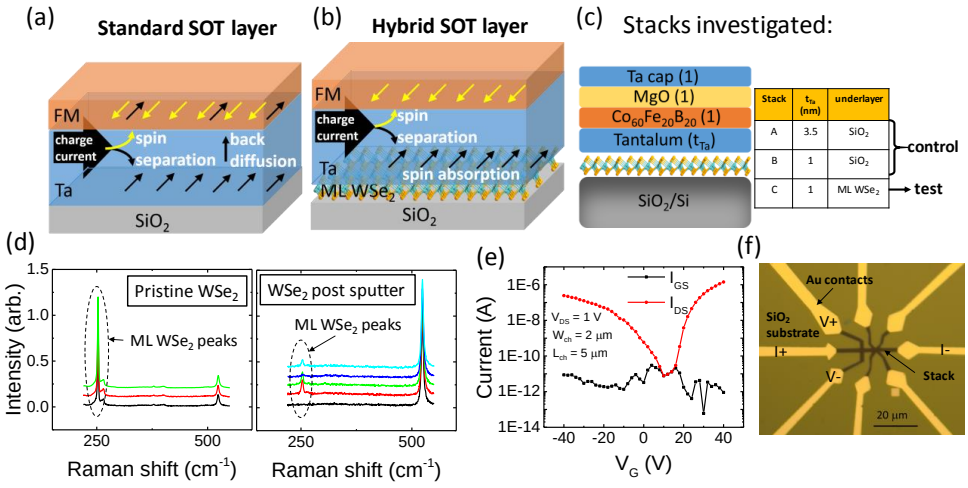

Fig. 8.1. **Effect of underlayer on charge to spin conversion:** (a) Spins accumulated at the Ta/SiO_2 interface result in a vertical concentration gradient of "black" spins, which leads to back diffusion. If the thickness of the Ta layer is comparable to the spin diffusion length, the back diffused spins can be significant and nullify the effect of spin accumulated at the FM interface. (b) By inserting a WSe_2 underlayer, the spins accumulated at the Ta/WSe_2 interface are absorbed by the WSe_2 layer, thus preventing the formation of the vertical spin concentration gradient. Hence, "yellow" spins accumulated on the FM are not nullified, resulting in a better charge to spin conversion efficiency. (c) The stacks investigated in this work. (d) Raman spectra of ML WSe_2 before and after magnetic sputter deposition. The peaks corresponding to ML WSe_2 are still preserved after the sputtering process with a reduced relative magnitude, indicative of partial damage to the ML WSe_2 layer. (e) Transfer characteristics of ML WSe_2. The width of the channel is 2 μm. The channel resistance is much larger than Ta resistance. (f) Optical microscope image of a fabricated device with the current and voltage leads marked. The width of the current electrode in this device is also 2 μm.

method shown in ref. [141] to extract H_K values. This method is robust against multi-domain issues as the large external magnetic field ensures coherent rotation of magnetization as a macrospin [141]. The obtained curves along with the fits are shown in fig. 8.2 (c). The obtained H_K values are shown in the figure insets.

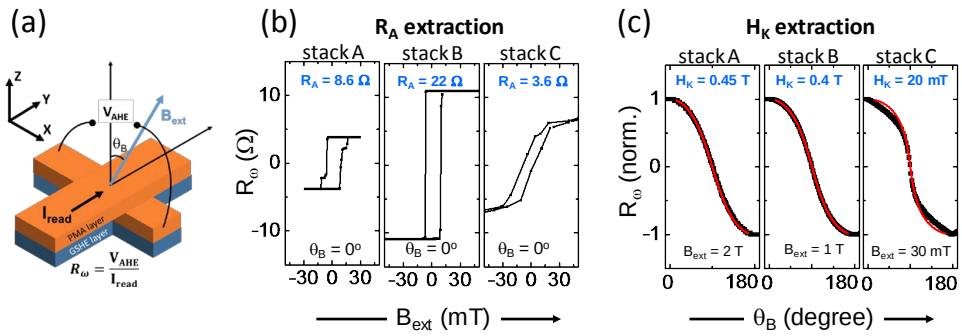

Fig. 8.2. (a) Measurement schematic to obtain R_A and H_K. For R_A extraction, the external field (B_{ext}) direction is fixed along the Z-axis ($\theta_B = 0^o$) and its magnitude is swept. For H_K extraction, the magnitude of B_{ext} is fixed, while its direction is rotated in the Z-Y plane. R_ω is obtained by dividing the first harmonic in phase component of the anomalous Hall voltage by the R.M.S of the AC current excitation. (b) Measured curves from stacks A, B and C for R_A extraction. Obtained R_A from the remanent values of R_ω at $B_{ext} = 0$ are mentioned in blue text. (c) Curves obtained from the rotation experiment. The fits to the measured curves give the value of H_K (which are mentioned in blue text in each figure inset).

SOT produces anti-damping and field like torques [142] on the magnetization that can be characterized as effective fields in the longitudinal (h_L) and transverse (h_T) direction, respectively [61, 141]. We obtain the values of h_L and h_T from the second harmonic component of the AHE resistance ($R_{2\omega}$). The measurement configuration is shown in fig. 8.3 (a). Here, the external field is applied in the plane of the film stack, with a direction that is either parallel or perpendicular to the applied current direction for extracting h_L and h_T, respectively. In this measurement configuration, $R_{2\omega}$ is given by:

$$\begin{aligned} R_{2\omega} &= -\frac{1}{2}\frac{R_A h_L}{(|B_Y| - H_K)} \\ R_{2\omega} &= -\frac{1}{2}\frac{R_A h_T}{(|B_X| - H_K)} \end{aligned} \tag{8.1}$$

where the first and the second expressions correspond to cases when B_{ext} is parallel and perpendicular to the applied current direction, respectively. In these expressions, the previously obtained values of R_A and H_K are applied leaving h_L or h_T as the

only variable in the equation, which can then be obtained by fitting the obtained $R_{2\omega}$ curve, as shown in fig. 8.3 (b)-(d). This method is also robust against multi-domain issues as the h_L, h_T are obtained by fitting to the large field regions of the $R_{2\omega}$ curve, where the magnetization is forced to behave as macrospin by the external field. The extracted h_L and h_T values are shown in the respective figure insets and table in fig. 8.3 (e).

The h_L and h_T values, normalized by the applied current density (J_{ac}) through the Ta layer are indicative of the spin Hall efficiency [143]. For the devices used in our experiments, the width of the current lead is 2 μm. Together with the film thicknesses and resistivities of Ta and CoFeB, J_{ac} is readily calculated. For simplicity, we have assumed that the resistivities of the Ta and the CoFeB layer are the same (which is true for our films grown on Si/SiO_2). If a higher resistivity for the Tantalum layer compared to the CoFeB layer is considered, then larger spin Hall efficiency values will be extracted (as the J_{ac} through the SOT layer will be smaller, hence h_L/J_{ac} will be larger). Hence, our extracted values for the spin Hall efficiencies are conservative estimates. The obtained h_L/J_{ac} values for the three stacks are shown in fig. 8.4 (a). For stack A, the control sample with 3.5 nm Ta without the underlayer, our extracted h_L/J_{ac} value is consistent with previously reported in literature [28]. For stack B, the control sample with 1nm Ta without the underlayer, the h_L/J_{ac} value reduces as $t_{Ta} = 1$ nm is smaller than the spin diffusion length in Ta, as will be explained in the next section. The h_L/J_{ac} value for stack C, our test sample with 1 nm Ta and the ML WSe_2 underlayer, has improved significantly (by 26.5×), owing to the suppression of the spin back diffusion since a large fraction of these unwanted spins are absorbed at the Ta/WSe_2 interface. Also shown in the same plot are the ratio of the longitudinal effective field to the transverse effective field (h_T/h_L). As can be seen, this ratio does not change significantly among the three stacks, which suggests the same SOT mechanism occurring in all three stacks.

The spin sink effectiveness can be directly obtained through spin pumping experiments by measuring the Gilbert damping constant of the CoFeB/Ta stack as a

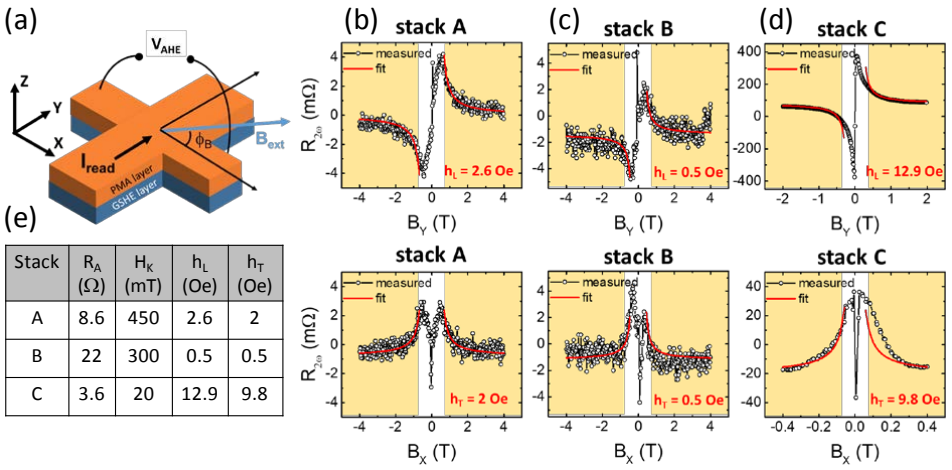

(e)

Stack	R_A (Ω)	H_K (mT)	h_L (Oe)	h_T (Oe)
A	8.6	450	2.6	2
B	22	300	0.5	0.5
C	3.6	20	12.9	9.8

Fig. 8.3. (a) Measurement schematic to obtain the SOT effective fields. The magnitude of the external magnetic field (B_{ext}) is swept while its direction is fixed in the X-Y plane of the film stack, either parallel ($\phi_B = 90^o$) or perpendicular ($\phi_B = 0^o$) to the current direction. $R_{2\omega}$ is obtained by dividing the second harmonic quadrature component of the anomalous Hall voltage by the R.M.S of the AC current excitation. Obtained second harmonic response of the devices made from (b) stack A, (c) stack B and (d) stack C. The top panel shows measurement results for the $\phi_B = 90^o$ configuration and the bottom panel shows that for the $\phi_B = 0^o$ configuration. The longitudinal (h_L) and transverse (h_T) effective fields are obtained by fitting the high field regions (highlighted in yellow) of the measured curve (black symbols) with the expression given in eq.1 (plotted in red line). The required values of R_A and H_K are obtained previously as shown in fig. 8.2. Note here that for the longitudinal configuration, the $R_{2\omega}$ curve is anti-symmetric while for the transverse configuration it is symmetric, as expected from the sign change of SOT effective fields with the change in magnetization direction. All extracted parameters are listed in the table shown in (e).

function of the Ta layer thickness, with and without the WSe_2 underlayer as done for other material systems [132]. However, the goal in our paper is to focus on the application of this effect to improve the power efficiency of an SOT based device. Therefore, we have measured and quantified the spin Hall efficiency directly and then corroborated it with the spin sink effect.

8.2.3 Corroboration with spin back diffusion

The spin Hall angle (θ_{SHE}) is the most commonly used metric to evaluate spin Hall efficiency. θ_{SHE} can be calculated from the (hL/Jac) values through the following expression [141]:

$$\theta_{SHE} = \frac{2e}{\hbar}\frac{h_L}{J_{ac}} M_S t_{FM} \tag{8.2}$$

where e is the charge of an electron, $\hbar$ is the reduced Planck constant ($h/2\pi$). t_{FM} is the thickness of the FM layer and M_S is its saturation magnetization. In our stacks, $t_{FM} = t_{CoFeB} = 1$ nm. M_S is measured using Superconducting Quantum Interference Device (SQUID) magnetometry with MPMS-3 to be 1031 emu/cc, which is consistent with the quoted value in literature for $Co_{60}Fe_{20}B_{20}$ [144].

The giant spin Hall effect results in the separation of oppositely polarized spins to the top and bottom surface of Ta. The spins reaching the top surface are absorbed by the FM layer and contribute to the observed SOT. However, the spins reaching the bottom surface of Ta get accumulated and as a result create a concentration gradient in the vertical direction. This leads to back diffusion of the oppositely directed spins into the FM, hence partly nullifying the effect of SOT. This is captured by the following expression for the measured θ_{SHE} [63]:

$$\theta_{SHE} = \theta_{SHE}^{bulk} \times \left(1 - sech\left(\frac{t_{Ta}}{\lambda_S}\right)\right) \tag{8.3}$$

Where θ_{SHE}^{bulk} is the spin Hall angle in the bulk limit and λ_S is the spin diffusion length in Ta. θ_{SHE} obtained from the above expression is plotted as a function of t_{Ta} for various λ_S in fig. 8.4 (b). From the θ_{SHE} values for stacks A and B, we extract $\lambda_S = 4.5$ nm and $\theta_{SHE}^{bulk} = 28.7$

Now, for stack C, the spins reaching the bottom surface of Ta are absorbed by the WSe_2 underlayer, resulting in suppressed back diffusion. Hence, the experimentally extracted value of θ_{SHE} for stack C should be much closer to the θ_{SHE}^{bulk} value, which is indeed confirmed in our experiment, as seen from the experimentally obtained data point (red star) for stack C in fig. 8.4 (b). This indicates that the use of WSe_2 underlayer restores the value of spin Hall angle closer to the bulk value even for the

case of ultra-thin Ta layers. The improvement in spin Hall angle is quantified by θ_{SHE}(stack C)/ θ_{SHE}(stack B) = 26.5.

8.2.4 Implication for low power SOT switching

Spin Hall angle, resistivity and the thickness of the SOT layer all are important parameters that impact the power efficiency of an SOT based memory device. Therefore, it is incomplete to consider the improvement in one of these parameters in isolation. We considered a figure of merit that captures their convoluted impact on the SOT switching power in the following way: The power required for SOT switching of a PMA magnet with an energy barrier (E_B) can be obtained from the expression for the critical switching current (I_C) [28]:

$$P_{switching} = I_C^2 R = \left(\frac{2e}{\hbar}\right)^2 \left(\frac{E_B^2}{WL}\right) / \left(\frac{\theta_{SHE}^2}{\rho \times t_{SHE}}\right) \tag{8.4}$$

Since E_B and dimensions of the magnet (W, L) are pre-determined by the desired retention time and targeted technology node respectively, the denominator, $\left(\frac{\theta_{SHE}^2}{\rho \times t_{SHE}}\right)$ becomes an important figure of merit. fig. 8.4 (c) summarizes θ_{SHE} and this figure of merit for several industrially relevant HMs. The presented Ta/WSe_2 stack outperforms the conventional giant spin Hall material β-W by a factor >1.75 and β-Ta by a factor >9.5. Our experiments suggest that efficient absorption of spins at the Ta/WSe_2 interface is responsible for this giant enhancement by preventing spin back diffusion.

8.3 Conclusion

We have demonstrated a hybrid SOT stack that shows enhanced spin Hall efficiency compared to heavy metals such as Pt, β-Ta and β-W, which are the standard materials of choice. This finding shows a promising integration of 2D materials in spintronics devices for energy efficient SOT-MRAM applications.

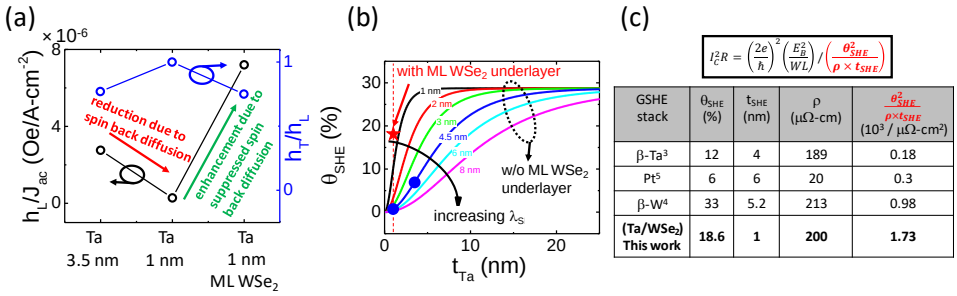

$I_c^2 R = \left(\frac{2e}{\hbar}\right)^2 \left(\frac{E_B^2}{WL}\right) / \left(\frac{\theta_{SHE}^2}{\rho \times t_{SHE}}\right)$

GSHE stack	θ_{SHE} (%)	t_{SHE} (nm)	ρ (μΩ-cm)	$\frac{\theta_{SHE}^2}{\rho \times t_{SHE}}$ (10^3 / μΩ-cm²)
β-Ta[3]	12	4	189	0.18
Pt[5]	6	6	20	0.3
β-W[4]	33	5.2	213	0.98
(Ta/WSe_2) This work	**18.6**	**1**	**200**	**1.73**

Fig. 8.4. (a) Spin Hall efficiency expressed by ratio of longitudinal effective field to the current density for the devices made from the three different stacks. When Ta thickness is decreased from 3.5 nm to 1 nm, the spin Hall efficiency decreases to nearly zero due to significant back diffusion of spins from the Ta/SiO_2 interface. When a ML WSe_2 is inserted, the spin Hall efficiency is greatly improved. The ratio of the longitudinal and transverse effective field is plotted with the right y-axis of the graph. We can see that the ratio does not show such huge change, suggesting that the mechanism of SOT is not altered. (b) The effective spin Hall angle (θ_SHE) increases as a function of the Ta layer thickness according to eq. 8.3. The experimentally obtained θ_SHE for stacks A and B (shown with the filled blue symbols) are well fitted with a spin diffusion length of 4.5 nm. With the insertion of ML WSe_2, the experimentally obtained θ_SHE (shown with the red star) is closer to the intrinsic bulk limit value. (c) Comparison of obtained θ_SHE and Ta thickness of our stacks with that presented in literature. A combination of high θ_SHE and ultra-thin Ta is desirable for energy efficient SOT switching of magnetization, captured by the figure of merit shown in the last column.

8.4 Methods

8.4.1 Sample preparation and characterization

Chemical vapor deposition (CVD) grown monolayer WSe_2 flakes were transferred to a silicon substrate with 90 nm thermal SiO_2. Raman spectroscopy was performed after this step to confirm the layer number of WSe_2 flakes. PVD magnetron sputtering was then used to deposit the stacks A, B and C mentioned in the main text, followed by another Raman spectroscopy step.

8.4.2 Device fabrication

The devices were fabricated in a two-step e-beam lithography process. First, the entire stack was etched into a Hall bar shape by e-beam lithography and dry etching using Argon plasma, followed by removal of the HSQ etch mask. Then, the contact pads were formed on the Hall bar by another e-beam lithography step followed by e-beam evaporation of Ti(20 nm)/Au(100 nm) and liftoff in acetone.

For obtaining the transfer characteristics of the monolayer WSe_2 devices as shown in fig. 8.1 (e), only one e-beam lithography step was used to define the contacts on transferred flakes, followed by e-beam evaporation of Ti(20 nm)/Au(100 nm) and liftoff in acetone.

8.4.3 Measurement setup

The transfer characteristics on fig. 8.1 (e) were obtained using Agilent semiconductor parameter analyzer with a Lakeshore probe station. The harmonic Hall measurements were performed by using a sinusoidal current from a Keithley 6221 current source and an SRS 850 DSP lock-in amplifier. These measurements were carried out inside a Quantum Design PPMS Dynacool system, with the sample mounted on a rotatable stage that allowed to change the angles (ϕ and θ) of the external magnetic field w.r.t to the film normal and current direction from 0^o to 90^o.

8.4.4 Contribution of fitting errors in SOT effective field extraction

The two parameters required for the calculation of the SOT effective fields are extracted from measurements: R_A is extracted from fig. 8.2 (b) and H_K is extracted from fig. 8.2 (c). These two parameters are then used as fitting parameters by a MATLAB curve fit tool to extract SOT effective fields h_L and h_T shown in fig. 8.3. The error in these fits according to the curve fit tool is very minimal as shown in fig. 8.5.

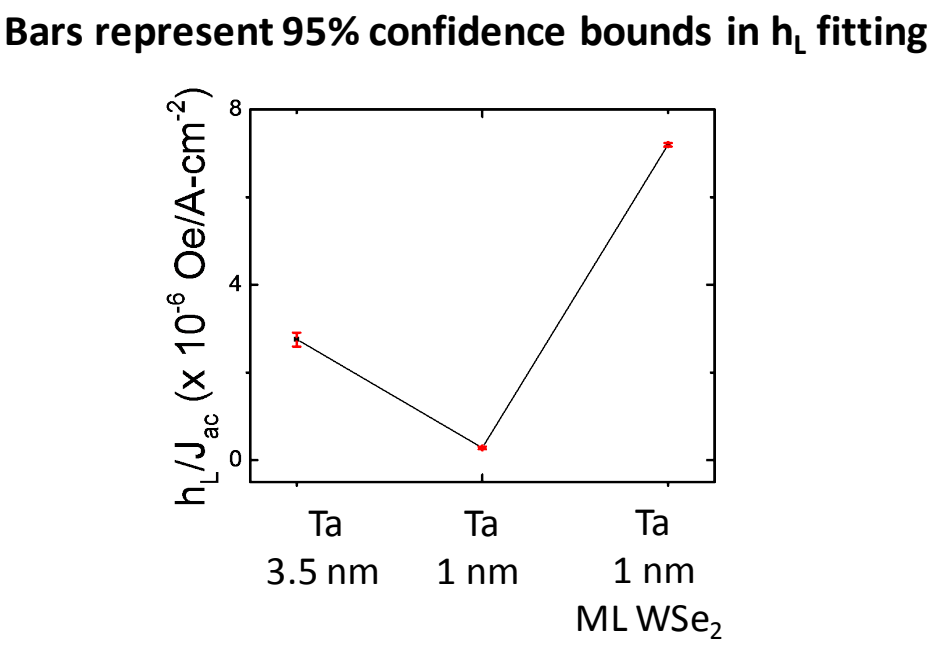

Fig. 8.5. 95% confidence bounds of the extracted h_L values from the fitting of eq. 8.1 to the measured data shown in fig. 8.3. Some error bars are smaller than the data point symbol size.

There could be an error in the extraction of H_K itself in fig. 8.2 (c), which could lead to error in the h_L values in fig. 8.4 (a). Fig 8.6 (a) shows the curves for different H_K values around the nominal value. Fig 8.6 (b) show the errors caused by using these H_K values to extract h_L.

Acknowledgements

I would like to gratefully acknowledge that this work was done in close collaboration with Dr. Terry Hung. The authors would like to thank Dr. Kerem Camsari, Prof. Joerg Appenzeller and Prof. Pramey Upadhyaya for fruitful discussions and their feedback on this work. This work was supported by the Center for Probabilistic Spin Logic for Low-Energy Boolean and Non-Boolean Computing (CAPSL), one of the Nanoelectronic Computing Research (nCORE) Centers as task 2759.003 and

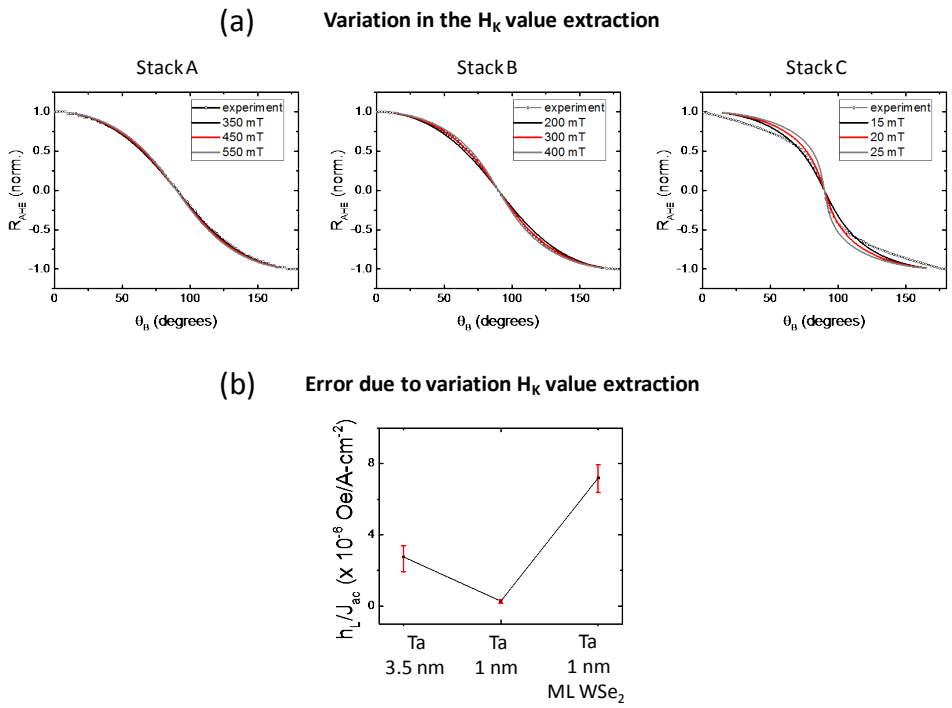

Fig. 8.6. (a) Fits to the measured R_{AHE} vs. θ_B curves for various H_K values around the nominal value. (b) Error in h_L extraction due to the above variation in the H_K values.

2759.004, a Semiconductor Research Corporation (SRC) program sponsored by the NSF through CCF 1739635.

9. SUMMARY AND OUTLOOK

Whether Moore's law is going to continue or end, the increasingly popular viewpoint is that the future of electronics may lie in the integration of CMOS technology with novel computing hardware. Hence, it is crucial to come up with innovations in computing hardware units to perform specialized tasks, while the regular computing tasks will still be implemented by the "general purpose processor" made out of Silicon CMOS transistors. This thesis is a step towards utilizing spintronics technology to design hardware building blocks for one such emerging computing paradigm: probabilistic computing with p-bits. The motivation for a major of the work performed towards this PhD has come from the theoretical developments in probabilistic computing and p-bits in Prof. Supriyo Datta group at Purdue among others. The goal of this work has been to identify the key experimental methods and the physical properties of spintronics based nano devices that can be engineered to make suitable probabilistic computing elements.

Chapter 3 explored the various schemes for implementing the LBNM in a p-bit using both in plane and perpendicular anisotropy systems. Each scheme provides a unique feature that can be beneficial depending on the p-bit device implementation. The LBNMs having in-plane anisotropy have a large pinning current, I_{pin} owing to the large demagnetization field that needs to be overcome by the torque produced by spin current [45]. Hence, the read disturb issue discussed in chapter 1 that depends on the parameter I_{read}/I_{pin} is suppressed for this type of LBNMs compared to the ones having perpendicular anisotropy. Also, it was shown in Chapter 3 that the pinning field (B_{pin}) increases by reducing the net moment ($M_S V$) compared to reducing H_K. This suggests that the earlier approach is potentially better to suppress the effect of unwanted dipolar stray field from the MTJ fixed layer as discussed in chapter 1. Interestingly, it has been shown that p-bits can operate even in the presence of both

the unwanted read disturb and the stray field issue by carefully engineering them to nullify each other [145]. For this approach, the LBNMs with weak perpendicular anisotropy become a good choice, owing to their easier current control as shown in Chapter 3 and 5.

It was discussed in Chapter 1 that for p-bit design A, tuning the magnetization state of perpendicular anisotropy nanomagnet using in plane polarized spin currents produced by the GSHE underlayer is non trivial. We have shown in Chapter 3 and 5 that a tilted anisotropy can enable this tunability. Precise control of the tilt angle, by using approaches similar to that followed by You et al. [93] is important to achieve device to device uniformity in the tunability.

The fluctuations in the circular in-plane magnets presented in chapter 3 originate from the torque produced due to a fluctuating demagnetization field. Theoretical predictions [46] have shown that these fluctuations can have sub-nanosecond time scale, which is much faster than the fluctuations from the perpendicular nanomagnet case coming purely from E_B scaling. Sutton et al. have shown that this sub-nanosecond fluctuation can lead to a significant advantage of autonomous probabilistic computers over traditional computers [146]. Future experiments to measure the time domain behavior of circular nanomagnets would be important from both a fundamental point and in this regard.

The fluctuation rate of p-bits was shown to be controllable by introducing an electrical feedback of the device output to its input using a simple resistor in chapter 3 and 6. Advantages arising from this feature, such as reducing the impact of device to device variation in fluctuation rate by designing appropriate feedback strengths could be explored in system level simulation studies [147].

In chapter 5, an autonomous network of 2 p-bits was experimentally demonstrated. The correlation in the temporal fluctuations of the two devices was described completely by the parallel PSL compact model [146] using parameters derived from the experiment. The same compact model predicts that the correlation strength in such networks not only depends on the weight of the connection, but also on the intrinsic

fluctuation rates of the p-bits. Experiments to study impact of fluctuation time scale on the obtained correlation will be important to benchmark the model and to provide guidelines for design of the weight matrix in an autonomous p-bit network.

p-bits could also be viewed as thermal energy powered self sustaining oscillators, with properties of resonance and synchronization, similar to that of typical periodic oscillators. In chapter 6, we have demonstrated phase synchronization of GSHE current controlled p-bits to periodic drives of particular frequencies. It was further shown that this synchronization frequency can be tuned by controlling an electrical feedback parameter. These phenomena can be leveraged to implement the idea of dynamic connectivity in an oscillatory associative memory arrays, as presented in ref. [18]. Demonstration of LBNM based stochastic oscillators as energy efficient hardware building blocks for associative memory arrays would be important to open another application domain for p-bits.

The work presented in this thesis mainly concerns with the experimental design of p-bits and has not discussed the implementation of the connection weights in much detail. Implementation of the connection weights using scalable technology is essential for large scale networks of p-bits. Emerging nanodevices such as memristors [148] or even magnetic memory [149] can be important in this regard.

The experimental design and study performed during the course of this PhD benefits greatly from the plethora of physical phenomena in the field of spintronics and nanomagnetism. It is worth noting that the p-bit can be implemented using all CMOS hardware as demonstrated in ref [150, 151]. The main advantage in implementing p-bits using spintronic technology is the compactness of the hardware enabled by the natural stochasticity in low barrier nanomagnets, which greatly reduces the area and power costs compared to the CMOS counterparts [32]. Furthermore, it has been argued in ref [146] that the clockless, autonomous operation of large networks of p-bits can achieve petaflips per second, which several orders of magnitude faster that other digital implementations. Along with the promising advantages, there are several challenges that need to be overcome for the realization of large scale probabilistic

computing cores as discussed in prior sections. The work presented in this thesis provides experimental methods to engineer the properties of spintronic devices to provide solutions to some of these challenges. It is the hope of the author that this work serves as an initial step in the search for the ideal probabilistic computing element and the eventual demonstration of specialized computing cores based on the probabilistic computing paradigm.

REFERENCES

REFERENCES

[1] J. Von Neumann, *The computer and the brain*. Yale University Press, 2012.

[2] G. E. Moore *et al.*, "Cramming more components onto integrated circuits," 1965.

[3] Y. LeCun, Y. Bengio, and G. Hinton, "Deep learning. nature 521," 2015.

[4] M. I. Jordan and T. M. Mitchell, "Machine learning: Trends, perspectives, and prospects," *Science*, vol. 349, no. 6245, pp. 255–260, 2015.

[5] B. Shahriari, K. Swersky, Z. Wang, R. P. Adams, and N. De Freitas, "Taking the human out of the loop: A review of bayesian optimization," *Proceedings of the IEEE*, vol. 104, no. 1, pp. 148–175, 2015.

[6] D. Heckerman, A. Mamdani, and M. P. Wellman, "Real-world applications of bayesian networks," *Communications of the ACM*, vol. 38, no. 3, pp. 24–26, 1995.

[7] S. Kirkpatrick, C. D. Gelatt, and M. P. Vecchi, "Optimization by simulated annealing," *science*, vol. 220, no. 4598, pp. 671–680, 1983.

[8] G. Indiveri and S.-C. Liu, "Memory and information processing in neuromorphic systems," *Proceedings of the IEEE*, vol. 103, no. 8, pp. 1379–1397, 2015.

[9] P. A. Merolla, J. V. Arthur, R. Alvarez-Icaza, A. S. Cassidy, J. Sawada, F. Akopyan, B. L. Jackson, N. Imam, C. Guo, Y. Nakamura *et al.*, "A million spiking-neuron integrated circuit with a scalable communication network and interface," *Science*, vol. 345, no. 6197, pp. 668–673, 2014.

[10] N. P. Jouppi, C. Young, N. Patil, D. Patterson, G. Agrawal, R. Bajwa, S. Bates, S. Bhatia, N. Boden, A. Borchers *et al.*, "In-datacenter performance analysis of a tensor processing unit," in *Proceedings of the 44th Annual International Symposium on Computer Architecture*, 2017, pp. 1–12.

[11] M. Davies, N. Srinivasa, T.-H. Lin, G. Chinya, Y. Cao, S. H. Choday, G. Dimou, P. Joshi, N. Imam, S. Jain *et al.*, "Loihi: A neuromorphic manycore processor with on-chip learning," *IEEE Micro*, vol. 38, no. 1, pp. 82–99, 2018.

[12] M. Yamaoka, C. Yoshimura, M. Hayashi, T. Okuyama, H. Aoki, and H. Mizuno, "A 20k-spin ising chip to solve combinatorial optimization problems with cmos annealing," *IEEE Journal of Solid-State Circuits*, vol. 51, no. 1, pp. 303–309, 2016.

[13] R. P. Feynman, "Simulating physics with computers," *International journal of theoretical physics*, vol. 21, no. 6, pp. 467–488, 1982.

[14] T. D. Ladd, F. Jelezko, R. Laflamme, Y. Nakamura, C. Monroe, and J. L. O'Brien, "Quantum computers," *Nature*, vol. 464, no. 7285, pp. 45–53, 2010.

[15] M. W. Johnson, M. H. Amin, S. Gildert, T. Lanting, F. Hamze, N. Dickson, R. Harris, A. J. Berkley, J. Johansson, P. Bunyk *et al.*, "Quantum annealing with manufactured spins," *Nature*, vol. 473, no. 7346, pp. 194–198, 2011.

[16] T. Inagaki, Y. Haribara, K. Igarashi, T. Sonobe, S. Tamate, T. Honjo, A. Marandi, P. L. McMahon, T. Umeki, K. Enbutsu *et al.*, "A coherent ising machine for 2000-node optimization problems," *Science*, vol. 354, no. 6312, pp. 603–606, 2016.

[17] P. L. McMahon, A. Marandi, Y. Haribara, R. Hamerly, C. Langrock, S. Tamate, T. Inagaki, H. Takesue, S. Utsunomiya, K. Aihara *et al.*, "A fully programmable 100-spin coherent ising machine with all-to-all connections," *Science*, vol. 354, no. 6312, pp. 614–617, 2016.

[18] F. C. Hoppensteadt and E. M. Izhikevich, "Oscillatory neurocomputers with dynamic connectivity," *Physical Review Letters*, vol. 82, no. 14, p. 2983, 1999.

[19] D. E. Nikonov, G. Csaba, W. Porod, T. Shibata, D. Voils, D. Hammerstrom, I. A. Young, and G. I. Bourianoff, "Coupled-oscillator associative memory array operation for pattern recognition," *IEEE Journal on Exploratory Solid-State Computational Devices and Circuits*, vol. 1, pp. 85–93, 2015.

[20] G. Csaba and W. Porod, "Perspectives of using oscillators for computing and signal processing," *arXiv preprint arXiv:1805.09056*, 2018.

[21] T. Miyazaki and N. Tezuka, "Giant magnetic tunneling effect in fe/al2o3/fe junction," *Journal of Magnetism and Magnetic Materials*, vol. 139, no. 3, pp. L231–L234, 1995.

[22] J. S. Moodera, L. R. Kinder, T. M. Wong, and R. Meservey, "Large magnetoresistance at room temperature in ferromagnetic thin film tunnel junctions," *Physical review letters*, vol. 74, no. 16, p. 3273, 1995.

[23] J. C. Slonczewski *et al.*, "Current-driven excitation of magnetic multilayers," *Journal of Magnetism and Magnetic Materials*, vol. 159, no. 1, p. L1, 1996.

[24] L. Berger, "Emission of spin waves by a magnetic multilayer traversed by a current," *Physical Review B*, vol. 54, no. 13, p. 9353, 1996.

[25] J. Katine, F. Albert, R. Buhrman, E. Myers, and D. Ralph, "Current-driven magnetization reversal and spin-wave excitations in co/cu/co pillars," *Physical review letters*, vol. 84, no. 14, p. 3149, 2000.

[26] M. Gajek, J. Nowak, J. Sun, P. Trouilloud, E. O'sullivan, D. Abraham, M. Gaidis, G. Hu, S. Brown, Y. Zhu *et al.*, "Spin torque switching of 20 nm magnetic tunnel junctions with perpendicular anisotropy," *Applied Physics Letters*, vol. 100, no. 13, p. 132408, 2012.

[27] S. Ikeda, K. Miura, H. Yamamoto, K. Mizunuma, H. Gan, M. Endo, S. Kanai, J. Hayakawa, F. Matsukura, and H. Ohno, "A perpendicular-anisotropy cofeb–mgo magnetic tunnel junction," *Nature materials*, vol. 9, no. 9, p. 721, 2010.

[28] L. Liu, C.-F. Pai, Y. Li, H. Tseng, D. Ralph, and R. Buhrman, "Spin-torque switching with the giant spin hall effect of tantalum," *Science*, vol. 336, no. 6081, pp. 555–558, 2012.

[29] K. Y. Camsari, P. Debashis, V. Ostwal, A. Z. Pervaiz, T. Shen, Z. Chen, S. Datta, and J. Appenzeller, "From charge to spin and spin to charge: Stochastic magnets for probabilistic switching," *Proceedings of the IEEE*, pp. 1–16, 2020.

[30] K. Y. Camsari, R. Faria, B. M. Sutton, and S. Datta, "Stochastic p-bits for invertible logic," *Physical Review X*, vol. 7, no. 3, p. 031014, 2017.

[31] D. H. Ackley, G. E. Hinton, and T. J. Sejnowski, "A learning algorithm for boltzmann machines," *Cognitive science*, vol. 9, no. 1, pp. 147–169, 1985.

[32] R. Zand, K. Y. Camsari, S. D. Pyle, I. Ahmed, C. H. Kim, and R. F. DeMara, "Low-energy deep belief networks using intrinsic sigmoidal spintronic-based probabilistic neurons," in *Proceedings of the 2018 on Great Lakes Symposium on VLSI*, 2018, pp. 15–20.

[33] J. Kaiser, R. Faria, K. Y. Camsari, and S. Datta, "Probabilistic circuits for autonomous learning: A simulation study," *arXiv preprint arXiv:1910.06288*, 2019.

[34] B. Behin-Aein, V. Diep, and S. Datta, "A building block for hardware belief networks," *Scientific reports*, vol. 6, p. 29893, 2016.

[35] R. Faria, K. Y. Camsari, and S. Datta, "Implementing bayesian networks with embedded stochastic mram," *AIP Advances*, vol. 8, no. 4, p. 045101, 2018.

[36] S. S. Haykin *et al.*, "Neural networks and learning machines/simon haykin." 2009.

[37] S. Geman and D. Geman, "Stochastic relaxation, gibbs distributions, and the bayesian restoration of images," *IEEE Transactions on pattern analysis and machine intelligence*, no. 6, pp. 721–741, 1984.

[38] B. Sutton, K. Y. Camsari, B. Behin-Aein, and S. Datta, "Intrinsic optimization using stochastic nanomagnets," *Scientific Reports*, vol. 7, p. 44370, 2017.

[39] K. Y. Camsari, S. Chowdhury, and S. Datta, "Scalable emulation of sign-problem–free hamiltonians with room-temperature p-bits," *Physical Review Applied*, vol. 12, no. 3, p. 034061, 2019.

[40] T. Kadowaki and H. Nishimori, "Quantum annealing in the transverse ising model," *Physical Review E*, vol. 58, no. 5, p. 5355, 1998.

[41] T. Okuyama, M. Hayashi, and M. Yamaoka, "An ising computer based on simulated quantum annealing by path integral monte carlo method," in *2017 IEEE International Conference on Rebooting Computing (ICRC)*. IEEE, 2017, pp. 1–6.

[42] T. Albash and D. A. Lidar, "Adiabatic quantum computation," *Reviews of Modern Physics*, vol. 90, no. 1, p. 015002, 2018.

[43] M. Troyer and U.-J. Wiese, "Computational complexity and fundamental limitations to fermionic quantum monte carlo simulations," *Physical review letters*, vol. 94, no. 17, p. 170201, 2005.

[44] L. Lopez-Diaz, L. Torres, and E. Moro, "Transition from ferromagnetism to superparamagnetism on the nanosecond time scale," *Physical Review B*, vol. 65, no. 22, p. 224406, 2002.

[45] O. Hassan, R. Faria, K. Y. Camsari, J. Z. Sun, and S. Datta, "Low-barrier magnet design for efficient hardware binary stochastic neurons," *IEEE Magnetics Letters*, vol. 10, pp. 1–5, 2019.

[46] J. Kaiser, A. Rustagi, K. Camsari, J. Sun, S. Datta, and P. Upadhyaya, "Subnanosecond fluctuations in low-barrier nanomagnets," *Physical Review Applied*, vol. 12, no. 5, p. 054056, 2019.

[47] K. Y. Camsari, S. Salahuddin, and S. Datta, "Implementing p-bits with embedded mtj," *IEEE Electron Device Letters*, vol. 38, no. 12, pp. 1767–1770, 2017.

[48] S. Datta, S. Salahuddin, and B. Behin-Aein, "Non-volatile spin switch for boolean and non-boolean logic," *Applied Physics Letters*, vol. 101, no. 25, p. 252411, 2012.

[49] A. Lucas, "Ising formulations of many np problems," *Frontiers in Physics*, vol. 2, p. 5, 2014.

[50] J. P. Morgan, A. Stein, S. Langridge, and C. H. Marrows, "Thermal ground-state ordering and elementary excitations in artificial magnetic square ice," *Nature Physics*, vol. 7, no. 1, p. 75, 2011.

[51] R. Faria, K. Y. Camsari, and S. Datta, "Low-barrier nanomagnets as p-bits for spin logic," *IEEE Magnetics Letters*, vol. 8, pp. 1–5, 2017.

[52] R. Zand, K. Y. Camsari, I. Ahmed, S. D. Pyle, C. H. Kim, S. Datta, and R. F. DeMara, "R-dbn: A resistive deep belief network architecture leveraging the intrinsic behavior of probabilistic devices," *arXiv preprint arXiv:1710.00249*, 2017.

[53] N. Locatelli, A. Mizrahi, A. Accioly, R. Matsumoto, A. Fukushima, H. Kubota, S. Yuasa, V. Cros, L. G. Pereira, D. Querlioz *et al.*, "Noise-enhanced synchronization of stochastic magnetic oscillators," *Physical Review Applied*, vol. 2, no. 3, p. 034009, 2014.

[54] D. Vodenicarevic, N. Locatelli, A. Mizrahi, J. S. Friedman, A. F. Vincent, M. Romera, A. Fukushima, K. Yakushiji, H. Kubota, S. Yuasa *et al.*, "Low-energy truly random number generation with superparamagnetic tunnel junctions for unconventional computing," *Physical Review Applied*, vol. 8, no. 5, p. 054045, 2017.

[55] O. Hassan, K. Y. Camsari, and S. Datta, "Voltage-driven building block for hardware belief networks," *arXiv preprint arXiv:1801.09026*, 2018.

[56] S. Manipatruni, D. E. Nikonov, C.-C. Lin, P. Bhagwati, Y. L. Huang, A. R. Damodaran, Z. Chen, R. Ramesh, and I. A. Young, "Voltage control of uni-directional anisotropy in ferromagnet-multiferroic system," *arXiv preprint arXiv:1801.08280*, 2018.

[57] P. Debashis, R. Faria, K. Y. Camsari, J. Appenzeller, S. Datta, and Z. Chen, "Experimental demonstration of nanomagnet networks as hardware for ising computing," in *Electron Devices Meeting (IEDM), 2016 IEEE International*. IEEE, 2016, pp. 34–3.

[58] R. Cowburn, D. Koltsov, A. Adeyeye, M. Welland, and D. Tricker, "Single-domain circular nanomagnets," *Physical Review Letters*, vol. 83, no. 5, p. 1042, 1999.

[59] W. F. Brown Jr, "The fundamental theorem of fine-ferromagnetic-particle theory," *Journal of Applied Physics*, vol. 39, no. 2, pp. 993–994, 1968.

[60] R. Cowburn, "Property variation with shape in magnetic nanoelements," *Journal of Physics D: Applied Physics*, vol. 33, no. 1, p. R1, 2000.

[61] M. Hayashi, J. Kim, M. Yamanouchi, and H. Ohno, "Quantitative characterization of the spin-orbit torque using harmonic hall voltage measurements," *Physical Review B*, vol. 89, no. 14, p. 144425, 2014.

[62] A. Rukhin, J. Soto, J. Nechvatal, M. Smid, and E. Barker, "A statistical test suite for random and pseudorandom number generators for cryptographic applications," Booz-Allen and Hamilton Inc Mclean Va, Tech. Rep., 2001.

[63] L. Liu, O. Lee, T. Gudmundsen, D. Ralph, and R. Buhrman, "Current-induced switching of perpendicularly magnetized magnetic layers using spin torque from the spin hall effect," *Physical review letters*, vol. 109, no. 9, p. 096602, 2012.

[64] D. Bhowmik, L. You, and S. Salahuddin, "Spin hall effect clocking of nanomagnetic logic without a magnetic field," *Nature nanotechnology*, vol. 9, no. 1, p. 59, 2014.

[65] S. Fukami, T. Anekawa, C. Zhang, and H. Ohno, "A spin–orbit torque switching scheme with collinear magnetic easy axis and current configuration," *Nature nanotechnology*, vol. 11, no. 7, p. 621, 2016.

[66] W. H. Butler, T. Mewes, C. K. Mewes, P. Visscher, W. H. Rippard, S. E. Russek, and R. Heindl, "Switching distributions for perpendicular spin-torque devices within the macrospin approximation," *IEEE Transactions on Magnetics*, vol. 48, no. 12, pp. 4684–4700, 2012.

[67] A. Fukushima, T. Seki, K. Yakushiji, H. Kubota, H. Imamura, S. Yuasa, and K. Ando, "Spin dice: A scalable truly random number generator based on spintronics," *Applied Physics Express*, vol. 7, no. 8, p. 083001, 2014.

[68] J. Pearl, *Probabilistic reasoning in intelligent systems: networks of plausible inference*. Morgan Kaufmann, 2014.

[69] D. Heckerman and J. S. Breese, "Causal independence for probability assessment and inference using bayesian networks," *IEEE Transactions on Systems, Man, and Cybernetics-Part A: Systems and Humans*, vol. 26, no. 6, pp. 826–831, 1996.

[70] S. Zermani, C. Dezan, H. Chenini, J. Diguet, and R. Euler, "Fpga implementation of bayesian network inference for an embedded diagnosis," in *2015 IEEE Conference on Prognostics and Health Management (PHM)*, June 2015, pp. 1–10.

[71] R. Cai, A. Ren, N. Liu, C. Ding, L. Wang, X. Qian, M. Pedram, and Y. Wang, "Vibnn: Hardware acceleration of bayesian neural networks," *SIGPLAN Not.*, vol. 53, no. 2, p. 476–488, Mar. 2018. [Online]. Available: https://doi.org/10.1145/3296957.3173212

[72] V. K. Mansinghka, E. M. Jonas, and J. B. Tenenbaum, "Stochastic digital circuits for probabilistic inference," *Massachussets Institute of Technology, Technical Report MITCSAIL-TR*, vol. 2069, 2008.

[73] L. N. Chakrapani, P. Korkmaz, B. E. Akgul, and K. V. Palem, "Probabilistic system-on-a-chip architectures," *ACM Transactions on Design Automation of Electronic Systems (TODAES)*, vol. 12, no. 3, pp. 1–28, 2008.

[74] Z. Weijia, G. W. Ling, and Y. K. Seng, "Pcmos-based hardware implementation of bayesian network," in *Electron Devices and Solid-State Circuits, 2007. EDSSC 2007. IEEE Conference on*. IEEE, 2007, pp. 337–340.

[75] B. Behin-Aein, V. Diep, and S. Datta, "A building block for hardware belief networks," *Scientific Reports*, vol. 6, p. 29893, 2016.

[76] O. Hassan, K. Y. Camsari, and S. Datta, "Voltage-driven building block for hardware belief networks," *IEEE Design & Test*, vol. 36, no. 3, pp. 15–21, 2019.

[77] P. Debashis, P. Upadhyaya, and Z. Chen, "Electrical annealing and stochastic resonance in superparamagnets for oscillatory networks with dynamic connectivity," in *APS Meeting Abstracts*, 2019.

[78] P. Debashis, R. Faria, K. Y. Camsari, and Z. Chen, "Design of stochastic nanomagnets for probabilistic spin logic," *IEEE Magnetics Letters*, vol. 9, pp. 1–5, 2018.

[79] P. Debashis and Z. Chen, "Experimental demonstration of a spin logic device with deterministic and stochastic mode of operation," *Scientific reports*, vol. 8, no. 1, pp. 1–9, 2018.

[80] ——, "Tunable random number generation using single superparamagnet with perpendicular magnetic anisotropy," in *2018 76th Device Research Conference (DRC)*. IEEE, 2018, pp. 1–2.

[81] V. Ostwal, P. Debashis, R. Faria, Z. Chen, and J. Appenzeller, "Spin-torque devices with hard axis initialization as stochastic binary neurons," *Scientific reports*, vol. 8, no. 1, pp. 1–8, 2018.

[82] Y. Shim, S. Chen, A. Sengupta, and K. Roy, "Stochastic spin-orbit torque devices as elements for bayesian inference," *Scientific reports*, vol. 7, no. 1, pp. 1–9, 2017.

[83] I. M. Miron, K. Garello, G. Gaudin, P.-J. Zermatten, M. V. Costache, S. Auffret, S. Bandiera, B. Rodmacq, A. Schuhl, and P. Gambardella, "Perpendicular switching of a single ferromagnetic layer induced by in-plane current injection," *Nature*, vol. 476, no. 7359, p. 189, 2011.

[84] A. E. Gelfand, S. E. Hills, A. Racine-Poon, and A. F. Smith, "Illustration of bayesian inference in normal data models using gibbs sampling," *Journal of the American Statistical Association*, vol. 85, no. 412, pp. 972–985, 1990.

[85] I. Yildirim, "Bayesian inference: Gibbs sampling," *Technical Note, University of Rochester*, 2012.

[86] R. P. Feynman, "Simulating physics with computers," *Int. J. Theor. Phys*, vol. 21, no. 6/7, 1999.

[87] W. H. Choi, Y. Lv, J. Kim, A. Deshpande, G. Kang, J.-p. Wang, and C. H. Kim, "A magnetic tunnel junction based true random number generator with conditional perturb and real-time output probability tracking," in *Electron Devices Meeting (IEDM)*, 2014, pp. 12–5.

[88] Editorial, "The memristor revisited," *Nature electronics*, vol. 1, no. 1, pp. 261–261, 2018.

[89] S. Choi, S. H. Tan, Z. Li, Y. Kim, C. Choi, P.-Y. Chen, H. Yeon, S. Yu, and J. Kim, "Sige epitaxial memory for neuromorphic computing with reproducible high performance based on engineered dislocations," *Nature materials*, vol. 17, no. 4, pp. 335–340, 2018.

[90] W. Scott, J. Jeffrey, B. Heard, D. E. Nikonov, I. A. Young, S. Manipatruni, A. Naeemi, and R. M. Iraei, "Hybrid piezoelectric-magnetic neurons: a proposal for energy-efficient machine learning," in *Proceedings of the ACMSE 2018 Conference*, 2018, pp. 1–5.

[91] K. Garello, F. Yasin, S. Couet, L. Souriau, J. Swerts, S. Rao, S. Beek, W. Kim, E. Liu, S. Kundu *et al.*, "2018 ieee symposium on vlsi circuits," 2018.

[92] V. Ostwal and J. Appenzeller, "Spin–orbit torque-controlled magnetic tunnel junction with low thermal stability for tunable random number generation," *IEEE Magnetics Letters*, vol. 10, pp. 1–5, 2019.

[93] L. You, O. Lee, D. Bhowmik, D. Labanowski, J. Hong, J. Bokor, and S. Salahuddin, "Switching of perpendicularly polarized nanomagnets with spin orbit torque without an external magnetic field by engineering a tilted anisotropy," *Proceedings of the National Academy of Sciences*, vol. 112, no. 33, pp. 10 310–10 315, 2015.

[94] G. Yu, P. Upadhyaya, Y. Fan, J. G. Alzate, W. Jiang, K. L. Wong, S. Takei, S. A. Bender, L.-T. Chang, Y. Jiang *et al.*, "Switching of perpendicular magnetization by spin–orbit torques in the absence of external magnetic fields," *Nature nanotechnology*, vol. 9, no. 7, p. 548, 2014.

[95] W. Kong, Y. Ji, X. Zhang, H. Wu, Q. Zhang, Z. Yuan, C. Wan, X. Han, T. Yu, K. Fukuda *et al.*, "Field-free spin hall effect driven magnetization switching in pd/co/irmn exchange coupling system," *Applied Physics Letters*, vol. 109, no. 13, p. 132402, 2016.

[96] Y. Cao, A. Rushforth, Y. Sheng, H. Zheng, and K. Wang, "Spintronic synapses: Tuning a binary ferromagnet into a multistate synapse with spin–orbit-torque-induced plasticity (adv. funct. mater. 25/2019)," *Advanced Functional Materials*, vol. 29, no. 25, p. 1970175, 2019.

[97] Y.-W. Oh, S.-h. C. Baek, Y. Kim, H. Y. Lee, K.-D. Lee, C.-G. Yang, E.-S. Park, K.-S. Lee, K.-W. Kim, G. Go *et al.*, "Field-free switching of perpendicular magnetization through spin–orbit torque in antiferromagnet/ferromagnet/oxide structures," *Nature nanotechnology*, vol. 11, no. 10, p. 878, 2016.

[98] S. Fukami, C. Zhang, S. DuttaGupta, A. Kurenkov, and H. Ohno, "Magnetization switching by spin-orbit torque in an antiferromagnet-ferromagnet bilayer system," *Nature materials*, 2016.

[99] K. Cai, M. Yang, H. Ju, S. Wang, Y. Ji, B. Li, K. W. Edmonds, Y. Sheng, B. Zhang, N. Zhang *et al.*, "Electric field control of deterministic current-induced magnetization switching in a hybrid ferromagnetic/ferroelectric structure," *Nature materials*, vol. 16, no. 7, pp. 712–716, 2017.

[100] M. Yang, Y. Deng, Z. Wu, K. Cai, K. W. Edmonds, Y. Li, Y. Sheng, S. Wang, Y. Cui, J. Luo *et al.*, "Spin logic devices via electric field controlled magnetization reversal by spin-orbit torque," *IEEE Electron Device Letters*, vol. 40, no. 9, pp. 1554–1557, 2019.

[101] A. Timopheev, R. Sousa, M. Chshiev, H. Nguyen, and B. Dieny, "Second order anisotropy contribution in perpendicular magnetic tunnel junctions," *Scientific reports*, vol. 6, no. 1, pp. 1–12, 2016.

[102] C.-C. Nguyen and R. T. Howe, "An integrated cmos micromechanical resonator high-q oscillator," *IEEE Journal of Solid-State Circuits*, vol. 34, no. 4, pp. 440–455, 1999.

[103] I. Mahboob and H. Yamaguchi, "Bit storage and bit flip operations in an electromechanical oscillator," *Nature nanotechnology*, vol. 3, no. 5, p. 275, 2008.

[104] N. Shukla, A. Parihar, M. Cotter, M. Barth, X. Li, N. Chandramoorthy, H. Paik, D. G. Schlom, V. Narayanan, A. Raychowdhury *et al.*, "Pairwise coupled hybrid vanadium dioxide-mosfet (hvfet) oscillators for non-boolean associative computing," in *2014 IEEE International Electron Devices Meeting*. IEEE, 2014, pp. 28–7.

[105] S. Kaka, M. R. Pufall, W. H. Rippard, T. J. Silva, S. E. Russek, and J. A. Katine, "Mutual phase-locking of microwave spin torque nano-oscillators," *Nature*, vol. 437, no. 7057, pp. 389–392, 2005.

[106] A. Awad, P. Dürrenfeld, A. Houshang, M. Dvornik, E. Iacocca, R. Dumas, and J. Åkerman, "Long-range mutual synchronization of spin hall nano-oscillators," *Nature Physics*, vol. 13, no. 3, pp. 292–299, 2017.

[107] A. Neiman, A. Silchenko, V. Anishchenko, and L. Schimansky-Geier, "Stochastic resonance: Noise-enhanced phase coherence," *Physical Review E*, vol. 58, no. 6, p. 7118, 1998.

[108] J. A. Freund, L. Schimansky-Geier, and P. Hänggi, "Frequency and phase synchronization in stochastic systems," *Chaos: An Interdisciplinary Journal of Nonlinear Science*, vol. 13, no. 1, pp. 225–238, 2003.

[109] L. Gammaitoni, P. Hänggi, P. Jung, and F. Marchesoni, "Stochastic resonance," *Reviews of modern physics*, vol. 70, no. 1, p. 223, 1998.

[110] B. Shulgin, A. Neiman, and V. Anishchenko, "Mean switching frequency locking in stochastic bistable systems driven by a periodic force," *Physical review letters*, vol. 75, no. 23, p. 4157, 1995.

[111] P. Boriskov, M. Belyaev, and A. Velichko, "Stochastic synchronization and the signal-to-noise ratio in an oscillator with a film vo 2 switch," *Journal of Communications Technology and Electronics*, vol. 64, no. 7, pp. 705–711, 2019.

[112] V. K. Verma and R. Yadava, "Stochastic resonance in mems capacitive sensors," *Sensors and Actuators B: Chemical*, vol. 235, pp. 583–602, 2016.

[113] S. Hedayat, I. Sourikopoulos, C. Loyez, F. Danneville, L. Clavier, V. Hoel, and A. Cappy, "Experimental investigation of stochastic resonance in a 65nm cmos artificial neuron," in *2017 International Conference on Noise and Fluctuations (ICNF)*. IEEE, 2017, pp. 1–4.

[114] B. Behin-Aein, D. Datta, S. Salahuddin, and S. Datta, "Proposal for an all-spin logic device with built-in memory," *Nature nanotechnology*, vol. 5, no. 4, p. 266, 2010.

[115] D. A. Allwood, G. Xiong, C. Faulkner, D. Atkinson, D. Petit, and R. Cowburn, "Magnetic domain-wall logic," *Science*, vol. 309, no. 5741, pp. 1688–1692, 2005.

[116] M. G. Mankalale, Z. Liang, Z. Zhao, C. H. Kim, J.-P. Wang, and S. S. Sapatnekar, "Comet: Composite-input magnetoelectric-based logic technology," *IEEE Journal on Exploratory Solid-State Computational Devices and Circuits*, vol. 3, pp. 27–36, 2017.

[117] A. V. Penumatcha, C.-C. Lin, V. Q. Diep, S. Datta, J. Appenzeller, and Z. Chen, "Impact of scaling on the dipolar coupling in magnet–insulator–magnet structures," *IEEE Transactions on Magnetics*, vol. 52, no. 1, pp. 1–7, 2016.

[118] J. Heron, J. Bosse, Q. He, Y. Gao, M. Trassin, L. Ye, J. Clarkson, C. Wang, J. Liu, S. Salahuddin *et al.*, "Deterministic switching of ferromagnetism at room temperature using an electric field," *Nature*, vol. 516, no. 7531, p. 370, 2014.

[119] Z. Wang, Y. Zhang, Y. Wang, Y. Li, H. Luo, J. Li, and D. Viehland, "Magnetoelectric assisted 180 magnetization switching for electric field addressable writing in magnetoresistive random-access memory," *ACS nano*, vol. 8, no. 8, pp. 7793–7800, 2014.

[120] J. W. Chenchen, M. A. K. B. Akhtar, R. Sbiaa, M. Hao, L. Y. H. Sunny, W. S. Kai, L. Ping, P. Carlberg, and A. K. S. Arthur, "Size dependence effect in mgo-based cofeb tunnel junctions with perpendicular magnetic anisotropy," *Japanese Journal of Applied Physics*, vol. 51, no. 1R, p. 013101, 2011.

[121] S. Li, S. Goolaup, J. Kwon, F. Luo, W. Gan, and W. S. Lew, "Deterministic spin-orbit torque induced magnetization reversal in pt/[co/ni] n/co/ta multilayer hall bars," *Scientific Reports*, vol. 7, no. 1, p. 972, 2017.

[122] S. Salahuddin and S. Datta, "Interacting systems for self-correcting low power switching," *Applied physics letters*, vol. 90, no. 9, p. 093503, 2007.

[123] C. Pan and A. Naeemi, "An expanded benchmarking of beyond-cmos devices based on boolean and neuromorphic representative circuits," *IEEE Journal on Exploratory Solid-State Computational Devices and Circuits*, vol. 3, pp. 101–110, 2017.

[124] N. Kani and A. Naeemi, "Analytical models for coupling reliability in identical two-magnet systems during slow reversals," *Journal of Applied Physics*, vol. 122, no. 22, p. 223902, 2017.

[125] T. Zhu, P. Chen, Q. Zhang, R. Yu, and B. Liu, "Giant linear anomalous hall effect in the perpendicular cofeb thin films," *Applied Physics Letters*, vol. 104, no. 20, p. 202404, 2014.

[126] S. Bhatti, R. Sbiaa, A. Hirohata, H. Ohno, S. Fukami, and S. Piramanayagam, "Spintronics based random access memory: a review," *Materials Today*, vol. 20, no. 9, pp. 530–548, 2017.

[127] K. Wang, J. Alzate, and P. K. Amiri, "Low-power non-volatile spintronic memory: Stt-ram and beyond," *Journal of Physics D: Applied Physics*, vol. 46, no. 7, p. 074003, 2013.

[128] C.-F. Pai, L. Liu, Y. Li, H. Tseng, D. Ralph, and R. Buhrman, "Spin transfer torque devices utilizing the giant spin hall effect of tungsten," *Applied Physics Letters*, vol. 101, no. 12, p. 122404, 2012.

[129] L. Liu, T. Moriyama, D. Ralph, and R. Buhrman, "Spin-torque ferromagnetic resonance induced by the spin hall effect," *Physical review letters*, vol. 106, no. 3, p. 036601, 2011.

[130] R. Yu, B. Miao, L. Sun, Q. Liu, J. Du, P. Omelchenko, B. Heinrich, M. Wu, and H. Ding, "Determination of spin hall angle and spin diffusion length in β-phase-dominated tantalum," *Physical Review Materials*, vol. 2, no. 7, p. 074406, 2018.

[131] H. Jiao and G. E. Bauer, "Spin backflow and ac voltage generation by spin pumping and the inverse spin hall effect," *Physical review letters*, vol. 110, no. 21, p. 217602, 2013.

[132] Y. Tserkovnyak, A. Brataas, G. E. Bauer, and B. I. Halperin, "Nonlocal magnetization dynamics in ferromagnetic heterostructures," *Reviews of Modern Physics*, vol. 77, no. 4, p. 1375, 2005.

[133] W. Yan, O. Txoperena, R. Llopis, H. Dery, L. E. Hueso, and F. Casanova, "A two-dimensional spin field-effect switch," *Nature communications*, vol. 7, no. 1, pp. 1–6, 2016.

[134] A. Dankert and S. P. Dash, "Electrical gate control of spin current in van der waals heterostructures at room temperature," *Nature communications*, vol. 8, no. 1, pp. 1–6, 2017.

[135] D. Xiao, G.-B. Liu, W. Feng, X. Xu, and W. Yao, "Coupled spin and valley physics in monolayers of mos 2 and other group-vi dichalcogenides," *Physical review letters*, vol. 108, no. 19, p. 196802, 2012.

[136] Z. Zhu, Y. Cheng, and U. Schwingenschlögl, "Giant spin-orbit-induced spin splitting in two-dimensional transition-metal dichalcogenide semiconductors," *Physical Review B*, vol. 84, no. 15, p. 153402, 2011.

[137] W. Feng, Y. Yao, W. Zhu, J. Zhou, W. Yao, and D. Xiao, "Intrinsic spin hall effect in monolayers of group-vi dichalcogenides: A first-principles study," *Physical Review B*, vol. 86, no. 16, p. 165108, 2012.

[138] Q. Shao, G. Yu, Y.-W. Lan, Y. Shi, M.-Y. Li, C. Zheng, X. Zhu, L.-J. Li, P. K. Amiri, and K. L. Wang, "Strong rashba-edelstein effect-induced spin–orbit torques in monolayer transition metal dichalcogenide/ferromagnet bilayers," *Nano letters*, vol. 16, no. 12, pp. 7514–7520, 2016.

[139] H. Yang, A. D. Vu, A. Hallal, N. Rougemaille, J. Coraux, G. Chen, A. K. Schmid, and M. Chshiev, "Anatomy and giant enhancement of the perpendicular magnetic anisotropy of cobalt–graphene heterostructures," *Nano letters*, vol. 16, no. 1, pp. 145–151, 2016.

[140] W. Zhang, P. K. J. Wong, X. Zhou, A. Rath, Z. Huang, H. Wang, S. A. Morton, J. Yuan, L. Zhang, R. Chua *et al.*, "Ferromagnet/two-dimensional semiconducting transition-metal dichalcogenide interface with perpendicular magnetic anisotropy," *ACS nano*, vol. 13, no. 2, pp. 2253–2261, 2019.

[141] Y. Fan, P. Upadhyaya, X. Kou, M. Lang, S. Takei, Z. Wang, J. Tang, L. He, L.-T. Chang, M. Montazeri *et al.*, "Magnetization switching through giant spin–orbit torque in a magnetically doped topological insulator heterostructure," *Nature materials*, vol. 13, no. 7, pp. 699–704, 2014.

[142] J. Z. Sun, "Spin-current interaction with a monodomain magnetic body: A model study," *Physical Review B*, vol. 62, no. 1, p. 570, 2000.

[143] K. Garello, I. M. Miron, C. O. Avci, F. Freimuth, Y. Mokrousov, S. Blügel, S. Auffret, O. Boulle, G. Gaudin, and P. Gambardella, "Symmetry and magnitude of spin–orbit torques in ferromagnetic heterostructures," *Nature nanotechnology*, vol. 8, no. 8, p. 587, 2013.

[144] J. M. Shaw, H. T. Nembach, M. Weiler, T. Silva, M. Schoen, J. Z. Sun, and D. C. Worledge, "Perpendicular magnetic anisotropy and easy cone state in ta/co 60 fe 20 b 20/mgo," *IEEE Magnetics Letters*, vol. 6, pp. 1–4, 2015.

[145] W. A. Borders, A. Z. Pervaiz, S. Fukami, K. Y. Camsari, H. Ohno, and S. Datta, "Integer factorization using stochastic magnetic tunnel junctions," *Nature*, vol. 573, no. 7774, pp. 390–393, 2019.

[146] B. Sutton, R. Faria, L. A. Ghantasala, K. Y. Camsari, and S. Datta, "Autonomous probabilistic coprocessing with petaflips per second," *arXiv preprint arXiv:1907.09664*, 2019.

[147] P. Wood, H. Pourmeidani, and R. F. DeMara, "Modular simulation framework for process variation analysis of mram-based deep belief networks," *arXiv preprint arXiv:2002.00897*, 2020.

[148] M. Hu, J. P. Strachan, Z. Li, E. M. Grafals, N. Davila, C. Graves, S. Lam, N. Ge, J. J. Yang, and R. S. Williams, "Dot-product engine for neuromorphic computing: Programming 1t1m crossbar to accelerate matrix-vector multiplication," in *2016 53nd ACM/EDAC/IEEE Design Automation Conference (DAC)*. IEEE, 2016, pp. 1–6.

[149] A. F. Vincent, J. Larroque, N. Locatelli, N. B. Romdhane, O. Bichler, C. Gamrat, W. S. Zhao, J.-O. Klein, S. Galdin-Retailleau, and D. Querlioz, "Spin-transfer torque magnetic memory as a stochastic memristive synapse for neuromorphic systems," *IEEE transactions on biomedical circuits and systems*, vol. 9, no. 2, pp. 166–174, 2015.

[150] A. Z. Pervaiz, L. A. Ghantasala, K. Y. Camsari, and S. Datta, "Hardware emulation of stochastic p-bits for invertible logic," *Scientific reports*, vol. 7, no. 1, pp. 1–13, 2017.

[151] A. Z. Pervaiz, B. M. Sutton, L. A. Ghantasala, and K. Y. Camsari, "Weighted p-bits for fpga implementation of probabilistic circuits," *IEEE transactions on neural networks and learning systems*, vol. 30, no. 6, pp. 1920–1926, 2018.

VITA

VITA

Punyashloka Debashis received his B.Tech degree from the Indian Institute of Technology, Kanpur and M.Tech degree from Indian Institute of Technology, Bombay both in Electrical Engineering, in the years 2012 and 2014, respectively. During his M.Tech, he worked on novel 3D channel materials and device designs for future CMOS devices. He joined Purdue University in Fall 2014 for pursuing his PhD degree in the School of Electrical and Computer Engineering. His PhD work involved the design and experimental investigation of spintronics based logic devices. During his PhD work, he designed and performed experiments towards an emerging computing platform based on probabilistic (p)-bits. After the completion of his PhD, he will be joining the Components Research division at Intel Corp., Hillsboro, Oregon.